12-23-2013

Understanding CRX-Associated Retinopathies Using Animal Models

Nicholas Minh Abell Tran
Washington University in St. Louis

WASHINGTON UNIVERSITY IN SAINT LOUIS

Division of Biology and Biomedical Sciences

Dissertation Examination Committee:

Shiming Chen, Chair
Rajendra Apte
David Beebe
Joseph Corbo
Vladimir Kefalov
Kristen Kroll

Understanding *CRX*-Associated Retinopathies Using Animal Models

By

Nicholas Minh Abell Tran

A dissertation presented to the
Graduate School of Arts and Sciences
of Washington University in
partial fulfillment of the
requirements for the degree
of Doctor of Philosophy

December 2013

Saint Louis, MO

Table of Contents:

List of Figures

List of Tables

List of abbreviations

Animal genotypes- *wild type (WT), heterozygous (het), homozyous (hom),* **Mice**: *Knock OUT (KO), Knock IN (K-IN), Crx Knock OUT (Crx KO,* het*: +/-,* hom: *-/-), Crx^{E168d2} (*het: *E168d2/+,*hom: *E168d2/d2), Crx^{E168d2} (*het: *E168d2neo/+,* hom: *E168d2neo/d2neo), Crx^{R90W} (*het: *R90W/+,* hom: *R90W/W), Crx^{R90W} (*het: *R90Wneo/+,* hom: *R90Wneo/Wneo), Nrl Knock OUT (Nrl KO,* hom: *Nrl -/-),* **Cat:** *Rod cone dysplasia (Crx^{Rdy})*

Retinal layers/features: retinal pigmented epithelium (RPE), outer limiting membrane (OLM), outer segment (OS), inner segment (IS), outer nuclear layer (ONL), outer plexiform layer (OPL), inner nuclear layer (INL), inner plexiform layer (IPL), ganglion cell layer (GCL)

Retinal cell types: photoreceptors (PR), short wavelength cones (S-cones), middle wavelength (M-cones), coexprressing cones (M/S cones), bipolar cells (BP), ganglion cells (GC)

Experimental procedures: Immunofluorescence (IF), Immunohistochemistry (IHC), Western blot (WB), electroretinogram (ERG), chromatin immunoprecipitation (ChIP), dual-luciferase assays (LUC), electron mobility shift assay (EMSA), quantitative reverse transcriptase polymerase chain reaction (qRT-PCR), next generation mRNA sequencing (RNA-Seq), light damage (LD), terminal deoxynucleotidyl transferase dUTP nick end labeling (*TUNEL*), transmission electron microscopy (TEM), Cell Specific Expression Analysis tool (CSEA), kilo

Reagants: Hematoxylin and Eosin (H&E), 13-cis retinoic acid (13-cis RA), recombinant adeno-associated virus (*rAAV*), peanut agglutanin (PNA), human embryonic kidney 293 cells (HEK 293), 5'-bromouridine (*BrU*)

Statistical terms: p-value (p-val or p), standard deviation (SD or STDEV), standard error of the mean (SEM), false discovery rate (FDR), fold-change (FC), counts per million (CPM), reads per kilobase per million (RPKM)

Gene symbols*: cone-rod homeobox (Crx), orthodenticle homolog 2 (Otx2), neural retina leucine zipper gene (Nrl), nuclear receptor subfamily 2, group E, member 3 (Nr2e3), RAR-related orphan receptor alpha (RORα), RAR-related orphan receptor beta (RORβ), retinoid X receptor gamma (RXRγ), thyroid hormone receptor, beta (Trb2 or Thrb2), cone arrestin (Carr or mCarr), opsin 1 (cone pigments), medium-wave-sensitive (Opn1mw or MOP), opsin 1 (cone pigments), short-wave-sensitive (Opn1sw or SOP), rhodopsin (Rho), rhodopsin kinase (RK), guanine neucleotide binding protein, alpha transducing 1 (Gnat1), guanine neucleotide binding protein, alpha transducing 2 (Gnat2), phosphodiesterase 6C, cGMA-specifc, cone, alpha prime (Pde6c), phosphodiesterase 6h, cGMA-specifc, cone, gamma (Pde6h), phosphodiesterase 6C, cGMA-specifc, rod, alpha (Pde6a), cyclic nucleotie gated channel beta 3 (Cngb3), CREB binding protein (Cbp), E1A binding protein (p300), K(lysine) acetyletransferase 2A (Gcn5), orthodentricle (Otd/Otx), Green fluorescent protein (Gfp), retinol bindin protein 3, interstitial (Rbp3), recoverin (Rcvrn), ubiquitin B (Ubb), tubulin, alpha 1b (Tuba1b), glyceraldehyde-3-phosphate dehydrogenase (Gapdh), Beta actin (β-actin)*

Note: Symbols for the proteins translated from genes listed above are written with the same text as gene symbols but in non-italicized all-capital letters.

Disease terms: autosomal dominat (ad), autosomal recessive (ar), cone-rod dystrophy (CoRD), Leber congenital amaurosis (LCA), retinitis pigmentosa (RP)

Protein terms: Amino acid (AA), homeodomain (HD), gluatmine rich (Gln), orthodentricle-tail (OTX-tail)

DNA terms: base pair (bp), messenger RNA (mRNA), Rhodopsin regulatory element containing CRX binding sites (*BAT-1*), Rhodopsin promoter-driven luciferase reporter (*Br130*), 500 bp *Crx* promoter (*0.5K Crx*), Chicken β-actin promoter expression vector (*pCAG* or *U11*), Chicken β-actin promoter expression vector, internal ribosomal entry site *Gfp* (*pCAGIG*), Rhodopsin kinase promoter (*Grk*), pcDNA vector CMV promoter, Xpress epitope tag, His Tag 6x (*pcDNA3.1hisc*), short-hairpin RNA (*shRNA*)

Ages/times: postnatal day (P), week (wk), month (mo), year (yr), minute (min), hour (hr)

Retinal regions: dorsal (D), ventral (V), nasal/temporal (N/T), central (C)

Acknowledgements

First and foremost, I would like to thank Shiming Chen for being the most outstanding mentor a graduate student could ask for. The successes of this project come from your thoughtful support and guidance. You have inspired, challenged and motivated me to become a better scientist and for that, I cannot thank you enough. I would like to thank Anne Hennig, who welcomed and helped integrate me into Chen lab. Thank you for helping me learn/do/fix/buy just about everything in lab an in editing proposals, papers, etc. on countless numbers of occasions. Thank you to Xiadong Zhang, Diana Brightman, Philip Ruzycki and Alan Zhang for being fantastic colleagues and collaborators, helping me every day in lab and creating a great environment to work in. Thank you to Hui Wang and Mingan Yang for your assistance and for keeping the lab running smoothly. Thank you to my thesis committee, in particular my committee chair, David Beebe, for your thoughtful guidance and support. Thank you to Belinda Dana and Frank Schottler of the DOVS histology core for all of your help with IHC and EM experiments. Thank you to Nobish Varghese, Mukesh Sharma, Rakesh Nagarajan, Julie Huecker, Mae Gordon, Simon Peterson-Jones and Laurence Occelli for being outstanding collaborators and helping push this project further than otherwise possible. Thank you to Jim Skeath, Tim Schedl, Melanie Puhar and the entire Molecular Genetics and Genomics program. Thank you to Washington University, the Department of Ophthalmology and Visual Science and the Division of Comparative Medicine. Finally, thank you to my peers including the 2010 FIVR fellows and Elizabeth Atkinson, David Grotsky, Vanessa Ridaura, Erica Schoeller, Maxim Schillebeeckx, Anthony Tubbs, Beth Tuck for all of the years of friendship and support.

"If I have seen further it is by standing on the shoulders of giants." -Isaac Newton

None of this work is possible without the immense efforts and support of all of my colleagues listed above. I'm thankful to have had the opportunity to work with you and have you in my life.

ABSTRACT OF THE DISSERTATION

Understanding *CRX*-Associated Retinopathies

Using Animal Models

By

Nicholas Tran

Doctor of Philosophy in Molecular Genetics and Genomics

Washington University in Saint Louis, 2013

Professor Shiming Chen, Chair

Cone-rod homeobox (CRX) protein is a "paired-like" homeodomain transcription factor that is essential for regulating rod and cone photoreceptor transcription. Mutations in human *CRX* are associated with the dominant retinopathies Retinitis Pigmentosa (RP), Cone-Rod Dystrophy (CoRD) and Leber Congenital Amaurosis (LCA), with variable severity. The goal of my dissertation project was to develop and characterize animal models to understand genetic mechanisms of phenotypic diversity in *CRX*-associated disease. Heterozygous *Crx Knock-Out* (*KO*) mice ("*+/-*") have normal vision as adults and fail to model the dominant human disease.

We generated two *Crx Knock-IN (K-IN)* mouse models: Crx^{E168d2} (*"E168d2"*) and Crx^{R90W} (*"R90W"*), which carry distinct types of mutations and are associated with retinopathies of differing severity. As seen in human patients, heterozygous *E168d2* ("*E168d2/+*") but not *R90W* (*"R90W/+"*) mice show severely impaired retinal function, while mice homozygous for either mutation are blind and undergo rapid photoreceptor degeneration. Careful morphological and biochemical characterization of *K-IN* mice and their associated mutant CRX proteins reveals that they cause disease through distinct molecular mechanisms. Unexpectedly, we also identified that *E168d2/+* mice express more mutant CRX protein than wild-type CRX resulting in an allelic imbalance favoring the mutant protein. Characterization of a *Crx* mutant feline model,

Crx^{Rdy}, *in vivo* and several *Crx* mutants *in vitro* reveals CRX overexpression may be a conserved mechanism. *E168d2neo/+,* a subline of *E168d2* with reduced mutant allele expression, displays a much milder retinal phenotype, demonstrating mutant allele expression level may be a critical genetic modifier of disease severity. Our studies indentify genetic mechanisms contributing to phenotypic diversity of *CRX*-associated disease, improve understanding of disease pathology and allow for the preliminary testing of novel therapeutic approaches.

Chapter I

-

Introduction & Background

Author: Nicholas Tran

Chapter I

1.1. Establishing functional rod and cone photoreceptors in mammals

The first step in forming vision is the conversion of light into an interpretable neurological signal. In the vertebrate retina, the ciliary rod and cone photoreceptors carry out this unique task in a process called phototransduction.[1] Rods and cones are specially tuned for different forms of phototransduction. Rods are incredibly sensitive, capable of responding to a single photon of light, but have slow kinetics. Rods support dim light and night vision. Cones are less sensitive than rods but have much faster kinetics. Additionally, many species have multiple subtypes of cones with different spectral sensitivities. Cones support bright light and color vision. To achieve phototransduction, ciliary vertebrate photoreceptors elaborate a highly specialized organelle called the outer segment. Within this organelle are thousands of stacked membranes each of which is packed with visual pigment G-protein coupled receptors called opsins, which bind a photosensitive chromophore. The chromophore isomerizes in response to light causing a conformational change in the opsin protein which sends a signaling cascade through a series of enzymes and proteins leading to the hyperpolerization of the cell. The large surface area of the outer segment and the amplification of the signal confer amazing sensitivity, with human rods capable of responding to a single photon of light. Many of the components of the outer segment and the phototransduction pathway are specifically expressed in photoreceptors and solely function within this pathway.[2] Because of this, the precise regulation of photoreceptor gene expression is absolutely critical to their functionality.

In mammalian rods and cones, the precise coordination of gene expression is dependent on a network of transcription factors (Fig. 1.1).[3,4] These transcription factors work in concert to activate rod genes in rods, cone genes in cones and repress genes of the opposite cell type. During retinal development, a cascade of transcription factors is expressed in a subset of retinal progenitor cells which gives rise to photoreceptors. In these cells, the homeodomain (HD) transcription factor OTX2 activates another HD transcription factor, CRX to initiate differentiation along the photoreceptor lineage. CRX, which is expressed in both

developing and mature rods and cones, promotes their terminal differentiation from photoreceptor precursors and their long-term survival. CRX expression is followed by the expression of rod-specific (including RORβ, NRL and NR2E3) and cone-specific (including RORα, TRβ2, RXRγ and COUP TFs) transcription factors in their corresponding cell types. CRX works synergistically with both cell-specific and ubiquitous transcription factors to coordinate rod and cone gene expression including the expression of phototransduction genes[4–8].

1.2. Molecular function of CRX

CRX (Accession: AAH53672.1) is an Otd/OTX-like 'paired' HD transcription factor that is preferentially expressed in vertebrate rod and cone photoreceptor cells in the retina and pinealocytes in the brain[6,7]. CRX plays an essential role in the establishment and maintenance of gene expression in mammalian rod and cone photoreceptors[9] and the pineal gland[10]. The molecular function of CRX is highly conserved amongst mammals including humans, mice, and cats.[6,7,11] Paralogues of CRX/OTX have been found to maintain similar roles in the photoreceptors of the evolutionarily divergent vertebrates fish[12], amphibians[13] and invertebrates *Drosophila*[14] and *Amphioxus*[15]. *CRX* encodes a 299 amino acid protein that contains a homeodomain (HD) near its N-terminus that is responsible for DNA binding (Fig 1.2)[6,16]. The HD is followed by glutamine rich (Gln), basic, WSP and OTX-tail motifs[6,16]. Previous studies show that CRX binds to photoreceptor target genes[7,8,17–23] and can directly activate the promoters of target genes *in vitro*, including its own promoter and *Rhodopsin*[6,18,24,25]. CRX is thought to mainly act as a transcriptional activator in photoreceptors based on expression profiling of the CRX knock-out (KO) mouse[2,3,9], but is associated with repression in certain genomic contexts[8]. Transactivation activity is dependent on the C terminal region of CRX (from the basic to the OTX-tail domains)[18]. CRX activates gene expression by interacting with the histone acetyltransferases GCN5, CBP and p300 (Accessions: AAC50641.1, AAC17736.1,

NP_001420.2, respectively)[26], promoting histone acetylation at target gene promoters[4,26] and mediating enhancer/promoter intrachromosomal looping interactions[27] of target photoreceptor genes. These events in chromatin remodeling and transcriptional activation are sequentially regulated during retinal development[26]. CRX also maintains specific interactions with transcriptional co-regulators including the rod-specific transcription factors NRL (Accession: NP_006168.1)[28,29] and NR2E3 (Accession: AAH41421.1)[30,31] to coordinately control photoreceptor gene expression. NRL has been shown to activate rod gene expression[32] while NR2E3 has dual activator/repressor activity[30,33,34]. CRX, NRL and NR2E3 have been shown to co-occupy target gene promoters and enhancers *in vivo*[23], have synergistic activity in promoting gene expression[35]. Genome wide profiling of CRX[8] and NRL[36] reveal that a high percentage of genes bound by NRL are also bound by CRX. A mouse *KO* of *Nrl* causes a fate switch of rods to a 'cone-like' state[37,38], and the additional loss of CRX in the *Crx* and *Nrl* double *KO* impairs the transcription of cone genes in this retina[3]. Outside of photoreceptors, CRX was found to broadly regulate transcription in the pineal gland[39] and loss of CRX attenuated circadian entrainment in the mouse[9]. These studies suggest that CRX plays a central and critical role in the activation of rod and cone gene expression and also regulates gene expression in the pineal gland.

1.3. *CRX* mutations associated with dominant Retinitis Pigmentosa, Cone-Rod Dystrophy and Leber Congenital Amaurosis

Mutations in human *CRX* (NCBI Reference Sequence: NG_008605.1) have been associated with autosomal dominant forms of the retinal degenerative diseases Retinitis Pigmentosa (adRP), Cone-Rod Dystrophy (adCoRD) and Leber Congenital Amaurosis (adLCA), with different ages of onset and severity[29,40–61]. *CRX* is the only gene associated with all three diseases[41,43,59,62], demonstrating its central role in rod and cone integrity. However, null

mutations in *CRX* may not be responsible for severe dominant disease. A null mutation in *CRX, P9ins1,* was associated with LCA in a heterozygous patient but the patient's father, a carrier of *P9ins1*, had a normal ocular phenotype suggesting either recessive or multigenic inheritance[60]. The phenotypes of the human and mouse heterozygous null mutations suggest that haploinsufficiency is unlikely to underlie the severe forms of dominant *CRX*-associated disease.

Dominant disease-causing human *CRX* mutations primarily fall into two classes (Fig. 1.2): frameshift mutations (blue text) mostly in the transactivation domains and amino acid substitution mutations (black text) mostly within the DNA binding homeodomain. Both classes are expected to produce mutant forms of CRX protein that are pathogenic. Supporting this hypothesis, the frameshift mutations *E168d1*, *E168d2*, *G217d1* and several other truncation mutations were linked to early onset (0-20 years) severe adCoRD/adLCA[40–49,51,53–55,62,63] and *A196d4* was associated with adult onset adCoRD[64]. The substitution mutations, *R41W*, *R41Q, R90W* and several others were associated with late onset (~40-60 years old) adCoRD[40,49,53,58,61,62], while *K88N* was associated with adLCA[65]. A patient homozygous for *R90W* was also diagnosed with autosomal recessive LCA[61]. Generally, frameshift mutations in the transactivation domains of *CRX* are associated with more early onset and severe dominant retinopathies than the substitution mutations, suggesting these two types of mutations may represent distinct classes and contribute to the phenotypic diversity of *CRX*-associated disease.

1.4. Distinct molecular activity of mutant CRX proteins

Most of the frameshift mutations are located in the transactivation domains of *CRX* (Fig. 1.2) and lead to the formation of a novel early stop codon typically resulting in the early truncation of CRX. These truncated mutant proteins were predicted to lose transactivation activity but maintain DNA-binding activity, since they have an intact homeodomain. While most frameshift mutations are predicted to produce a truncated CRX protein, there are multiple mutations which could generate mutant proteins with novel amino acid tails of varying length

(summarized in Fig. 1.3). It is unknown how these unique C-terminal tails affect the function of CRX.

Truncated CRX proteins resulting from the frameshift mutations *E168d1*, *E168d2*, *A196d4* and *G217d1* lost the ability to transactivate the promoter of *Rhodopsin* (*Rho*) in HEK293 cell transient transfection assays, but are expected to bind DNA normally since CRX 1-107, a complete activation domain truncation mutant, retained CRX target binding activity[18]. It was predicted that these truncated mutant proteins could interfere with the function of WT CRX by an antimorphic mechanism and cause a severe dominant retinal phenotype[18]. Furthermore, rescue experiments of the *otd*^{uvi} phenotype in *Drosophila* demonstrate the CRX truncation mutation *I138*^{fs48} possessed dominant-negative activity on target gene expression[14], providing experimental evidence for an antimorphic mechanism for this class of *CRX* mutations.

Four substitution mutations in the homeodomain: *R41W*, *R41Q, R90W*[28,61,64], and *K88N*[29], also reduced the ability of CRX to bind to and transactivate the *Rhodopsin* promoter. *R41Q* and *R90W* both reduced CRX:NRL protein interaction[28], while *K88N* additionally interfered with basal NRL-mediated transcription[65]. *R41W*, *R41Q*, and *R90W* were predicted to represent hypomorphic alleles associated with either recessive or less severe dominant forms of disease, while *K88N* was predicted to possess antimorphic activity on NRL function causing a stronger phenotype. In contrast, four other substitution mutations associated with early onset adCoRD/LCA: *E80A*[40,49,62,66], *A56T*[47], *A158T* and *V242M*[58] did not lose DNA binding or transactivating activity[67]. *In vivo* rescue experiments in *Drosophila* also demonstrate that *E80A* but not *R90W* or *K88N* possesses some dominant-negative activity on *Rh5* expression[14]. Collectively these experiments support our hypothesis that substitution mutations may cause disease through several distinct mechanisms.

Chapter I

1.5. Current and proposed models for *CRX*-associated retinopathy

The role of *Crx* in retinal development was first characterized *in vivo* by the generation of a *Crx Knock-OUT* (*KO*) mouse[9]. In the homozygous *Crx KO* mouse ("-/-"), photoreceptors fail to form outer segments (OS), a highly specialized photoreceptor organelle which contains visual pigment opsins and other proteins required for phototransduction. As a result, -/- photoreceptors do not function, form abnormal synapses, and undergo progressive degeneration[9,68]. Gene expression profile studies showed that -/- mice have severely reduced expression of many photoreceptor specific genes[2,3,69]. Most of these genes are direct CRX targets as detected by ChIP-seq analyses of the genomic CRX binding profile in the mouse retina[8].

In addition to the *Crx KO* mouse, the role of CRX and the impact of mutant CRX proteins on retinal development has been studied in multiple animal models. While mouse retinal development is guided by a trio of 'paired-like' homeodomain transcription factors OTX1, OTX2 and CRX[6,7,13,70], in *Drosophila* the roles of these three genes are replaced by a single factor, *Otd*[71,72], an paired-like homeobox transcription factor family member. Human CRX and OTX2 were able to rescue different aspects of the Otd^{uvi} photoreceptor phenotype, suggesting distinct, yet overlapping functions for CRX and OTX2[14]. In addition, it was found that the *CRX* mutants *E80A*, $I138^{fs48}$ and *R90W* had partial and overlapping rescue function on photoreceptor morphology and gene expression, while *K88N* was unable to rescue the Otd^{uvi} phenotype. Of these mutations, only *E80A* and $I138^{fs48}$ possessed dominant-negative activity, with $I138^{fs48}$ having the strongest effect[14]. In other studies, a morpholino knockdown of *Zebrafish Crx* showed that CRX was critical for photoreceptor and bipolar cell development[12] and lipofection of *Otx5b*, a homologue of *Crx*, in *Xenopus Laevis* biased retinal progenitors to the photoreceptor fate[73].

The *in vivo* studies detailed above have helped to elucidate the roles of CRX and CRX homologues in retinal development. They demonstrate CRX's central role in photoreceptor

development and gene expression, which is critical to the formation of functional photoreceptors and vision. However, these animal studies fail to provide accurate models of dominant *CRX*-associated retinopathies, limiting their usefulness for translational research. The heterozygous *Crx KO* mouse ("+/-"), only shows a slight delay in photoreceptor development and largely display normal morphology, gene expression and retinal function in adulthood[9], suggesting that severe dominant disease may result from the activity of mutant CRX proteins. Supporting this, the feline model, Crx^{Rdy}, was found to carry a frameshift mutation in *Crx*, *n.546delC,* which was predicted to generate a truncated CRX protein[11]. Crx^{Rdy} cats display severe dominant impairment of retinal function, photoreceptor degeneration and reduced Rhodopsin expression, all characteristic of adLCA[74–77]. The phenotype of the Crx^{Rdy} cat closely matches human retinopathy for similar-type truncation mutations, indicating it is an accurate model of dominant *CRX*-associated disease.

Currently, there is no treatment strategy for *CRX*-associated diseases. Establishing animal models that accurately recapitulate different disease mechanisms is critical for developing and testing novel therapeutic approaches. The Crx^{Rdy} cat demonstrates the importance of tailoring animal models to the specific types of mutations identified in human patients. However, the high cost, slow breeding and lack of genetic tools for research in cats, are prohibitive for performing advanced pathological and biochemical studies in larger animals. Additionally, the Crx^{Rdy} cat only represents one type of *Crx* mutation and human disease is associated with multiple distinct types.

To address these issues, we sought to generate mechanistically distinct mouse models of *CRX*-associated disease to identify specific differences in pathology and molecular function of mutant CRX proteins. Here we report the generation of two *Knock-IN (K-IN)* mouse models carrying different types of human disease-causing *Crx* mutations and present a detailed

morphological, functional and biochemical characterization of these mouse models. The frameshift mutation *E168d2* produces a severe dominant phenotype through an antimorphic mechanism, while the substitution mutation *R90W* produces a very mild late-onset 'CoRD-like' phenotype in heterozygotes and 'LCA'-like disease in homozygotes. Furthermore, these studies revealed that the expression level of a mutant allele can dramatically affect the disease phenotype, providing insight into the phenotypic variability of disease, as well as, potential treatment strategies.

Chapter I

References for Chapter I

1. Hubbell, WL. Bownds, M. Visual Transduction In Vertebrate Photoreceptors. *Ann. Rev. Neurosci.* **2,** 17–34 (1979).

2. Blackshaw, S., Fraioli, R. E., Furukawa, T. & Cepko, C. L. Comprehensive analysis of photoreceptor gene expression and the identification of candidate retinal disease genes. *Cell* **107,** 579–589 (2001).

3. Hsiau, T. H. *et al.* The cis-regulatory logic of the mammalian photoreceptor transcriptional network. *PLoS One* **2e643,** (2007).

4. Hennig, A. K., Peng, G. H. & Chen, S. Regulation of photoreceptor gene expression by Crx-associated transcription factor network. *Brain Res* **1192,** 114–133 (2008).

5. Hennig, A. K., Peng, G.-H. & Chen, S. Transcription coactivators p300 and CBP are necessary for photoreceptor-specific chromatin organization and gene expression. *PLoS One* **8,** e69721 (2013).

6. Chen, S. *et al.* Crx, a novel Otx-like paired-homeodomain protein, binds to and transactivates photoreceptor cell-specific genes. *Neuron* **19,** 1017–30 (1997).

7. Furukawa, T., Morrow, E. M. & Cepko, C. L. Crx, a novel otx-like homeobox gene, shows photoreceptor-specific expression and regulates photoreceptor differentiation. *Cell* **91,** 531–541 (1997).

8. Corbo, J. C. *et al.* CRX ChIP-seq reveals the cis-regulatory architecture of mouse photoreceptors. 1512–1525 (2010). doi:10.1101/gr.109405.110.CRX

9. Furukawa, T., Morrow, E. M., Li, T., Davis, F. C. & Cepko, C. L. Retinopathy and attenuated circadian entrainment in Crx-deficient mice. *Nat Genet* **23,** 466–470 (1999).

10. Rovsing, L. *et al.* Crx broadly modulates the pineal transcriptome. *J. Neurochem.* **119,** 262–74 (2011).

11. Menotti-Raymond M, Deckman KH, David VA, Myrkalo J, O'Brien SJ, N. K. Mutation discovered in a feline model of human congenital retinal blinding disease. *Invest Ophthalmol Vis Sci* **[Epub ahea,** (2010).

12. Shen, Y. & Raymond, P. a. Zebrafish cone-rod (crx) homeobox gene promotes retinogenesis. *Dev. Biol.* **269,** 237–51 (2004).

13. Plouhinec, J.-L. *et al.* The mammalian Crx genes are highly divergent representatives of the Otx5 gene family, a gnathostome orthology class of orthodenticle-related homeogenes involved in the differentiation of retinal photoreceptors and circadian entrainment. *Mol. Biol. Evol.* **20,** 513–21 (2003).

14. Terrell, D. *et al.* OTX2 and CRX rescue overlapping and photoreceptor-specific functions in the Drosophila eye. *Dev. Dyn.* **241,** 215–28 (2012).

15. Vopalensky, P. *et al.* Molecular analysis of the amphioxus frontal eye unravels the evolutionary origin of the retina and pigment cells of the vertebrate eye. *Proc. Natl. Acad. Sci. U. S. A.* **109,** 15383–8 (2012).

16. Fei, Y. & Hughes, T. E. Nuclear trafficking of photoreceptor protein crx: the targeting sequence and pathologic implications. *Invest. Ophthalmol. Vis. Sci.* **41,** 2849–56 (2000).

17. Chen, S. *et al.* Functional analysis of cone-rod homeobox (CRX) mutations associated with retinal dystrophy. *Hum Mol Genet* **11,** 873–884 (2002).

18. Chau, K. Y., Chen, S., Zack, D. J. & Ono, S. J. Functional domains of the cone-rod homeobox (CRX) transcription factor. *J. Biol. Chem.* **275,** 37264–70 (2000).

19. Boatright, J. H. *et al.* A major cis activator of the IRBP gene contains CRX-binding and Ret-1/PCE-I elements. *Mol. Vis.* **3,** 15 (1997).

20. Bobola, N. *et al.* OTX2 homeodomain protein binds a DNA element necessary for interphotoreceptor retinoid binding protein gene expression. *Mech. Dev.* **82,** 165–9 (1999).

21. Fei, Y. *et al.* Functional dissection of the promoter of the interphotoreceptor retinoid-binding protein gene: the cone-rod-homeobox element is essential for photoreceptor-specific expression in vivo. *J. Biochem.* **125,** 1189–99 (1999).

22. Livesey, F. J., Furukawa, T., Steffen, M. A., Church, G. M. & Cepko, C. L. Microarray analysis of the transcriptional network controlled by the photoreceptor homeobox gene Crx. *Curr Biol* **10,** 301–310 (2000).

23. Peng, G. H. & Chen, S. Chromatin immunoprecipitation identifies photoreceptor transcription factor targets in mouse models of retinal degeneration: new findings and challenges. *Vis. Neurosci.* **22,** 575–586 (2005).

24. Kimura, a. Both PCE-1/RX and OTX/CRX Interactions Are Necessary for Photoreceptor-specific Gene Expression. *J. Biol. Chem.* **275,** 1152–1160 (2000).

25. Langmann, T. *et al.* CRX controls retinal expression of the X-linked juvenile retinoschisis (RS1) gene. *Nucleic Acids Res.* **36,** 6523–34 (2008).

26. Peng, G. H. & Chen, S. Crx activates opsin transcription by recruiting HAT-containing co-activators and promoting histone acetylation. *Hum Mol Genet* **16,** 2433–2452 (2007).

27. Peng, G.-H. & Chen, S. Active opsin loci adopt intrachromosomal loops that depend on the photoreceptor transcription factor network. *Proc. Natl. Acad. Sci. U. S. A.* **108,** 17821–6 (2011).

28. Mitton, K. P. *et al.* The leucine zipper of NRL interacts with the CRX homeodomain. A possible mechanism of transcriptional synergy in rhodopsin regulation. *J. Biol. Chem.* **275,** 29794–9 (2000).

29. Nichols, L. L. *et al.* Two novel CRX mutant proteins causing autosomal dominant Leber congenital amaurosis interact differently with NRL. *Hum. Mutat.* **31,** E1472–83 (2010).

30. Peng, G. H., Ahmad, O., Ahmad, F., Liu, J. & Chen, S. The photoreceptor-specific nuclear receptor Nr2e3 interacts with Crx and exerts opposing effects on the transcription of rod versus cone genes. *Hum. Mol. Genet.* **14,** 747–764 (2005).

31. Roduit, R., Escher, P. & Schorderet, D. F. Mutations in the DNA-binding domain of NR2E3 affect in vivo dimerization and interaction with CRX. *PLoS One* **4,** e7379 (2009).

32. Rehemtulla, a *et al.* The basic motif-leucine zipper transcription factor Nrl can positively regulate rhodopsin gene expression. *Proc. Natl. Acad. Sci. U. S. A.* **93,** 191–5 (1996).

33. Webber, A. L. *et al.* Dual role of Nr2e3 in photoreceptor development and maintenance. *Exp. Eye Res.* **87,** 35–48 (2008).

34. Chen, J., Rattner, A. & Nathans, J. The rod photoreceptor-specific nuclear receptor Nr2e3 represses transcription of multiple cone-specific genes. *J. Neurosci.* **25,** 118–129 (2005).

35. Mitton, K. P. *et al.* The leucine zipper of NRL interacts with the CRX homeodomain. A possible mechanism of transcriptional synergy in rhodopsin regulation. *J. Biol. Chem.* **275,** 29794–9 (2000).

36. Hao, H. *et al.* Transcriptional regulation of rod photoreceptor homeostasis revealed by in vivo NRL targetome analysis. *PLoS Genet.* **8,** e1002649 (2012).

37. Daniele, L. L. *et al.* Cone-like morphological, molecular, and electrophysiological features of the photoreceptors of the Nrl knockout mouse. *Invest Ophthalmol Vis Sci* **46,** 2156–2167 (2005).

38. Yoshida, S. *et al.* Expression profiling of the developing and mature Nrl-/- mouse retina: identification of retinal disease candidates and transcriptional regulatory targets of Nrl. *Hum. Mol. Genet.* **13,** 1487–503 (2004).

39. Rovsing, L. *et al.* Crx broadly modulates the pineal transcriptome. *J. Neurochem.* **119,** 262–74 (2011).

40. Sohocki, M. M. *et al.* A range of clinical phenotypes associated with mutations in CRX, a photoreceptor transcription-factor gene. *Am J Hum Genet* **63,** 1307–1315 (1998).

41. Jacobson, S. G. *et al.* Retinal degenerations with truncation mutations in the cone-rod homeobox (CRX) gene. *Invest Ophthalmol Vis Sci* **39,** 2417–2426 (1998).

42. Hanein, S. *et al.* Leber congenital amaurosis: comprehensive survey of the genetic heterogeneity, refinement of the clinical definition, and genotype-phenotype correlations as a strategy for molecular diagnosis. *Hum. Mutat.* **23,** 306–17 (2004).

43. Dharmaraj, S. R. *et al.* Mutational analysis and clinical correlation in Leber congenital amaurosis. *Ophthalmic Genet.* **21,** 135–50 (2000).

44. Galvin, J. a, Fishman, G. a, Stone, E. M. & Koenekoop, R. K. Evaluation of genotype-phenotype associations in leber congenital amaurosis. *Retina* **25,** 919–29

45. Nakamura, M., Ito, S. & Miyake, Y. Gene in a Japanese Patient With. **24,** 465–467 (1998).

46. Zhang, Q. *et al.* Screening for CRX gene mutations in Chinese patients with Leber congenital amaurosis and mutational phenotype. *Ophthalmic Genet.* **22,** 89–96 (2001).

47. Lotery, a J. *et al.* Mutation analysis of 3 genes in patients with Leber congenital amaurosis. *Arch. Ophthalmol.* **118,** 538–43 (2000).

48. Wang, P., Guo, X. & Zhang, Q. Further evidence of autosomal-dominant Leber congenital amaurosis caused by heterozygous CRX mutation. *Graefes Arch. Clin. Exp. Ophthalmol.* **245,** 1401–2 (2007).

49. Huang, L. *et al.* CRX variants in cone-rod dystrophy and mutation overview. *Biochem. Biophys. Res. Commun.* **426,** 498–503 (2012).

50. Tzekov, R. T. *et al.* Autosomal dominant retinal degeneration and bone loss in patients with a 12-bp deletion in the CRX gene. *Invest. Ophthalmol. Vis. Sci.* **42,** 1319–27 (2001).

51. Tzekov, R. T., Sohocki, M. M., Daiger, S. P. & Birch, D. G. Visual phenotype in patients with Arg41Gln and ala196+1bp mutations in the CRX gene. *Ophthalmic Genet.* **21,** 89–99 (2000).

52. Koenekoop, R. K., Loyer, M., Dembinska, O. & Beneish, R. Mutation report Visual improvement in Leber congenital amaurosis and the CRX genotype. 49–60 (2002).

53. Paunescu, K., Preising, M. N., Janke, B., Wissinger, B. & Lorenz, B. Genotype-phenotype correlation in a German family with a novel complex CRX mutation extending the open reading frame. *Ophthalmology* **114,** 1348–1357.e1 (2007).

54. Walia, S. *et al.* Visual acuity in patients with Leber's congenital amaurosis and early childhood-onset retinitis pigmentosa. *Ophthalmology* **117,** 1190–8 (2010).

55. Den Hollander, A. I., Roepman, R., Koenekoop, R. K. & Cremers, F. P. M. Leber congenital amaurosis: genes, proteins and disease mechanisms. *Prog. Retin. Eye Res.* **27,** 391–419 (2008).

56. Cl, F. *et al.* Conerod dystrophy due to mutations in a novel photoreceptor-specific homeobox gene (CRX) essential for maintenance of the photoreceptor. *Cell* **91,** 543–553 (1997).

57. Freund, C. L. *et al.* De novo mutations in the CRX homeobox gene associated with Leber congenital amaurosis. *Hum. Mutat.* **18,** 550–551 (2001).

58. Swain, P. K. *et al.* Mutations in the cone-rod homeobox gene are associated with the cone-rod dystrophy photoreceptor degeneration. *Neuron* **19,** 1329–36 (1997).

59. Berger, W., Kloeckener-Gruissem, B. & Neidhardt, J. The molecular basis of human retinal and vitreoretinal diseases. *Prog. Retin. Eye Res.* **29,** 335–75 (2010).

60. E, S. *et al.* A CRX null mutation is associated with both Leber congenital amaurosis and a normal ocular phenotype. *Invest Ophthalmol Vis Sci* **41,** 2076–2079 (2000).

61. Swaroop, A. *et al.* Leber congenital amaurosis caused by a homozygous mutation (R90W) in the homeodomain of the retinal transcription factor CRX: direct evidence for the involvement of CRX in the development of photoreceptor function. *Hum Mol Genet* **8,** 299–305 (1999).

62. Rivolta C, Berson El, D. D. Dominant Leber congenital amaurosis, cone-rod degeneration, and retinitis pigmentosa caused by mutant versions of the transcription factor CRX. *Hum Mutat* **18,** 488–498 (2001).

63. Freund, C. L. *et al.* Cone-rod dystrophy due to mutations in a novel photoreceptor-specific homeobox gene (CRX) essential for maintenance of the photoreceptor. *Cell* **91,** 543–553 (1997).

64. Chen, S. *et al.* Functional analysis of cone-rod homeobox (CRX) mutations associated with retinal dystrophy. *Hum. Mol. Genet.* **11,** 873–84 (2002).

65. Nichols, L. L. *et al.* Two novel CRX mutant proteins causing autosomal dominant Leber congenital amaurosis interact differently with NRL. *Hum. Mutat.* **31,** E1472–83 (2010).

66. Den Hollander, A. I., Roepman, R., Koenekoop, R. K. & Cremers, F. P. M. Leber congenital amaurosis: genes, proteins and disease mechanisms. *Prog. Retin. Eye Res.* **27,** 391–419 (2008).

67. Pittler, S. J. *et al.* Functional analysis of the rod photoreceptor cGMP phosphodiesterase alpha-subunit gene promoter: Nrl and Crx are required for full transcriptional activity. *J. Biol. Chem.* **279,** 19800–19807 (2004).

68. Morrow, E. M., Furukawa, T., Raviola, E. & Cepko, C. L. Synaptogenesis and outer segment formation are perturbed in the neural retina of Crx mutant mice. *BMC Neurosci* **6,** 5 (2005).

69. Livesey, F. J., Furukawa, T., Steffen, M. A., Church, G. M. & Cepko, C. L. Microarray analysis of the transcriptional network controlled by the photoreceptor homeobox gene Crx. *Curr. Biol.* **10,** 301–310 (2000).

70. Nishida, A. *et al.* Otx2 homeobox gene controls retinal photoreceptor cell fate and pineal gland development. *Nat. Neurosci.* **6,** 1255–1263 (2003).

71. Vandendries, E. R., Johnson, D. & Reinke, R. orthodenticle is required for photoreceptor cell development in the Drosophila eye. *Dev. Biol.* **173,** 243–55 (1996).

72. Ranade, S. S. *et al.* Analysis of the Otd-dependent transcriptome supports the evolutionary conservation of CRX/OTX/OTD functions in flies and vertebrates. *Dev Biol* **315,** 521–534 (2008).

73. Viczian, a. S. XOtx5b and XOtx2 regulate photoreceptor and bipolar fates in the Xenopus retina. *Development* **130,** 1281–1294 (2003).

74. Chong, N. H., Alexander, R. a, Barnett, K. C., Bird, a C. & Luthert, P. J. An immunohistochemical study of an autosomal dominant feline rod/cone dysplasia (Rdy cats). *Exp. Eye Res.* **68,** 51–7 (1999).

75. Leon, a & Curtis, R. Autosomal dominant rod-cone dysplasia in the Rdy cat. 1. Light and electron microscopic findings. *Exp. Eye Res.* **51,** 361–81 (1990).

76. Leon, A. & Curtis, R. Autosomal Qominant Dysplasia findings in the Rdy Cat 2 . Electrophysiological. 489–502 (1991).

77. Jacobson, S. G., Kemp, C. M., Narfström, K. & Nilsson, S. E. Rhodopsin levels and rod-mediated function in Abyssinian cats with hereditary retinal degeneration. *Exp. Eye Res.* **49,** 843–52 (1989).

Fig 1.1)

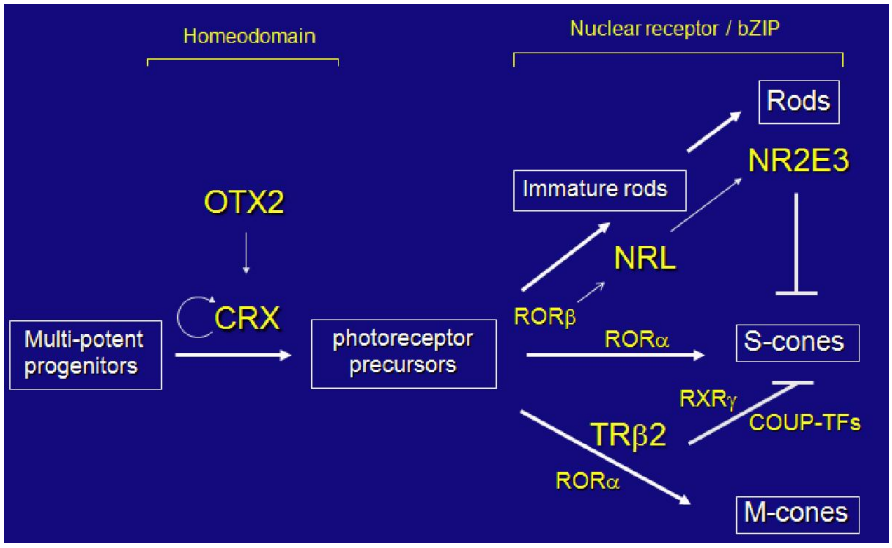

Figure 1.1) Schematic of the photoreceptor transcription factor network. CRX works synergistically with several co-factors to regulate gene expression in mammalian rods and cones.

Fig. 1.2)

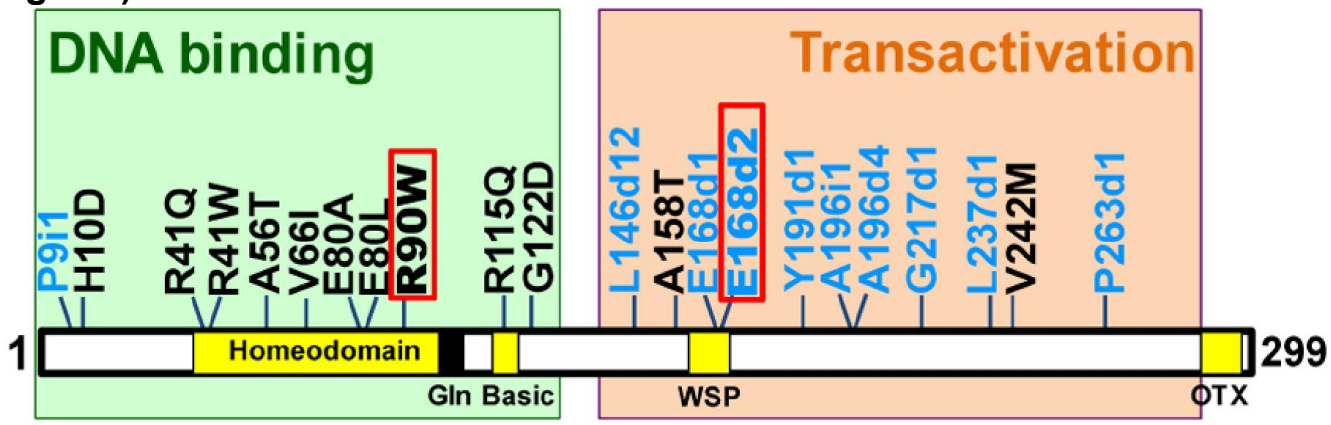

Figure 1.2) Diagram of CRX protein showing regions associated with DNA binding (green box) and transactivation (orange box) and mutations identified from patients with retinopathy. These mutations mainly fall into two classes: amino acid substitutions within the DNA binding region (black text) and frameshift deletions and insertions in the transactivation region (blue text). Two mutations (marked by red box) were selected for generating knock-in mouse models: *E168d2* was predicted to generate a truncated protein that interferes with wild-type CRX function; *R90W* was predicted to generate a protein with reduced ability to bind DNA.

Fig. 1.3)

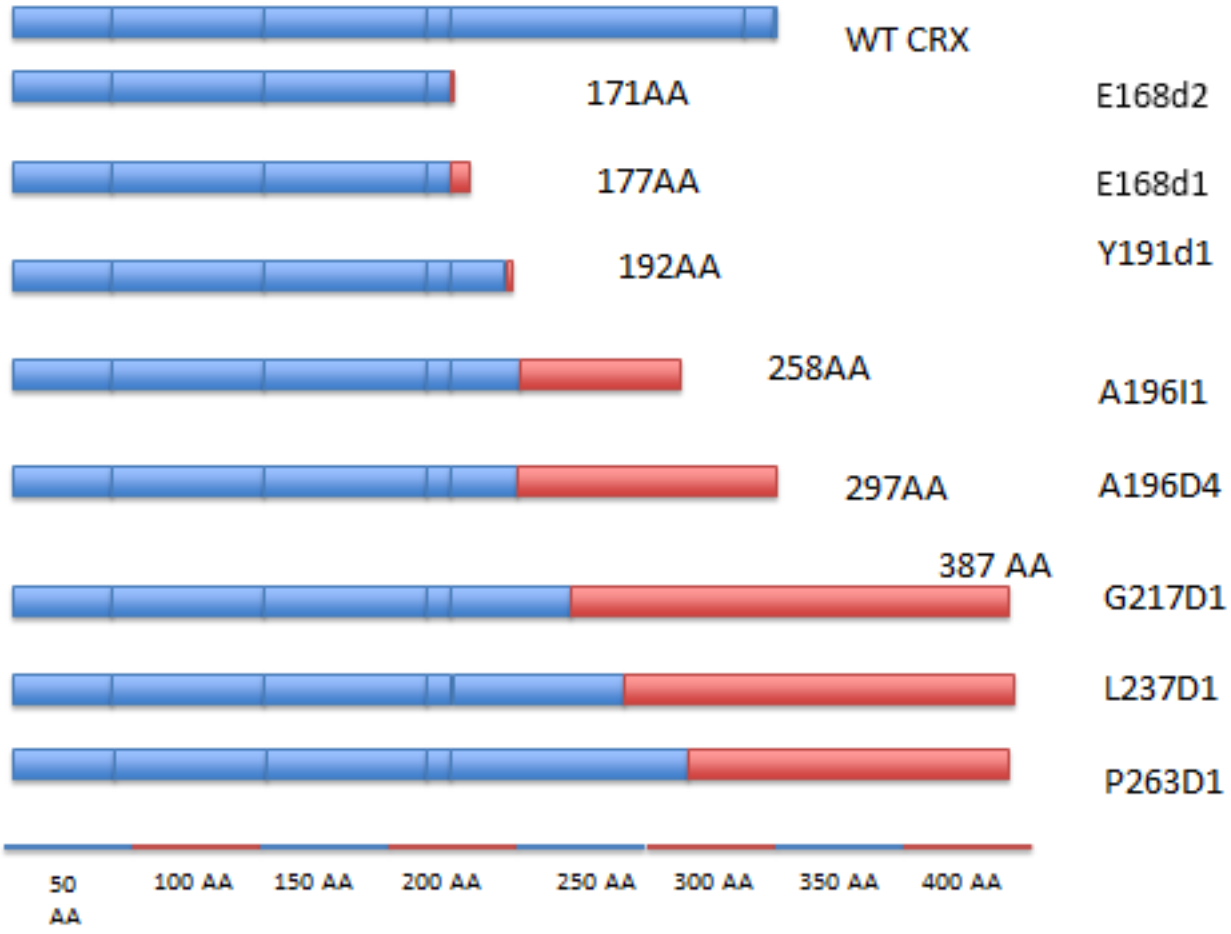

Figure 1.3) Schematic representing the predicted size of mutant CRX proteins based on genomic sequence analysis. The specific CRX mutation is listed on the right. Normal CRX coding regions are shown in blue, novel coding regions are shown in red. A scale bar indicating the amino acid (AA) length is shown at the bottom.

Chapter II

-

Mechanistically Distinct Mouse Models for *CRX*-Associated Retinopathy

Author: Nicholas Tran

Co-authors: Shiming Chen, Anne Hennig, Xiaodong Zhang, Alan Zhang, Julie Huecker

This chapter is adapted from data and analysis contained within:

Tran NM, Zhang A, Zhang X, Huecker J, Hennig A, Chen S Mechanistically Distinct Mouse Models For *CRX*-Associated Retinopathy. PLOS Genetics, *in press*.

Chapter II

Introduction- Generation of *E168d2* and *R90W Knock-IN* mouse models

In this study, we have generated two *Crx K-IN* mouse lines, each carrying a human disease-causing mutation in the mouse allele (Accession: NM_007770.4). Crx^{E168d2} ("*E168d2*") mice carry a 2-bp deletion mutation, *Glu168del2,* which resulted in a codon frameshift and early truncation of the transactivation domains of CRX protein (Fig 1.2, Fig 2.1A-B). Crx^{R90W} ("*R90W*") mice carry *Arg90Trp*, an amino acid substitution mutation in the homeodomain of CRX (Fig 1.2, Fig 2.1A-B). An intermediate subline of each ("*E168d2neo*" and "*R90Wneo*") carrying a *neomycin* (*neo*) cassette in intron 3-4 was also maintained (Fig 2.1A), since the *neo* cassette specifically reduced the expression of the mutant allele (Fig 2.2). The *neo* was removed from the germline by crossing *E168d2neo* and *R90Wneo* mice to the *Sox2-Cre* mouse[1] to generate the final *E168d2* and *R90W* mouse lines (Fig 2.1A). Successful *K-IN* was confirmed by PCR amplification of *neo* (Primer set: Neo F/R) and the respective *Crx* allele (Table 2.1) and Sanger sequencing of homozygous mice (Fig 2.1B).

Results

2.1. Expression of CRX protein and mRNA in *Knock-IN* mice

2.1.i) Mutant CRX protein is overexpressed in *E168d2* but not *R90W* mice

To determine if *E168d2* and *R90W K-IN* mice properly express their respective CRX proteins, immunofluorescence (IF) staining for CRX was performed on paraffin-embedded retinal sagittal sections of P10 mice (Fig 2.2). The mouse monoclonal CRX antibody M02 (Abnova) used recognizes WT (Accession: NP_031796.1) and both mutant forms of CRX. Slides were immunostained in the same batch and imaged using a common exposure. As reported previously[2–4], CRX staining in *WT* retina (Fig 2.2A) was predominantly localized to the outer nuclear layer (ONL), comprised of the rod and cone photoreceptor cell bodies. Less intense CRX staining was also seen in the outer portion of the inner nuclear layer (INL), which is comprised of bipolar and horizontal cell bodies. *E168d2* homozygous (*E168d2*/*d2*") and

heterozygous (*"E168d2/+"*) mouse retinas showed higher intensity CRX staining than *WT*, especially in the ONL (Fig 2.2B&C). The heterozygous *E168d2neo* ("*E168d2neo/+"*) retina on the other hand showed similar intensity CRX staining as *WT* retina (Fig 2.2D vs 2.2A). In contrast, CRX staining in the ONL of *R90W* homozygous ("*R90W/W*") and heterozygous ("*R90W/+"*) mouse retinas was reduced compared to *WT* retinas, although a few cells expressing high levels of CRX are scattered across the ONL (Fig 2.2E&F). This mosaic pattern of variable CRX expression was not seen in *WT* retinas. *Crx Knock-Out* ("-/-") retinas didn't show CRX reactivity in the ONL and served as negative controls (Fig 2.2G). The positive CRX staining in *E168d2/d2* and *R90W/W* retinas suggests that the $CRX^{[E168d2]}$ and $CRX^{[R90W]}$ mutant proteins were expressed in the appropriate cell layers.

The expression levels of WT CRX and mutant $CRX^{[E168d2]}$, $CRX^{[R90W]}$ proteins were compared and quantified in P10 *E168d2* and *R90W K-IN* retinas using quantitative Western blots assayed with the polyclonal CRX 119b-1 antibody[5], which also recognized all forms of CRX proteins assayed. *WT* retina extracts showed a ~37kD band (Fig 2.2H, Lane 1). In contrast, a ~27kD dublet CRX band was detected in *E168d2/d2* (Lane 2) and homozygous *E168d2neo* ("*E168d2neo/d2neo"*) (Lane 3) retinas, suggesting that the $CRX^{[E168d2]}$ protein was a truncated CRX protein as predicted by Sanger sequencing and genomic alignment (Fig 2.1B). Furthermore, the band intensities suggest that the amount of $CRX^{[E168d2]}$ protein in mutant retinas is higher than that of the full-length CRX in *WT* retinas (Fig 2.2H, Lanes 2&3 vs. Lane 1). Quantification of CRX protein levels (Fig 2.2I) revealed a significant genotype difference ($p=0.0002$) overall. *E168d2/d2* retinas made twice as much total CRX protein as *WT* retinas, while *E168d2neo/d2neo* retinas produce similar amounts of CRX protein as *WT* retinas.

Heterozygous *E168d2/+* (Fig 2.2H, Lane 4) and *E168d2neo/+* (Lane 5) mice expressed both full-length WT CRX and truncated $CRX^{[E168d2]}$ protein but in different ratios. Quantification of CRX protein in *E168d2/+* retinal extracts (Fig 2.2I) revealed that the full-length WT CRX

protein was present at approximately half of the level in *WT* retinas, but the level of CRX$^{[E168d2]}$ protein was more than twice that of the WT CRX. As a result, the total CRX protein level in these retinas was significantly increased by 2-fold compared to normal retinas. *E168d2neo/+* retinal extracts also expressed WT CRX at approximately half *WT* levels but expressed less CRX$^{[E168d2]}$ protein than *E168d2/+* retinas (Fig 2.2H, lane 5 vs. 1&4, and Fig 2.2I). As a result, the total CRX level in *E168d2neo/+* was comparable to the *WT* control levels. These results are consistent with immunostaining results shown in Fig 2.2B-D and suggest that the *E168d2* allele overproduces mutant protein, which was prevented by the presence of the *neo* cassette in *E168d2neo*.

CRX expression patterns in *R90W* mice differed from *E168d2*. In P10 *R90W/W* retinal extracts (Fig 2.2H, Lane 6, & Fig 2.2I), CRX$^{[R90W]}$ was not significantly different from CRX in *WT* retinal extracts (Fig 2.2H, Lane 1, & Fig 2.2I), while levels were reduced in *R90Wneo/Wneo* retinas (Fig 2.2H, Lane 7 & Fig 2.2I). *R90W/+* retinas (Fig 2.2H, Lane 8, & Fig 2.2I) had normal total CRX protein levels compared to *WT* mice, although it was not possible to distinguish the quantity of WT CRX vs. CRX$^{[R90W]}$. As seen with the *E168d2* allele, the presence of the *neo* cassette reduced total CRX protein levels in *R90Wneo/Wneo* and *R90Wneo/+* retinas, compared to corresponding *R90W* retinas (Fig 2.2H, Lane 7 vs. 6, Lane 9 vs. 8, & Fig 2.2I). Thus, the presence of the *neo* cassette similarly affected the expression of both *K-IN* alleles.

2.1.ii) Mutant *Crx* mRNA is overexpressed in *E168d2* but not *R90W* mice

To investigate whether the changes observed in CRX protein levels correlate with altered *Crx* mRNA transcription, *Crx* mRNA levels were determined by quantitative real-time reverse transcriptase PCR (qRT-PCR) (Fig 2.2J). Specific PCR primer pairs were used that selectively amplified sequences from either *WT* or total (*WT*+*mutant*) *Crx* cDNA (Primer sets: *Crx E168WT* F/R and *Crx R90WT* F/R; Table 2.1). Primer specificity was validated by

amplification of *WT, E168d2/d2* and *R90W/W* retinal cDNA preparations. The results show that *E168d2/d2* retinas made twice as much total *Crx* mRNA as *WT* retinas, consistent with the elevated CRX protein levels in *E168d2/d2*. Total *Crx* mRNA levels in *E168d2neo/d2neo* retinas were lower than *E168d2/d2* levels (FDR p=0.07) but remained elevated relative to the *WT* ($p<0.05$) retinas, in contrast to the normal total CRX protein levels observed in these retinas.

E168d2/+ mice also showed moderately elevated total *Crx* mRNA levels (Fig 2.2J). Similar to protein levels, *E168d2* mRNA levels (deduced from Total - WT) were much higher than WT levels (~2:1 ratio). By comparison, *E168d2neo/+* mice expressed slightly elevated levels of total *Crx* mRNA that were lower than *E168d2/+*. *WT* and *E168d2* alleles were evenly expressed in these retinas. These results are consistent with the differences in CRX protein levels, supporting an RNA-based mechanism for $CRX^{[E168d2]}$ overexpression, which was partially reversed in *E168d2neo/+* mice.

R90W mice showed a distinct pattern of mRNA expression compared to *E168d2*. *R90W/W* retinas had normal *Crx* mRNA levels (Fig 2.2I), in contrast to their reduced CRX protein levels. This suggests a post-transcriptional mechanism either in the production or degradation of $CRX^{[R90W]}$ protein is likely responsible. *Crx* mRNA levels in *R90Wneo/R90Wneo* mice were substantially reduced in comparison to *WT* ($p<0.05$) and *R90W/R90W* mice (FDR p=0.07). The *R90W/+* and *R90Wneo/+* mice showed essentially normal levels of total *Crx* mRNA, contributed either by both alleles equally (in *R90W/+*) or the *WT* allele predominantly (in *R90Wneo/+*). Together, our results suggest that *E168d2* and *R90W* mRNA and corresponding proteins are produced in *K-IN* mouse retinas, but expression levels are differentially regulated. The mechanism of differential expression appears to be determined by features intrinsic to each mutant allele.

Chapter II

2.2. Retinal morphology

2.2.i) Morphology of homozygous *Knock-IN* mice

To determine the effect of *E168d2* and *R90W* mutations on retinal morphology, paraffin embedded retinal sections from *E168d2/d2* and *R90W/W* mice at P14, 1 month (mo) and 3mo were stained with hematoxylin and eosin (H&E), imaged by light microscopy and compared to sections from *WT* and *-/-* mice[6,7] (Fig 2.3). Cell specification in *WT* retina is complete by P14 and three distinct neuronal layers are present: the ONL, INL and the ganglion cell layer (GCL) (Fig 2.3A). At P14 *E168d2/d2, R90W/W* and *-/-* retinas all had established normal cellular lamination (Fig 2.3B-D). Quantitative morphometric measures across the sagittal plane of the retina presented by 'spider graphs' (Fig 2.3M) did not show a genotype*distance interaction (the statistical threshold required to make individual comparisons when analyzing data with two-way ANOVA) ($p=0.15$) at P14. These results support previous finding that CRX is not required for retinal cell fate specification[6], including rod photoreceptors, which constitute the majority of cells in the ONL. However, unlike *WT* retinas none of the mutant ONL cells had begun to form OS's at this age (Fig 2.3B, C, D vs. A). This OS defect persisted through 1-3mo when OS's were fully formed in *WT* retina (Fig 2.3F, G, H vs. E; J, K, L vs. I). By 1 mo, loss of ONL nuclei was evident in all mutant retinas (Fig 2.3F-H). In comparison to the ~12 rows of ONL nuclei seen in *WT* retinas, *E168d2/d2* had only ~3-4 rows, and *R90W/W* and *-/-* had ~7-9 rows (Fig 2.3F, G, H vs. E). Quantification of ONL thickness shows photoreceptor degeneration occurred evenly across the sagittal plane of all mutant retinas (Fig 2.3N, red, green & blue lines vs. black). While *R90W/W* and *-/-* mice had similarly reduced ONL thickness (green and blue line, respectively), *E168d2/d2 retinas* showed greater ONL thinning at 1mo (red line vs. green & blue), suggesting that degeneration was accelerated in these retinas. At 3mo, all models exhibited greatly reduced ONL thickness (Fig 2.3O) with only ~2-3 rows of ONL cells remaining (Fig 2.3J, K, L vs. I), suggesting ONL degeneration is progressive and extensive in all homozygous mutant mice.

To determine if ONL thinning is mediated by programmed cell death, "terminal deoxynucleotidyl transferase dUTP nick end labeling" (TUNEL) analysis was performed on P21 and P35 sagittal retinal sections (Fig 2.4). At P21 (Fig 2.4A-E), *E168d2/d2, R90W/W* and *-/-* mice all had significantly increased TUNEL+ cells present, almost exclusively in the ONL, *E168d2/d2* exhibited the highest number of TUNEL+ cells (~34 fold over *WT*). At P35 (Fig 2.4F-J), TUNEL+ cells remained elevated in the ONL of all mutant models but *E168d2/d2* mice showed fewer TUNEL+ cells compared to *R90W/W* and *-/-* mice. There was no increase in TUNEL+ cells in other retinal layers of any of the mutant mice. These timecourse analyses suggest that the peak of ONL degeneration is earlier in *E168d2/d2* mice compared to *R90W/W* and *-/-* mice, corresponding with the earlier ONL thinning observed in morphometric analyses.

In spite of reduced *Crx* expression levels, homozygous mice from the sublines of each strain that carry a *neo* cassette (*E168d2neo/d2neo*, *R90Wneo/Wneo*) displayed retinal morphology and function (data not shown) that was indistinguishable from the respective *neo*-deleted line. Thus, in homozygous mice lacking *WT* alleles, the onset and rate of photoreceptor degeneration was not greatly affected by mutant protein expression level.

2.2.ii) Rod morphology and survival in heterozygous *Knock-IN* mice

To determine the inheritance of *E168d2* and *R90W*-associated phenotypes, retinal morphology of heterozygous *E168d2/+, E168d2neo/+* and *R90W/+* mice was assessed by histology and morphometry. Paraffin embedded sagittal retina sections of heterozygous mutant mice at P14, 1mo, 3mo and 6mo were stained with H&E, imaged by light microscopy and compared to *WT* sections (Fig 2.5A-P). At P14, all retinas of heterozygous mutant mice displayed normal cellular lamination (Fig 2.5B-D vs. A). However, morphometric measurements of the ONL thickness showed that *E168d2/+* had increased thickness at the two points most proximal to the optic nerve head (ON) (Fig 2.5Q, colored lines vs. black). *E168d2/+* retinas also

showed shortened rod OS's compared to *WT* (Fig 2.5B vs. A). The OS defect in *E168d2/+* retinas remained at 1mo (Fig 2.5F vs. E), 3mo (Fig 2.5J vs. I) and 6mo (Fig 2.5N vs. M). At 1mo and 3mo (Fig 2.5E-L, R-S), morphometric measurements of ONL thickness did not identify a significant genotype*distance interaction overall, therefore differences at each distance were not tested. However, at 3mo, *E168d2*/+ had fewer rows of ONL cells ~6-8 and had reduced mean ONL thickness at each distance. By 6mo, most of *E168d2/+* ONL cells had degenerated with only ~2-3 rows of nuclei remaining (Fig 2.5N vs. M; Fig 2.5T, red vs. black line). By morphometric analyses, *E168d2/+* exhibited reduced ONL thickness at all distances. These results suggest that *E168d2/+* retinas undergo progressive rod photoreceptor degeneration through 6mo of age. Consistent with this observation, TUNEL analysis showed at P35 *E168d2*/+ mice had 15-fold more TUNEL+ cells than *WT* all of which were located in the ONL (Fig 2.4L vs. K; Fig 2.4O), consistent with the observed photoreceptor degeneration phenotype. These results suggest that the *E168d2* mutation causes dominant rod photoreceptor morphological defects and degeneration.

To determine if mice expressing lower levels of $CRX^{[E168d2]}$ protein have a less severe retinal phenotype, the morphology of *E168d2neo*/+ retinas was compared with that of *E168d2*/+ retinas. At P14, similar to *E168d2*/+ (Fig 2.5B), the OS's of *E168d2neo/+* mice appeared shorter than in *WT* mice (Fig 2.5C vs. A). However, unlike *E168d2/+*, *E168d2neo/+* formed fully elongated outer segments by 1mo (Fig 2.5G vs. F), which were well maintained at 3mo (Fig 2.5K vs. J) and 6mo (Fig 2.5O vs. M). These results suggest that, despite a delay in maturation, *E168d2neo/+* mice had less disrupted rod photoreceptor structure than *E168d2/+*. Furthermore, *E168d2neo/+* did not show significant thinning of the ONL through 6mo (Fig 2.5S&T, blue vs. black line) or elevated TUNEL+ cells compared to *WT* (Fig 2.4 M vs. K). Overall, the rod photoreceptor phenotype of *E168d2neo/+* mice is mild compared to *E168d2*/+ mice, suggesting that *E168d2* disease severity was influenced by the expression level of the mutant allele in heterozygous mice, consistent with *E168d2* being an antimorphic mutation.

Chapter II

To further reveal morphological defects in *E168d2* photoreceptors at the ultra-structural level, transmission electron microscopy (TEM) imaging analyses were performed on the retinas of P21 *E168d2/+, E168d2neo/+* and *WT* mice (Fig 2.5U-W). Images were randomly coded for blinded data analysis. Compared to the morphology of *WT* OS's (Fig 2.5U), *E168d2/+* mice (Fig 2.5V) exhibited severely shortened and disordered OS's including the presence of 'wave-like' disc patterns (white '*'s), ectopic vesicle formation (white '+'s), and improper stacking of OS discs including vertically oriented discs (white triangles). OS morphology was largely normal in *E168d2neo/+* mice (Fig 2.5W); although minor 'wave-like' disc patterns and ectopic vesicle formation were occasionally seen.

Rod nuclei in P21 *WT* retina adopt a characteristic nuclear architecture with large areas of highly electron dense heterochromatin in the center and smaller regions of translucent euchromatin in the nuclear periphery[8] (Fig 2.6A&D). The chromatin pattern of *E168d2/+* rods, however, appeared less condensed than *WT* (Fig 2.6B&E vs. A&D). This did not occur in *E168d2neo/+* mice (Fig 2.6C&F vs. A&D). To quantify these changes, the percentage of the nuclear area comprised of condensed heterochromatin was measured in randomly selected *WT*, *E168d2/+* and *E168d2neo/+* rod nuclei. Fig 2.6G shows that the mean area of heterochromatin in *E168d2/+* rods was significantly reduced by 8% compared to *WT*. This reduction in rod heterochromatin territory was not seen in *E168d2neo/+* mice, suggesting more normal rod nuclear architecture. In addition, photoreceptor degeneration in *E168d2*/+ and *E168d2neo/+* mice was evidenced by the presence of highly electron dense nuclei corresponding to pyknotic photoreceptor cells undergoing cell death, which were not observed in *WT* retinas (Fig 2.6E&F vs. G, white pentagon).

Unlike *E168d2/+*, *R90W/+* mice had normal retinal morphology at all ages (Fig 2.5D, H, L&P), comparable to +/- mice[6]. They formed and maintained full-length OS's and normal ONL thickness (Fig 2.5H, L&P) through 6mo of age. No increase in TUNEL+ cells over *WT* was

detected (Fig 2.4N&O). These results suggest rod photoreceptor development and maintenance are normal in *R90W/+* mice. This is consistent with clinical evaluations for heterozygous *R90W* carriers in human cases[9–13].

2.2.iii) Cone morphology and survival in heterozygous *Knock-IN* mice

2.2.iii.a) Mislocalization of cone nuclei in heterozygous E168d2 mice

Cone photoreceptors comprise only ~3% of ONL cells in mouse retina and their integrity could not be accurately assessed by light microscopy-based histology alone. However, cone nuclei were identified in TEM micrographs by their distinct decondensed chromatin patterns[8] and their nuclear position near the outer edge of the ONL (Fig 2.6A, white arrows). In the retinas of P21 *E168d2*/+ mice, few cone nuclei were identifiable in the ONL (Fig 2.6B&E). The majority of nuclei with 'cone-like' decondensed chromatin were misplaced to the inner regions of the ONL adjacent to the OPL (Fig 2.6E, white arrows).

The number of identifiable cone nuclei in *E168d2neo*/+ mice was greatly increased compared to *E168d2*/+, but nuclei were frequently mislocalized to the middle and inner ONL (Fig 2.6F, white arrows). Thus, cone formation/survival is improved in *E168d2neo*/+ mice but cone nuclear localization remains abnormal. Taken together, the ultra-structural analyses suggest that rod and cone photoreceptor morphology is highly disrupted in *E168d2/+* mice, and less so in *E168d2neo*/+ mice.

To determine whether the scattered nuclei with decondensed 'cone-like' chromatin in *E168d2/+* and *E168d2neo/+* were indicative of mislocalized cone nuclei, cone specific markers were used to further assess the cell population. Paraffin-embedded retinal sections were immunostained for cone arrestin (CARR, Accession: Q9EQP6.1) (antibody: rabbit polyclonal α-mCARR, Millipore), which stained the cone cell body from the inner segment to the synaptic

terminal (Fig 2.7A-D). Normal cones undergo nuclear migration during development, reaching their final position at the apical ONL by P12[14,15]. Retinal sagittal sections immunostained with CARR were analyzed to determine cone nuclear position in *WT* and mutant retinas (Fig 2.7A-D). Nuclei were assigned to three zones: Inner (IONL), Mid (MONL) or Outer ONL (OONL) (Fig 2.7A). At P14, while most *WT* cone nuclei were positioned in the OONL, cone nuclei in *E168d2/+* were mostly (>70%) positioned in the IONL and the majority of *E168d2neo*/+ cone nuclei (~70%) were mislocalized in the MONL (Fig 2.7E). At 1mo, *E168d2*/+ cone nuclei remained highly scattered (Fig 2.7B, white arrow) with less than 20% localized to OONL (Fig 2.7F), while most *E168d2neo*/+ cone nuclei (~80%) had migrated to the OONL although a significant number (11%) remained in the MONL (Fig 2.7C white arrows; Fig 2.7F). Thus, cone nuclear migration was largely ablated in *E168d2*/+ mice, while this phenotype was less severe in *E168d2neo*/+ mice. In contrast, cone nuclei localization in *R90W*/+ retina was mildly affected at P14 (~17% in MONL) (Fig 2.7E) but was normal at 1mo of age (Fig 2.7D&F).

2.2.iii.b) Progressive cone degeneration in heterozygous E168d2 mice

The numbers of CARR+ cones in P14 and 1mo *E168d2/+* retina sections were noticeably reduced compared to *WT* retina (Fig 2.7B). This could have been caused by either missing cone photoreceptors or aberrant CARR expression. Indeed, the expression of CARR was previously shown to be CRX-dependent[6] and was reduced in *E168d2/+* and *E168d2neo*/+ retinas (see below). To accurately determine the integrity of the cone population in heterozygous mutant retinas, another pan cone marker, peanut agglutinin conjugated to Rhodamine (PNA, Vector labs) was used in immunofluorescence staining of whole-mount retinas (Fig 2.8). Unlike CARR, PNA reactivity was independent of CRX's regulatory function and marked the membrane sheath of all cones[16], thus allowing for the accurate assessment of cone density in mutant retinas. Whole-mount retina preparations of 1mo and 1year (yr) old

heterozygous *K-IN* mice were stained with PNA (Fig 2.8E-L, blue stain). 40x fluorescent images were taken of the dorsal (D), ventral (V), nasal/temporal (N/T) and central (C) retina (diagrammed in Fig 2.8A), and cone density from each region was determined by counting PNA+ cells. At 1 mo, total cone density from *E168d2*/+ retinas over all regions was reduced by 67.7±1.3% (Fig 2.8B&C, green vs. blue bars), suggesting a cone deficit prior to rod degeneration. Cone density in 1yr old *E168d2/+* retinas was not determined because ONL degeneration was already extensive by 6mo (Fig 2.5N). Cone density was preserved in *E168d2neo*/+ mice at 1mo but was reduced by 39.6±5.3% at 1yr (Fig 2.8B, red vs. blue bar in each age group). Further comparing the cone density in different regions of *E168d2neo*/+ retina showed that cone density was normal in all regions at 1mo (Fig 2.8C, red vs. blue bars) and in the ventral retina at 1yr of age, but was reduced in all other regions (Fig 2.8D, red vs. blue bars). These results suggest that *E168d2*/+ mice had early cone deficits, while cones were maintained longer in *E168d2neo*/+ retinas. In contrast, *R90W*/+ mice had normal overall cone density through 1yr (Fig 2.8B&C, purple vs. blue bars), despite modestly reduced cone density in the central region with age.

2.2.iiic) Malformation of M/S cone opsin gradient in heterozygous E168d2 mice

Mouse cones consist of three subtypes defined by which cone opsins they express: OPN1MW (MOP, Accession: NP_032132.1), OPN1SW (SOP, Accession: NP_031564.1) or both opsins. In normal mouse retina, MOP and SOP are expressed in opposing gradients along the dorsal-ventral axis[17]. In the dorsal retina, a high percentage of cones express MOP, a few cones express SOP and no cones express both. Moving towards the central and ventral retina, there is an increase in SOP and MOP/SOP co-expressing cones[18]. The formation of the cone opsin gradient in *Crx* mutant retinas was assessed by IF staining of whole-mount retinas with polyclonal rabbit anti-red/green opsin (Millipore), polyclonal goat anti-OPN1SW (Santa Cruz)

antibodies and PNA. Fluorescence images acquired in the regions diagrammed in Fig 2.8A of control *WT* retinas showed the clear formation of the cone opsin gradient as expected (Fig 2.8E & I).

At 1mo, *E168d2/+* mice had low levels of the cone opsins in their outer segments and did not establish the M/S opsin gradient properly (Fig 2.8F&J). This conclusion was confirmed by quantification of the fraction of cones (PNA+) expressing MOP, SOP, both opsins or no opsin in tested regions (Fig 2.8M-P). *E168d2/+* dorsal retina showed a reduction in the proportion of cones expressing MOP only, but an increase in cones expressing SOP or both opsins (Fig 2.8 F&M, *E168d2/+* vs. *WT*). In contrast, *E168d2/+* ventral retina showed a large decrease in the percentage of MOP/SOP co-expressing cones and an increase in cones expressing SOP only (Fig 2.8J&P, *E168d2/+* vs. *WT*). Changes in M/S opsin patterns in central and nasal/temporal regions were also seen in *E168d2/+* mice (Fig 2.8N&O, *E168d2/+* vs. *WT*). Overall, *E168d2*/+ mice had a lower percentage of co-expressing cones and failed to properly regulate opsin expression across the dorsal-ventral axis. In addition, the levels of opsin on individual cone outer segments were highly variable in *E168d2/+* retinas, and some PNA+ cells did not have any detectable opsin (Fig 2.8F&J, white arrows). These results suggest that cone opsin expression, trafficking, or both were affected in *E168d2/+* retina.

In contrast, the levels of MOP and SOP were closer to normal in *E168d2neo*/+ cones but the opsin gradient remained highly disrupted (Fig 2.8G&K vs. E&I). As shown in the bar graphs, the percentage of cones co-expressing MOP/SOP was increased dramatically in *E168d2neo*/+ dorsal retina (Fig 2.8M, *E168d2neo/+* vs. *WT*), while the percentage of co-expressing cones was decreased in the central, nasal/temporal and ventral retina (Fig 2.8N-P, *E168d2neo/+* vs. *WT*). These results suggested that in *E168d2neo*/+ retinas, despite having normal cone numbers at 1mo, the cone opsin gradient was not properly established, which may have contributed to the deficits in cone function (see below) and long-term survival.

By comparison, *R90W/+* mice showed largely normal M/S opsin expression and gradient formation across the dorsal to ventral retina (Fig 2.8H&L vs. E&I). Quantification did not reveal any significant differences in the fraction of cones expressing each opsin in any of the regions surveyed (Fig 2.8M-P, *R90W/+* vs. *WT*).

Taken together, assessment of the cone photoreceptor population in mutant mice reveals that cones do not develop properly in *E168d2/+* retinas and cone defects arise earlier and are more severe than rod defects. *E168d2neo*/+ retinas showed more normal cone photoreceptor development and morphology and slower cone degeneration than *E168d2*/+ retinas. However, cone subtype specification remained disrupted in *E168d2neo*/+ retinas. Reduction in the number of cones in *E168d2*/+ and *E168d2neo*/+ before rod degeneration was consistent with a 'cone-centric' phenotype. In contrast, *R90W/+* mice had largely normal cone morphology, did not exhibit any significant cone subtype differences and no changes in overall cone density through 1yr.

2.3. Retinal physiology in *E168d2* and *R90W K-IN* mice

2.3.i) Homozygous *Crx E168d2* and *R90W* mice are functionally blind

To assess the consequence of these morphological changes on retinal function, electroretinograms (ERG) were performed under various light intensities on *WT*, *E168d2/d2* and *R90W/W* mice at 1 month of age[19]. *E168d2/d2* and *R90W/W* mice did not show any detectable dark-adapted or light-adapted responses (Fig 2.9 A-C). These results suggest *E168d2/d2* and *R90W/W* mice are blind at young ages, similar to the phenotype reported for *-/-* mice[6]. The functional deficits of rod and cone photoreceptors in *E168d2/d2* and *R90W/W* mice are consistent with the necessity of photoreceptor OS's for phototransduction[20,21] and suggest defective development of photoreceptor function in the homozygous mutant mice, similar to deficits in retinal function in LCA patients.

2.3.ii) Retinal function in heterozygous *Knock-IN* mice

2.3.i.a) Heterozygous E168d2 mice show severe rod/cone functional deficits

To determine if rod and cone photoreceptor morphological abnormalities and degeneration correspond with impaired retinal function, ERG's were performed on *E168d2/+*, *E168d2neo/+*, *R90W/+,* and *+/-* mice at 1mo, 3mo and 6mo (Fig 2.9D-L). First, ERG analyses were carried out on dark-adapted animals to assess rod-driven function. The responses to light flashes of increasing intensities were recorded, and the amplitudes of the A-waves (arising from the hyperpolarization of photoreceptors) and B-waves (arising from the activity of the photoreceptor-driven inner retina)[19] were measured. The results were plotted as average peak amplitudes of A and B-waves, against serial log scale light intensities (Fig 2.9D, E, G, H, J & K, black line). Next, ERGs were performed after 10 minutes of light adaptation to measure cone-driven responses. The average peak amplitudes of light-adapted B-waves were plotted against log scale light intensity (Fig 2.9F, I & L, black line). A significant genotype*light flash intensity interaction (by two-way ANOVA, $p<0.05$) was detected at every time point for both dark and light-adapted tests. At 1 mo, both dark-adapted A and B-waves were detectable in *E168d2/+* mice particularly in high light intensities, but the peak amplitudes were significantly reduced compared to *WT* controls (Fig 2.9D&G, green vs. black line), indicating impaired "rod-driven" function. *E168d2/+* rod function declined further with age, as the peak amplitudes became progressively smaller at 3 mo and 6 mo (Fig 2.9G, J vs. D; H, K vs. E, green line), corresponding with rod degeneration. For illustrative purposes, the progressive nature of rod functional deficits was demonstrated by the mean percent reductions of dark-adapted A and B-wave amplitudes (Table 2.2, *E168d2/+* columns). Percent reduction for both A and B-waves increased from 1mo to 6mo suggesting further deviation from *WT* function.

Cone-driven light-adapted B-wave peak amplitudes were barely detectable in *E168d2/+* at 1 mo (Fig 2.9F, green line) and all later ages tested (Fig 2.9I&L, green line), corresponding

with the early reduction of cone number. The mean percent reductions in light-adapted B-wave amplitudes were more severe than those seen in dark-adapted A or B-wave amplitudes (Table 2.2, *E168d2/+* columns), suggesting that cone function was more severely affected than rod function in *E168d2/+* mice.

Compared to *E168d2/+*, *E168d2neo*/+ mice show significantly less impaired dark-adapted A and B-wave peak amplitudes for most light intensities at all the ages tested (Fig 2.9D, E, G, H, K & L, red line vs. green line). *E168d2neo*/+ mice only had minor 'rod-driven' functional deficits compared to *WT* mice (red line vs. black line). These findings are summarized in Table 2.2. The average percent reductions of the dark-adapted A and B-waves in *E168d2neo*/+ mice were much less than *E168d2/+* for all three ages tested. More importantly, the minor deficits in *E168d2neo*/+ 'rod-driven' function did not progress with age, consistent with improved rod survival. Light-adapted B-waves were also significantly more robust in *E168d2neo*/+ mice, compared to *E168d2*/+ mice (Fig 2.9F, I & L, red vs. green line), but remained significantly reduced, compared to *WT* mice (red vs. black line). *E168d2neo*/+ cone deficits were more severe than rod deficits as shown by higher percent reductions in light-adapted B-waves than dark-adapted B-waves (Table 2.2, *E168d2neo*/+ columns). These defects were first detected at 1mo and persist through 6mo. Thus, while *E168d2*/+ mice had severely impaired rod and cone function resembling an 'LCA' phenotype, *E168d2neo*/+ mice had 'cone-centric' deficits in retinal function, modeling a 'CoRD' phenotype. The 'cone-centric' morphological and functional deficits of *E168d2neo*/+ mice, together with the early cone deficits in *E168d2*/+ mice, suggest that cones may be more sensitive than rods to the antimorphic effect of $CRX^{[E168d2]}$ protein.

2.3.ii.b) Heterozygous R90W mice show minor late-onset cone functional deficits

Previous studies report subtle ERG deficits in +/- mice[6], but in our studies *R90W/+* and +/- mice did not show significant ERG deficits at 1mo or 3mo (Fig 2.9D-I, blue and orange line, respectively). At 6mo, *R90W*/+ mice exhibit minor light-adapted B-wave deficits at the 1.88, 2.39 and 2.82 cdS/m^2 flash intensities (Fig 2.9L, blue vs. black line), while +/- were functionally normal, suggesting late-stage cone defects in *R90W*/+ mice. The difference between our studies and previous studies on +/- could have been due to mouse strain background, since the original *Crx KO* characterization was performed on a mixed background of *129Sv* x *C57BL/6*[6]. All experiments in this paper were performed on a congenic *C57BL/6J* background. Nevertheless, the *R90W* mutation produced only a mild late-stage cone functional phenotype in heterozygous mice, while the *E168d2* mutation in heterozygous mice caused an early-onset severe impairment of rod and cone function that depended on the expression level of the *E168d2* allele relative to *WT*.

2.4. Molecular activity of CRX$^{[E168d2]}$ and CRX$^{[R90W]}$ proteins

To determine how mutant forms of CRX protein affect target gene transcription, we assessed their ability to bind to DNA and transactivate transcription. First, electrophoretic mobility shift assays (EMSA) were used to measure DNA binding activity of CRX WT, CRX$^{[E168d2]}$ and CRX$^{[R90W]}$ protein expressed in HEK293 cells on the rhodopsin promoter target site *BAT-1*[22] (Fig 2.10A). To compare relative binding affinity, the amount of CRX in each nuclear extract was quantified using Western blots and equalized between transfections (Fig 2.10B). EMSA was then performed on a 2-fold dilution series of nuclear extracts of each CRX protein. Following incubation with *BAT-1* probe, WT CRX extract produced a single species of specific band shift (marked as 'WT') with a concentration-dependent intensity. This shifted band

represented specific binding of the indicated CRX protein to *BAT-1* CRX sites, as it is absent in the lane receiving the GFP control extract and when the probe contains mutated CRX binding sites (*BAT-1 Mut AB*). CRX$^{[E168d2]}$ nuclear extract also produced a specific band shift (marked 'E168d2'), which migrated much faster than the full-length CRX band as expected for a truncated protein. The intensity of the E168d2 band was comparable to the WT full-length band at each corresponding concentration, suggesting that CRX$^{[E168d2]}$ binds target sites with similar efficiency as WT CRX, providing a basis for competition binding to common targets. In contrast, CRX$^{[R90W]}$ nuclear extract produced a faint band with the same mobility as WT (Fig 2.10A), but significantly reduced intensity (~69% lower than WT). Reduced but not abolished DNA binding activity was also reported for bacterially expressed CRX homeodomain peptides carrying the *R90W* mutation[23]. These results support the hypothesis that CRX$^{[E168d2]}$ protein maintains normal DNA binding ability, while CRX$^{[R90W]}$ protein has reduced DNA binding ability.

To determine if *in vitro* DNA binding activity of each mutant reflected ability to associate with target chromatin *in vivo*, the association of WT CRX, CRX$^{[E168d2]}$ and CRX$^{[R90W]}$ protein with target gene promoter regions was examined using chromatin immunoprecipitation (ChIP) assays. ChIP was performed on P10 mouse retinas of *WT, E168d2/d2, R90W/W* and *-/-* mice using the CRX 119b-1 antibody[5]. As expected, enrichment of CRX$^{[E168d2]}$ protein was detected on the promoter of genes expressed in rods (*Rho, Gnat1*), cones (*Arr3, Opn1mw, Opn1sw*) and both rods/cones (*Crx, Rbp3* (Accession: AJ294749.1)) (Fig 2.10C, red bars). Despite reduced DNA binding activity *in vitro*, CRX$^{[R90W]}$ protein was found on the promoter of all candidate genes tested (Fig 2.10C, green bars). The mechanism by which CRX$^{[R90W]}$, which has reduced DNA-binding ability, is recruited to target gene chromatin *in vivo* remains to be determined.

The ability of CRX$^{[E168d2]}$ and CRX$^{[R90W]}$ proteins to transactivate target promoters, either alone or in combination with WT CRX, was assessed by dual-luciferase reporter assays in transiently transfected HEK293 cells. Consistent with a previous report[23], WT CRX was able to

cooperate with NRL to activate a *Rhodopsin* promoter-driven luciferase reporter, *Br130* (Fig 2.10D). However, CRX$^{[E168d2]}$ failed to increase transactivation above NRL alone, suggesting that CRX$^{[E168d2]}$ was unable to form functional interactions with transcription co-activators despite its normal DNA binding ability. In contrast, CRX$^{[R90W]}$ weakly promoted NRL-mediated transactivation, consistent with CRX$^{[R90W]}$'s weak ability to bind target DNA (Fig 2.10A) and interact with NRL[24] *in vitro*. To test the effect of mutant protein on WT CRX function, *E168d2* and *R90W* expression vectors were each co-transfected at increasing concentrations with WT CRX. CRX$^{[E168d2]}$ protein significantly impaired WT CRX function when the ratio of *E168d2:WT* vector reached 2:1 or higher, suggesting CRX$^{[E168d2]}$ actively interfered with WT CRX via an antimorphic mechanism, consistent with the dose-dependent toxicity observed in *E168d2/+* and *E168d2neo/+* mice. In contrast, at the same *mutant:WT* vector ratios, CRX$^{[R90W]}$ protein did not disrupt WT protein function, consistent with the hypomorphic effect of *R90W* in mice.

The *Crx* promoter is another known CRX direct target. It contains two CRX consensus binding sites within a 500-bp upstream region that is required for CRX auto-activation[25]. However, unlike *Rhodopsin*, which is downregulated, *Crx* was overexpressed in *E168d2* mice (Fig 2.2). To determine if *Crx* overexpression resulted from the direct action of CRX$^{[E168d2]}$ protein on the *Crx* promoter, dual-luciferase reporter assays using the 0.5K *Crx* promoter were performed (Fig 2.10E). As expected, WT CRX protein transactivated this in a concentration-dependent manner (Fig 2.10E), while CRX$^{[E168d2]}$ and CRX$^{[R90W]}$ at the highest concentration did not transactivate. When both WT and mutant proteins were present, CRX$^{[E168d2]}$ interfered with the transactivation activity of WT CRX, even at a 1:2 mutant:WT vector ratio. CRX$^{[R90W]}$ protein also reduced WT CRX transactivation activity, though less strongly, at the 1:1 and 2:1 mutant:WT vector ratios. These results suggest that both CRX$^{[E168d2]}$ and CRX$^{[R90W]}$ proteins 1) are less effective than WT CRX at activating target promoters, and 2) interfere with WT CRX autoactivation.

Taken together, functional analyses of CRX$^{[E168d2]}$ and CRX$^{[R90W]}$ proteins revealed that they affected target gene transcription via distinct mechanisms. While CRX$^{[E168d2]}$ bind DNA equally well as WT CRX, it fails to activate transcription and interferes with WT CRX function, resulting in a dose-dependent antimorphic effect. In contrast, CRX$^{[R90W]}$ has reduced ability to bind target DNA, qualifying CRX$^{[R90W]}$ as a hypomorphic protein.

Discussion

E168d2 and *R90W* mouse lines accurately model the corresponding human diseases

E168d2 mice model dominant 'LCA' or severe early-onset 'CoRD'

While all homozygous *K-IN* mice assessed in this paper demonstrated 'LCA'-like phenotypes, only *E168d2/+* mice presented with dominantly inherited retinopathy characteristic of 'LCA' or severe early-onset 'CoRD'. Rods and cones of *E168d2/+* mice were strongly functionally impaired from 1mo, exhibited abnormal nuclear and OS morphology and degenerated rapidly within the first 6mo of life (Summarized in Table 2.3). Importantly, the cone deficits were more severe and occurred earlier than rod deficits. Cone nuclei were mislocalized to the inner ONL at P14 and 1mo (Fig 2.7E&F) and the number of cones was decreased (32.3% of WT) in *E168d2/+* mice at 1mo (Fig 2.8B). In addition, the cone opsin gradient[18] was highly disrupted in *E168d2/+* and *E168d2neo/+* mice (Fig 2.8M-P). Misregulation of this gradient could arise either from inability of mutant CRX proteins to properly interact with co-factors to cooperatively regulate opsin expression, or as a result of impaired cone subtype specification. While these data suggest terminal differentiation of cones in *E168d2/+* retina may have been compromised, it is unclear if cone deficits were due to impaired cell fate specification, survival, or both. The accurate quantification of cone number was not possible in *E168d2/+* retina at P14 or earlier due to reduced expression of cone markers including cone opsins. Future experiments tracing the cone lineage in developing *E168d2/+* retinas are needed to distinguish these possibilities.

In summary, the *E168d2/+* mouse phenotype closely matched the clinical features of patients diagnosed with LCA who carry the *E168d2* mutation. These patients showed severe vision loss detectable within the first few months of life, including markedly reduced ERG responses[28–30]. Several pieces of evidence suggest that the *E168d2/+* mouse also models human disease associated with other mutations within the class of frameshift truncation mutations. First, several other frameshift and deletion mutations in human *CRX* caused similar clinical phenotypes[11–13,29,31–41]. Second, *in vitro* functional analyses showed that these mutations resulted in defects in target gene transactivation similar to those we see with *E168d2*[23,42]. Third, the recently-identified feline model *Rdy*, which also carries a frameshift truncation mutation in *Crx*[43], has severely reduced visual function and progressive photoreceptor degeneration that closely matches the *E168d2/+* phenotype[21,44–46]. *Rdy* cats carry a spontaneous single base-pair deletion *n.546delC* producing a truncated CRX protein just 14 amino acids longer than the CRX$^{[E168d2]}$ protein[43]. Thus, a common pathogenic mechanism is likely responsible for these similar phenotypes in different mammalian species, for which the *E168d2* mouse serves as an appropriate small-animal model.

E168d2neo reveals that expression levels of mutant CRX correlate with disease severity

CRX-associated dominant diseases vary in age of onset and severity, even with similar mutations[11,12]. The factors responsible for these phenotype variations have not yet been identified, but comparing findings from *E168d2* and *E168d2neo* mice revealed one possible mechanism. The *E168d2neo* mouse, which had reduced expression of CRX$^{[E168d2]}$, showed a less severe phenotype than *E168d2*, resembling later-onset dominant 'CoRD'. Characterization of the low expression subline *E168d2neo/+* (which expressed 30% less mutant protein) in parallel with *E168d2/+* revealed that mutant allele expression level significantly impacted phenotype severity. In young *E168d2neo/+* mice, the rod phenotype was almost fully

rescued and the cone phenotype was significantly improved by all measures performed, including rod and cone morphology (Figs 2.5-8), function (Fig 2.9, Table 2.2), survival (Fig 2.4). While older *E168d2neo/+* mice did show impaired cone function and degeneration, disease progression was much slower compared to *E168d2/+*. Thus, while the *E168d2* mouse represented the most accurate disease model for the human CRX^{E168d2} phenotype, the *E168d2neo/+* mouse modeled less severe forms of 'CoRD'. The expression level-dependent phenotypes of the *E168d2* mouse lines have several implications: 1) These findings support an antimorphic activity for $CRX^{[E168d2]}$ protein; 2) In human patients carrying similar *CRX* mutations, features intrinsic to the mutation allele and/or genetic background may affect *CRX* expression, which could impact disease severity; 3) Consequently, therapy directed at shifting the ratio of WT to mutant CRX protein might be effective at improving vision in patients.

Overexpression of $CRX^{[E168d2]}$ protein in E168d2 mice is caused by unknown mechanism

E168d2 mice overexpressed both *Crx* mRNA and protein in an allele specific manner (Fig 2.2H-J), indicating *Crx* misregulation occurred at the RNA level, either in the synthesis or degradation of the mRNA transcript. Transient transfection assays (Fig 2.10E) showed that while WT CRX was able to transactivate its own promoter, $CRX^{[E168d2]}$ had lost transactivation activity and interfered with WT CRX autoregulation. Thus, overexpression of the *E168d2* allele *in vivo* was unlikely due to the direct action of $CRX^{[E168d2]}$ protein on the *Crx* promoter. Other possible mechanisms for *E168d2* allele-specific overexpression *in vivo* include suppression of a negative feedback regulation, changes in transcription efficiency of the *E168d2* allele, or stability of the *E168d2* transcript. Expression of a known regulator of *Crx* expression, *Otx2* (Accession: NM_144841.3), was altered in *E168d2* mice. *Otx2* is required for induction of *Crx* expression during development[2,47] but is normally turned off in differentiated photoreceptors when CRX expression reaches high levels. *Otx2* was upregulated at P21 in *E168d2*/+ retinas (see Tables 3.3 & 3.4 in Chapter III), suggesting that the feedback network was affected in the mutants. A

more comprehensive investigation of the network regulating *Crx's* transcription is required. Alternatively, since the level of RNA made by the mutant allele was much higher than that of the *WT* allele in *E168d2/+* retinas, it is plausible that changes in *Crx E168d2* mRNA stability may be involved. More importantly, since this mutant allele-specific overexpression was shared by anther frameshift mutation, *I138*^{fs48} in *Drosophila*[42,48], the underlying molecular mechanism could be conserved for this type of CRX mutation.

R90W mice model mild late-onset dominant 'CoRD'

While homozygous *R90W* mice displayed a 'LCA-like' phenotype, heterozygous *R90W/+* mice didn't exhibit changes in photoreceptor morphology or degeneration at the early ages tested (Table 2.3). However, minor changes in cone function were detectable at 6mo (Fig 2.9L), suggesting *R90W/+* has a mild dominant phenotype. The *R90W/+* phenotype closely resembled the clinical features of a pedigree where the equivalent human *R90W* mutation was identified[10]: A proband homozygous for *R90W* had almost complete loss of vision and was diagnosed with autosomal recessive LCA. Her parents, each of whom carried one *R90W* allele, had mild cone functional defects and reduced color discrimination ability by middle age (40's). It is unknown if the cone functional defects reported for the human carriers are related to misregulation of cone gene expression or cone degeneration. Several other substitution mutations were similarly associated with mild late-onset dominant disease in humans[9–13,37,42]. Overall, reduced numbers of rods or cones were not observed in *R90W/+* mice up to one year of age, but disease may appear at later ages. The mild dominant phenotype of *R90W/+*, not observed in *+/-* mice, as well as the *CRX* promoter-driven luciferase assay results (Fig 2.10E) suggest CRX$^{[R90W]}$ possesses some minor disruptive effects on WT CRX function. Overall, however, unlike *E168d2* and *E168d2neo*, there were no major phenotypic differences observed between *R90W* and *R90Wneo,* consistent with CRX$^{[R90W]}$ being predominantly a hypomorphic protein. It is unknown how genetic background or environmental interactions contribute to the

substitution mutation disease phenotype. The *R90W* mouse line provides a valid small animal model for investigating this subset of milder *CRX*-related diseases.

CRX$^{[E168d2]}$ and CRX$^{[R90W]}$ protein cause disease through distinct mechanisms

Several pieces of evidence support that CRX$^{[E168d2]}$ and CRX$^{[R90W]}$ protein cause disease via different mechanisms, as illustrated in Fig 2.11. CRX$^{[E168d2]}$ protein bound to DNA and interfered with the function of CRX WT, classifying it as an antimorphic protein with dominant-negative activity (Fig 2.11B). CRX$^{[E168d2]}$ bound target gene DNA *in vivo,* suggesting that the abnormal photoreceptor morphology and function could stem from the direct activity of CRX$^{[E168d2]}$ on target gene expression. The antimorphic effect of CRX$^{[E168d2]}$ is unlikely to involve interference with NRL function, since CRX$^{[E168d2]}$ did not interfere with NRL transactivation (Fig 2.10D) and a similar truncation mutation in bovine CRX C160 (1-160) maintained interaction with NRL[24]. The *E168d2* mouse model thus demonstrates the effects of an antimorphic truncated CRX protein associated with human disease.

The CRX$^{[R90W]}$ protein had reduced DNA binding and weakly promoted transcription *in vitro*, classifying CRX$^{[R90W]}$ as a hypomorphic protein (Fig 2.11C, F). Although binding of CRX$^{[R90W]}$ to the BAT-1 oligo *in vitro* was reduced (Fig 2.10A), CRX$^{[R90W]}$ associated with CRX target DNA *in vivo* (Fig 2.10C), suggesting co-factors may anchor CRX$^{[R90W]}$ to target DNA. CRX$^{[R90W]}$ weakly promoted NRL-mediated transactivation of the *Rho* promoter *in vitro* (Fig 2.10D), consistent with early findings that CRX$^{[R90W]}$ protein reduced the physical interaction with NRL[24]. Thus, even though CRX$^{[R90W]}$ was associated with target promoters *in vivo*, it may have lost specific interactions with co-factors, therefore reducing its function. In *Drosophila*, human *R90W* was able to partially rescue the *otd^{uvi}* phenotype, consistent with a hypomorphic mechanism[48]. Taken together, our results show that CRX$^{[R90W]}$ is a predominantly hypomorphic mutant CRX protein, representative of substitution mutations associated with mild forms of CRX disease.

Chapter II

Mechanistically distinct mutations underlie *CRX*-associated disease

The molecular functions of several CRX mutations associated with human retinopathy have been investigated *in vitro*[10,23,42] and *in vivo* in *Drosophila*[48]. Such studies indicate that mutant CRX proteins have distinct molecular functions, which could in part explain the variation in *CRX*-disease phenotypes. The distinct phenotypes of mice carrying *E168d2,* an antimorphic frameshift mutation, and *R90W,* a hypomorphic substitution mutation, further expand our understanding of the impact of mutation type on disease pathology and closely match the functions and associated phenotypes of other similar type mutations. This suggests that *E168d2* and *R90W K-IN* mice are representative animal models for two larger groups of disease causing mutations, increasing their utility as research tools for studying pathology and developing therapies. There are likely additional mechanisms of *CRX*-associated disease yet to be modeled *in vivo*, such as substitution mutations that do not affect DNA-binding but are nonetheless associated with dominant disease[10,23,42]. Collectively, these studies demonstrate the diversity of molecular defects mediating *CRX*-associated disease and highlight the value of having multiple small-animal models to understand them.

For detailed Materials and Methods see Appendix B

Chapter II

References for Chapter II

1. Hayashi, S., Lewis, P., Pevny, L. & McMahon, A. P. Efficient gene modulation in mouse epiblast using a Sox2Cre transgenic mouse strain. *Mech. Dev.* **119 Suppl 1,** S97–S101 (2002).

2. Nishida, A. *et al.* Otx2 homeobox gene controls retinal photoreceptor cell fate and pineal gland development. *Nat. Neurosci.* **6,** 1255–1263 (2003).

3. Peng, G. H., Ahmad, O., Ahmad, F., Liu, J. & Chen, S. The photoreceptor-specific nuclear receptor Nr2e3 interacts with Crx and exerts opposing effects on the transcription of rod versus cone genes. *Hum. Mol. Genet.* **14,** 747–764 (2005).

4. Hsiau, T. H. *et al.* The cis-regulatory logic of the mammalian photoreceptor transcriptional network. *PLoS One* **2e643,** (2007).

5. Peng, G. H. & Chen, S. Crx activates opsin transcription by recruiting HAT-containing co-activators and promoting histone acetylation. *Hum Mol Genet* **16,** 2433–2452 (2007).

6. Furukawa, T., Morrow, E. M., Li, T., Davis, F. C. & Cepko, C. L. Retinopathy and attenuated circadian entrainment in Crx-deficient mice. *Nat Genet* **23,** 466–470 (1999).

7. Morrow, E. M., Furukawa, T., Raviola, E. & Cepko, C. L. Synaptogenesis and outer segment formation are perturbed in the neural retina of Crx mutant mice. *BMC Neurosci* **6,** 5 (2005).

8. Carter-Dawson LD, L. M. Rods and cones in the mouse retina. II. Autoradiographic analysis of cell generation using tritiated thymidine. *J Comp Neurol. 1979 Nov 15;188(2)263-72.* **15,** 263–272 (1979).

9. Swain, P. K. *et al.* Mutations in the cone-rod homeobox gene are associated with the cone-rod dystrophy photoreceptor degeneration. *Neuron* **19,** 1329–36 (1997).

10. Swaroop, A. *et al.* Leber congenital amaurosis caused by a homozygous mutation (R90W) in the homeodomain of the retinal transcription factor CRX: direct evidence for the involvement of CRX in the development of photoreceptor function. *Hum Mol Genet* **8,** 299–305 (1999).

11. Rivolta, C., Berson, E. L. & Dryja, T. P. Dominant Leber congenital amaurosis, cone-rod degeneration, and retinitis pigmentosa caused by mutant versions of the transcription factor CRX. *Hum. Mutat.* **18,** 488–98 (2001).

12. Sohocki, M. M. *et al.* A range of clinical phenotypes associated with mutations in CRX, a photoreceptor transcription-factor gene. *Am J Hum Genet* **63,** 1307–1315 (1998).

13. Huang, L. *et al.* CRX variants in cone-rod dystrophy and mutation overview. *Biochem. Biophys. Res. Commun.* **426,** 498–503 (2012).

14. Chiquet, C. *et al.* Characterization of calbindin-positive cones in primates. *Neuroscience* **115,** 1323–33 (2002).

15. Rich, K. a, Zhan, Y. & Blanks, J. C. Migration and synaptogenesis of cone photoreceptors in the developing mouse retina. *J. Comp. Neurol.* **388,** 47–63 (1997).

16. Mieziewska, K. E., van Veen, T., Murray, J. M. & Aguirre, G. D. Rod and cone specific domains in the interphotoreceptor matrix. *J. Comp. Neurol.* **308,** 371–80 (1991).

17. Szél, a, Röhlich, P., Caffé, a R. & van Veen, T. Distribution of cone photoreceptors in the mammalian retina. *Microsc. Res. Tech.* **35,** 445–62 (1996).

18. Applebury, M. L. *et al.* The murine cone photoreceptor: a single cone type expresses both S and M opsins with retinal spatial patterning. *Neuron* **27,** 513–523 (2000).

19. Peachey, N. S. & Ball, S. L. Electrophysiological analysis of visual function in mutant mice. *Doc. Ophthalmol.* **107,** 13–36 (2003).

20. Hawkins, R. K., Jansen, H. G. & Sanyal, S. Development and degeneration of retina in rds mutant mice: photoreceptor abnormalities in the heterozygotes. *Exp. Eye Res.* **41,** 701–20 (1985).

21. Humphries MM, Rancourt D, Farrar J, Kenna P, Hazel M, Bush R, Seiving PA, Sheils DM, McNally N, Creighton P, Erven A, Boros A, Gulya K, Capecchi M, H. P. Retinopathy induced in mice by targeted disruption of the rhodopsin gene. *Nat. Genet.* 216–219 (1997).

22. Chen, S. *et al.* Crx, a novel Otx-like paired-homeodomain protein, binds to and transactivates photoreceptor cell-specific genes. *Neuron* **19,** 1017–30 (1997).

23. Chen, S. *et al.* Functional analysis of cone-rod homeobox (CRX) mutations associated with retinal dystrophy. *Hum Mol Genet* **11,** 873–884 (2002).

24. Mitton, K. P. *et al.* The leucine zipper of NRL interacts with the CRX homeodomain. A possible mechanism of transcriptional synergy in rhodopsin regulation. *J. Biol. Chem.* **275,** 29794–9 (2000).

25. Furukawa, A., Koike, C., Lippincott, P., Cepko, C. L. & Furukawa, T. The mouse Crx 5'-upstream transgene sequence directs cell-specific and developmentally regulated expression in retinal photoreceptor cells. *J. Neurosci.* **22,** 1640–7 (2002).

26. Roberts, M. R., Hendrickson, A., McGuire, C. R. & Reh, T. a. Retinoid X receptor (gamma) is necessary to establish the S-opsin gradient in cone photoreceptors of the developing mouse retina. *Invest. Ophthalmol. Vis. Sci.* **46,** 2897–904 (2005).

27. Roberts, M. R., Srinivas, M., Forrest, D., Morreale de Escobar, G. & Reh, T. a. Making the gradient: thyroid hormone regulates cone opsin expression in the developing mouse retina. *Proc. Natl. Acad. Sci. U. S. A.* **103,** 6218–23 (2006).

28. Jacobson, S. G. *et al.* Retinal degenerations with truncation mutations in the cone-rod homeobox (CRX) gene. *Invest Ophthalmol Vis Sci* **39,** 2417–2426 (1998).

29. Lotery, a J. *et al.* Mutation analysis of 3 genes in patients with Leber congenital amaurosis. *Arch. Ophthalmol.* **118,** 538–43 (2000).

30. Freund, C. *et al.* De novo mutations in the CRX homeobox gene associated with Leber congenital amaurosis. *Nat. Genet.* **18,** 311–312 (1998).

31. Hanein, S. *et al.* Leber congenital amaurosis: comprehensive survey of the genetic heterogeneity, refinement of the clinical definition, and genotype-phenotype correlations as a strategy for molecular diagnosis. *Hum. Mutat.* **23,** 306–17 (2004).

32. Dharmaraj, S. R. *et al.* Mutational analysis and clinical correlation in Leber congenital amaurosis. *Ophthalmic Genet.* **21,** 135–50 (2000).

33. Galvin, J. a, Fishman, G. a, Stone, E. M. & Koenekoop, R. K. Evaluation of genotype-phenotype associations in leber congenital amaurosis. *Retina* **25,** 919–29

34. Nakamura, M., Ito, S. & Miyake, Y. Gene in a Japanese Patient With. **24,** 465–467 (1998).

35. Zhang, Q. *et al.* Screening for CRX gene mutations in Chinese patients with Leber congenital amaurosis and mutational phenotype. *Ophthalmic Genet.* **22,** 89–96 (2001).

36. Wang, P., Guo, X. & Zhang, Q. Further evidence of autosomal-dominant Leber congenital amaurosis caused by heterozygous CRX mutation. *Graefes Arch. Clin. Exp. Ophthalmol.* **245,** 1401–2 (2007).

37. Paunescu, K., Preising, M. N., Janke, B., Wissinger, B. & Lorenz, B. Genotype-phenotype correlation in a German family with a novel complex CRX mutation extending the open reading frame. *Ophthalmology* **114,** 1348–1357.e1 (2007).

38. Tzekov, R. T., Sohocki, M. M., Daiger, S. P. & Birch, D. G. Visual phenotype in patients with Arg41Gln and ala196+1bp mutations in the CRX gene. *Ophthalmic Genet.* **21,** 89–99 (2000).

39. Walia, S. *et al.* Visual acuity in patients with Leber's congenital amaurosis and early childhood-onset retinitis pigmentosa. *Ophthalmology* **117,** 1190–8 (2010).

40. Den Hollander, A. I., Roepman, R., Koenekoop, R. K. & Cremers, F. P. M. Leber congenital amaurosis: genes, proteins and disease mechanisms. *Prog. Retin. Eye Res.* **27,** 391–419 (2008).

41. Freund, C. L. *et al.* Cone-rod dystrophy due to mutations in a novel photoreceptor-specific homeobox gene (CRX) essential for maintenance of the photoreceptor. *Cell* **91,** 543–553 (1997).

42. Nichols, L. L. *et al.* Two novel CRX mutant proteins causing autosomal dominant Leber congenital amaurosis interact differently with NRL. *Hum. Mutat.* **31,** E1472–83 (2010).

43. Menotti-Raymond M, Deckman KH, David VA, Myrkalo J, O'Brien SJ, N. K. Mutation discovered in a feline model of human congenital retinal blinding disease. *Invest Ophthalmol Vis Sci* **[Epub ahea,** (2010).

44. Leon, a & Curtis, R. Autosomal dominant rod-cone dysplasia in the Rdy cat. 1. Light and electron microscopic findings. *Exp. Eye Res.* **51,** 361–81 (1990).

45. Leon, A. & Curtis, R. Autosomal Qominant Dysplasia findings in the Rdy Cat 2 . Electrophysiological. 489–502 (1991).

46. Chong, N. H., Alexander, R. a, Barnett, K. C., Bird, a C. & Luthert, P. J. An immunohistochemical study of an autosomal dominant feline rod/cone dysplasia (Rdy cats). *Exp. Eye Res.* **68,** 51–7 (1999).

47. Omori, Y. *et al.* Analysis of transcriptional regulatory pathways of photoreceptor genes by expression profiling of the Otx2-deficient retina. *PLoS One* **6,** e19685 (2011).

48. Terrell, D. *et al.* OTX2 and CRX rescue overlapping and photoreceptor-specific functions in the Drosophila eye. *Dev. Dyn.* **241,** 215–28 (2012).

49. Wang, X. *et al.* Barrier to autointegration factor interacts with the cone-rod homeobox and represses its transactivation function. *J. Biol. Chem.* **277,** 43288–300 (2002).

50. Chen, S. *et al.* Interference of Crx-dependent transcription by ataxin-7 involves interaction between the glutamine regions and requires the ataxin-7 carboxy-terminal region for nuclear localization. *Hum. Mol. Genet.* **13,** 53–67 (2004).

Chapter II

Tables

Table 2.1 PCR Primer Pairs			
Mouse Crx Genotyping primers		**Mouse QRT-PCR primers**	
DN WT-F	5'- CATTTGGAGTCCAGCCTCAGAG -5'	Arr3-RTF1	5'-AAGTTTTCCATCTACCTGGGG-3'
DN mut-F	5'- CATTTGGAGTCCAGCCTCAGGC -3'	Arr3-RTR1	5'-TCACATCCAAGTCATCACGG-3'
DN-R	5'- GAGCAAGTTCTCAGCACCTTTACG -3'	Opn1sw-RTF1	5'-GCTGGACTTACGGCTTGTCACC-3'
Total Crx F:	5'-GCAGCGACAGCAGCAGAAACA-3'	Opn1sw-RTR1	5'-TGTGGCGTTGTGTTTGCTGC-3'
Total Crx R:	5'-AGAAGCCGGGGCATAGGTCAT-3'	Crxos1-RT F	5'-GGAACTCAAACTACGGAAAGACC-3'
Neo F:	5'-ATG GAT TGC ACG CAG GTT CTC-3'	Crxos-RT R	5'-CTTTGGTACCCAGAAGAGAGCTT-3'
Neo R:	5'-CTG ATG CTC TTC GTC CAG ATC-3'	Crx LF WT-RTF	5'-CCTCACTATTCAGTCAATGCCTTG-3'
LF WT-F	5'-CCAGGTCTGGTTCAAGAATCGT-3'	Crx LF WT-RTR	5'-TCTGCATTTCGCCCTACG-3'
LF mut-F	5'-CCAGGTCTGGTTCAAGAATTGG-3'	Crx DN WT RTF	5'-TGCCTGAGTCCAGGGTCCAG-3'
LF-R	5'-CAAACATCTGTAGAGGGTCTCGG-3'	Crx DN WT RTR	5'-CCTCAGGCAAAGGAGCCTCTG-3'
Genomic mCrx Int/Ex4-F	5'-GGTAGGTAGGTGATACATGATGAC-3'	Dnaic-RTF	5'-CTGTGGTAGCCAAGAAGAAGAAC-3'
Genomic mCrx Int/Ex4-R	5'-CCCACTGAAATAGGAACTTGGAG-3'	Dnaic-RTR	5'-CTCACGAGGTTTAGCAGTTTGTC-3'
Sequencing primer DN	5'-AACAGAAAGCAGAAGCCG-3'	Mop-RTF	5'-GGTGGTGATGGTCTTCGCATAC-3'
Sequencing primer LF	5'- GTGATGTGTGGGTCTTACC -3'	Mop-RTR	5'-TTGGAGGTGCTGGAAAGTTCAG-3'
		Myo7a-RTF	5'-GACACCTGACAGACTGGATAAAG-3'
Mouse promoter ChIP primers		Myo7a-RTR	5'-CTAGGGAAGTAGGATTTGTCCTC-3'
Arr3-376F	5'- CAACCCAGCACAGGATAATG -3'	Nr2e3-RTF	5'-AGTCCCAGGTGATGCTAAGC-3'
Arr3-181R	5'-TGATTGTTACTGAGGAGGTAGGC -3'	Nr2e3-RTR	5'-TTCTAAGATGTGCTGCCCC-3'
Crx-159F	5'- TCCCTCCCTTCTTCATCAAC -3	NRL-RTF	5'-TTCTGGTTCTGACAGTGACTACG-3'
Crx+73R	5'- GAAATAGGTCCCCTCACACG -3'	NRL-RTR	5'-AAGGCTCCCGCTTTATTTC-3'
Gnat1-304F	5'- CGGGACTAAAGGGTCTGTTC -3'	Otx2-RTF	5'-ACTTGCCAGAATCCAGGGTG-3'
Gnat1-185R	5'- TTCAACTGCTGACTTGGCAC -3'	Otx2-RTR	5'-TGAGCCAGCATAGCCTTGAC-3'
Grm6-139F	5'- CCAGAGGTTGGCTCAGGTAAG -3'	Rho-RTF	5'-GCTTCCCTACGCCAGTGTG-3'
GluR6+67R	5'- GCAGGAAAAGTTGGTGACTCG -3'	Rho-RTR	5'-CAGTGGATTCTTGCCGCAG-3'
IRBP-364F	5'- AACCAGACCTCCAACTGCG -3'	Tuba1b-RTF	5' -CAAGCTGGAGTTCTCCATTTAC-3'
IRBP+45R	5'- CTGCCTCTCTCCCTTGCCC -3'	Tuba1b-RT2R	5'-GTCATAGATGGCCTCATTGTCT-3'
OPN1SW-456F	5'- CACTCATCCTCTTCCTGTTTCC -3'	Ubb-RT1F	5'-CAACATCCAGAAAGAGTCAACC-3'
OPN1SW-262R	5'- GGTCAGTATTGGTTTCTGTGGC -3'	Ubb-RT1R	5'-ATGTTGTAATCAGAGAGGGTGC-3'
OPN1MW-216F	5'- TGAGCACCCCTGTGGATTG -3'		
OPN1MW-23R	5'- GGAACCTGTCAGACTTGGCAC -3'		
Rho-200F	5'- GGGGCAGACAAGATGAGACAC -3'		
Rho+124R	5'- TTCGTAGACAGAGACCAAGGC -3'		

Table 2.1) PCR Primer Pairs for Genotyping, qRT-PCR and qChIP. List of oligonucleotides used for all PCR-based analyses.

Table 2.2) Percent reduction* of ERG peak amplitudes in *E168d2/+* and *E168d2neo/+* mice

	Dark-adapted A-waves Average: -0.02, 0.387, 0.875 Cds/m^2 flashes		**Dark-adapted B-waves** Average: -0.02, 0.387, 0.875 Cds/m^2 flashes		**Light-adapted B-waves** Average: 0.40, 0.88, 1.38, 1.88, 2.39, 2.82 Cds/m^2 flashes	
Age	***E168d2/+***	***E168d2neo/+***	***E168d2/+***	***E168d2neo/+***	***E168d2/+***	***E168d2neo/+***
1mo	73.3 ±5.3	25.9 ±1.1	68.2 ±1.6	25.6 ±5.3	72.8 ±10.2	41.3 ±7.3
3mo	76.4 ±5.1	25.2 ±1.2	73.1 ± 2.8	26.3 ±1.8	82.4 ±4.3	46.7 ±6.3
6mo	82.6 ±8.7	21.8 ±4.5	76.3 ±0.3	17.3 ±1.9	78.9 ±12.9	41.4 ±5.3

*Average percent reductions were calculated based on Fig 7 data. ±STDEV

Table 2.3) Summary of retinal phenotypes of *Crx E168d2, R90W* and *KO* mice

	Function (ERG)		OS Length	Nuclear position	Opsin Gradient	Photoreceptor degeneration timecourse		Gene expression		Disease model
Genotype	**Rod**	**Cone**	**Rod**	**Cone**	**Cone**	**Rod**	**Cone**	**P10**	**P21**	
WT	++++	++++	++	OONL	+++	-	-	+++	+++	
E168d2/+	+	+	+	MONL	-	1-6mo	1mo	+	+	LCA
E168d2neo/+	+++	++	++	IONL	+	-	1mo-1yr	+	++	CoRD
R90W/+	++++	++++	++	OONL	++	-	-	++	+++	Mild CoRD
+/-	++++	++++	++	OONL	ND*	-	-	++	+++	
E168d2/d2	-	-	-	-	-	1-3mo	1-3mo	-	-	LCA
R90W/W	-	-	-	-	-	1-3mo	1-3mo	-	-	LCA
-/-	-	-	-	-	-	1-3mo	1-3mo	-	-	LCA

'+' qualitative graded levels; '-' null; *ND: Not determined

Fig. 2.1)

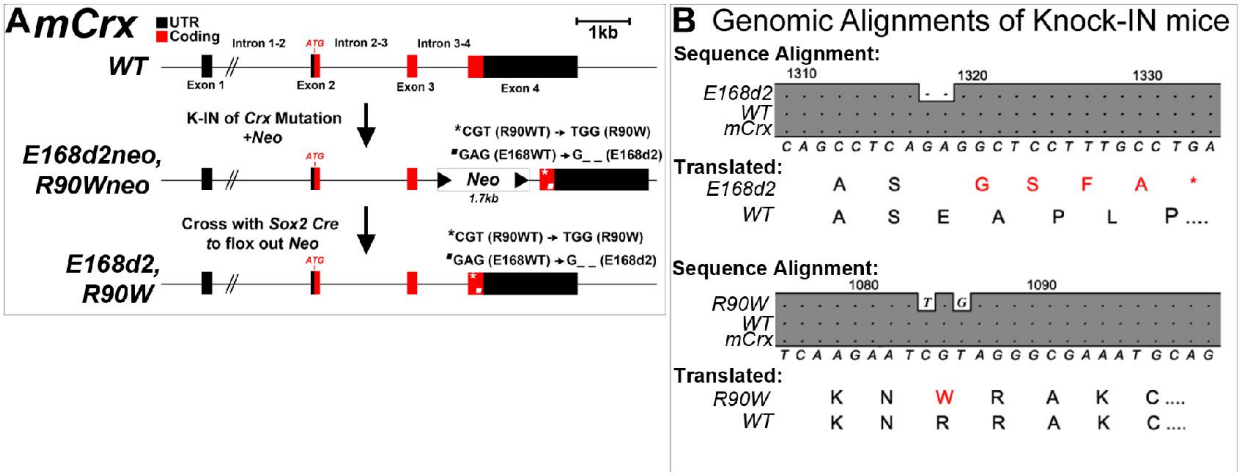
A mCrx
UTR
Coding
1kb
WT
Intron 1-2
Intron 2-3
Intron 3-4
Exon 1
Exon 2
Exon 3
Exon 4
ATG
K-IN of Crx Mutation
+Neo
E168d2neo,
R90Wneo
*CGT (R90WT) → TGG (R90W)
#GAG (E168WT) → G_ _ (E168d2)
Neo
1.7kb
Cross with Sox2 Cre
to flox out Neo
E168d2,
R90W
B Genomic Alignments of Knock-IN mice
Sequence Alignment:
1310
1320
1330
E168d2
WT
mCrx
C A G C C T C A G A G G C T C C T T T G C C T G A
Translated:
E168d2 A S G S F A *
WT A S E A P L P ....
Sequence Alignment:
1080
1090
R90W
WT
mCrx
T C A A G A A T C G T A G G G C G A A A T G C A G
Translated:
R90W K N W R A K C ....
WT K N R R A K C ....

Figure 2.1) Generation of mechanistically distinct *Knock-IN (K-IN*) mouse lines for *CRX*-associated disease: *E168d2*, *E168d2neo*, *R90W* and *R90Wneo*. A) Diagram of mouse *Crx* locus showing gene structure and strategy for generating *Crx E168d2* and *R90W K-IN* lines. *E168d2neo* and *R90Wneo* each carry the indicated targeting construct containing *loxP*-flanked *Neo* cassette in Intron 3-4 as a selection marker. The final *E168d2* and *R90W* lines were generated from the respective '*Neo*+' sublines by *Sox2-Cre*-mediated excision in germline. B) Germline transmission of *K-IN* constructs was confirmed by Sanger sequencing of genomic DNA from homozygous *E168d2/d2, R90W/W* and *WT* mice and aligned to genomic *mCrx*. Shaded '·' in the grey boxes indicate fully conserved sequences, unshaded '·' denote deletions, and letters indicate base pair substitutions. Gene position (above alignment), consensus sequence (below alignment) and translated amino acid sequence are shown. Amino acid changes in *E168d2* and *R90W* are shown in red text with '*' indicating the novel stop codon in *E168d2*. Further generations of *E168d2* and *R90W* mice were genotyped by allele specific PCR amplification of genomic DNA (Table 2.1).

Fig. 2.2)

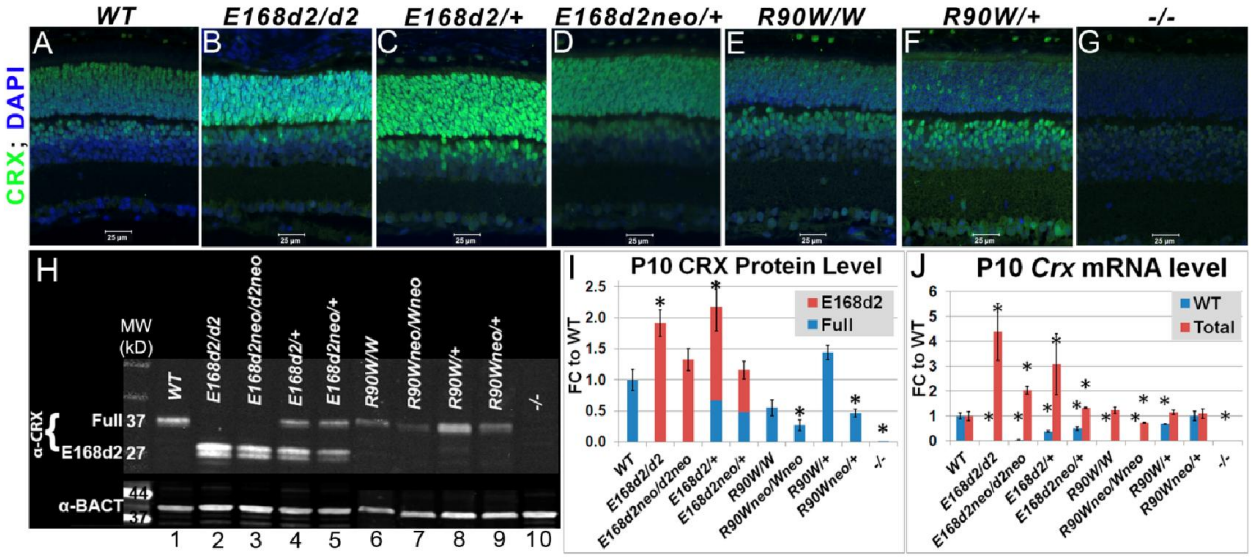
WT
E168d2/d2
E168d2/+
E168d2neo/+
R90W/W
R90W/+
-/-
A
B
C
D
E
F
G
CRX; DAPI
H
MW (kD)
WT
E168d2/d2
E168d2neo/d2neo
E168d2/+
E168d2neo/+
R90W/W
R90Wneo/Wneo
R90W/+
R90Wneo/+
-/-
α-CRX
Full 37
E168d2 27
α-BACT
1 2 3 4 5 6 7 8 9 10
I
P10 CRX Protein Level
E168d2
Full
FC to WT
J
P10 Crx mRNA level
WT
Total
FC to WT

Figure 2.2) Differential expression of mutant CRX protein/RNA in K-IN mouse retinas. A-G) Paraffin embedded sagittal sections of P10 mouse retinas were stained with the mouse monoclonal CRX M02 antibody (Abnova) and imaged by fluorescent microscopy. Scale bars: 25μM. H) SDS-PAGE and Western blot analyses of CRX proteins made by the indicated mouse strains at P10 using the rabbit polyclonal CRX 119b-1 antibody and mouse monoclonal anti-β-ACTIN (α-BACT, Sigma-Aldrich). Positive bands correlating with the ~37kD full-length CRX and ~27kD truncated $CRX^{[E168d2]}$ are visible. Lanes are numbered for reference (below). I) CRX protein levels were quantified by measuring the intensities of the $CRX^{[E168d2]}$ and full-length bands normalized to the β -ACTIN control using LI-COR Odyssey Image Studio software. The results are presented as fold changes (FC) relative to full-length CRX level in *WT* retina. (*p≤0.05) J) *Crx* mRNA levels were determined by quantitative real-time PCR using allele specific PCR primer pairs. Separate primer pairs were used to amplify *WT Crx* alone and total *Crx (WT+mutant)* in *E168d2* and *R90W* mice (see materials and methods). The results are presented as FC relative to *WT* retina. (*p≤0.05)

Fig. 2.3

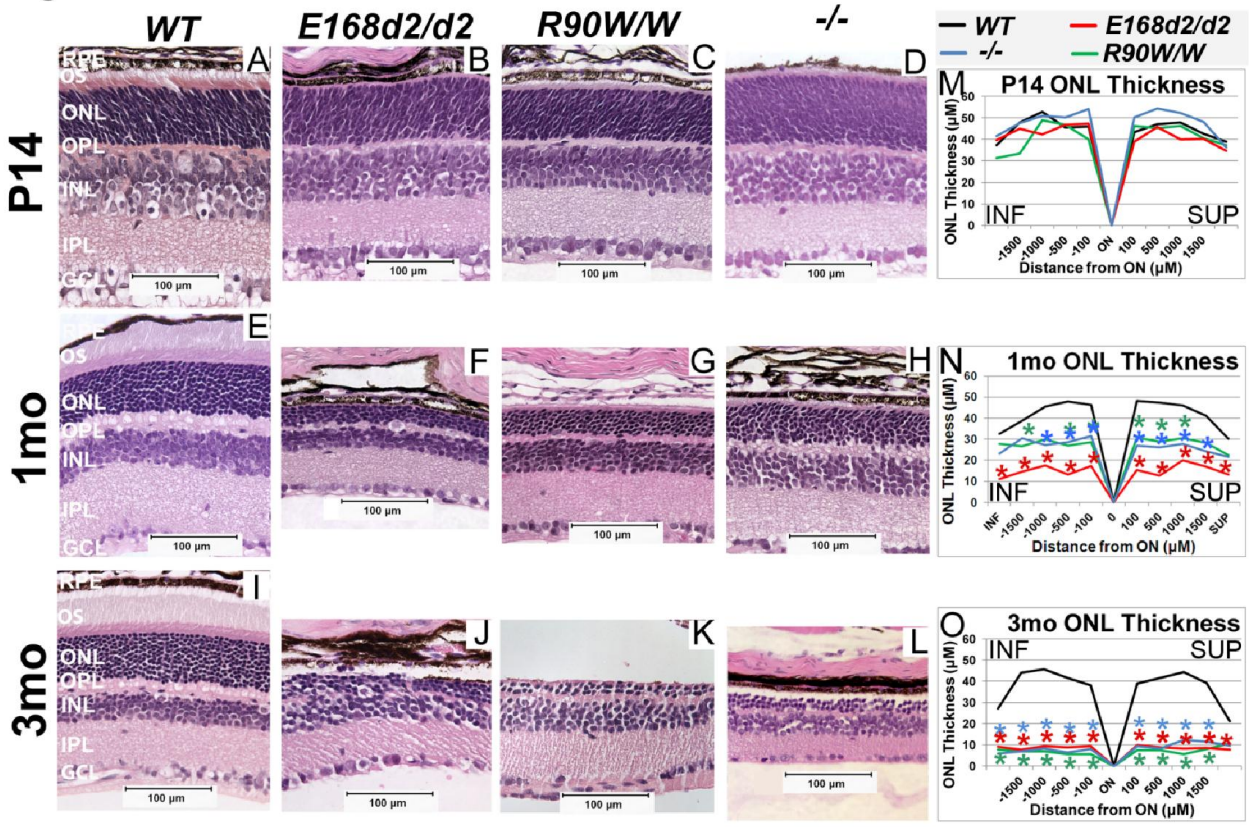
WT
E168d2/d2
R90W/W
-/-
P14
1mo
3mo
A
B
C
D
E
F
G
H
I
J
K
L
M
N
O
ONL
OPL
INL
IPL
GCL
100 µm
WT
E168d2/d2
-/-
R90W/W
P14 ONL Thickness
1mo ONL Thickness
3mo ONL Thickness
ONL Thickness (µM)
INF
SUP
Distance from ON (µM)

Figure 2.3) Homozygous E168d2/d2 and R90W/W mice develop 'LCA'-like retinopathy. A-L) H&E staining of paraffin embedded sagittal retinal sections for *E168d2/d2, R90W/W* and *-/-* mice at P14, 1mo and 3mo and imaged by light microscopy, showing the lack of photoreceptor outer segments (OS) and loss of ONL cells with age. Scale bars: 100μM. M-O) Reduction of ONL thickness in mutant retina at each age was quantified using 'spider graph' morphometry. Significant differences in overall ONL thickness were determined by testing genotype*distance interactions (by two-way ANOVA) at 1mo ($p=0.002$) and 3mo ($p=0.0001$), followed by individual comparisons to WT: *$p<0.05$. INF-inferior retina, SUP-superior retina.

Fig 2.4)

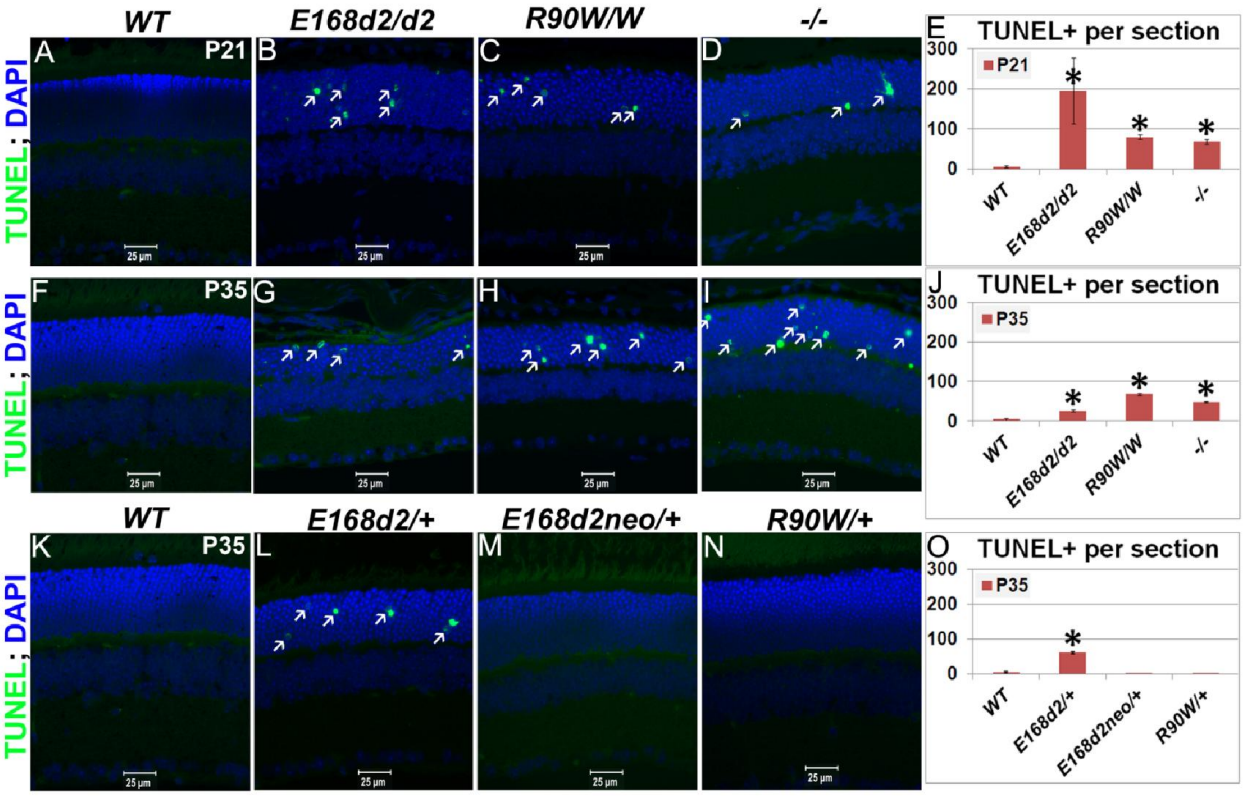
WT
E168d2/d2
R90W/W
-/-
A
P21
B
C
D
TUNEL; DAPI
E
TUNEL+ per section
P21
300
200
100
0
WT
E168d2/d2
R90W/W
-/-
F
P35
G
H
I
J
TUNEL+ per section
P35
WT
E168d2/+
E168d2neo/+
R90W/+
K
P35
L
M
N
O
TUNEL+ per section
P35
25 µm

Figure 2.4) Detection of programmed cell death in *E168d2, R90W* and *-/-* mice. **A-O**) Cells undergoing programmed cell death were detected by fluorescent TUNEL staining of paraffin embedded sagittal sections. *WT, E168d2/d2*, *R90W/W* and *-/-* retinas were assessed at P21 (**A-D**) and P35 (**F-I**). TUNEL+ cells (white arrows) in the ONL of *WT*, *E168d2/d2*, *R90W/W* and -/- retinas were quantified at P21 (**E**) and P35 (**J**). **K-N**) *WT*, *E168d2/+, E168d2neo/+*, and *R90W/+* retinas were assessed at P35. **O**) Quantification of TUNEL+ cells in P35 *WT*, *E168d2/+, E168d2neo/+*, and *R90W/+* retinas confirms increased programmed cell death in *E168d2/+* retinas. Scale bar: 25μM. (*$p<0.05$; Error bars: STDEV)

Fig 2.5)

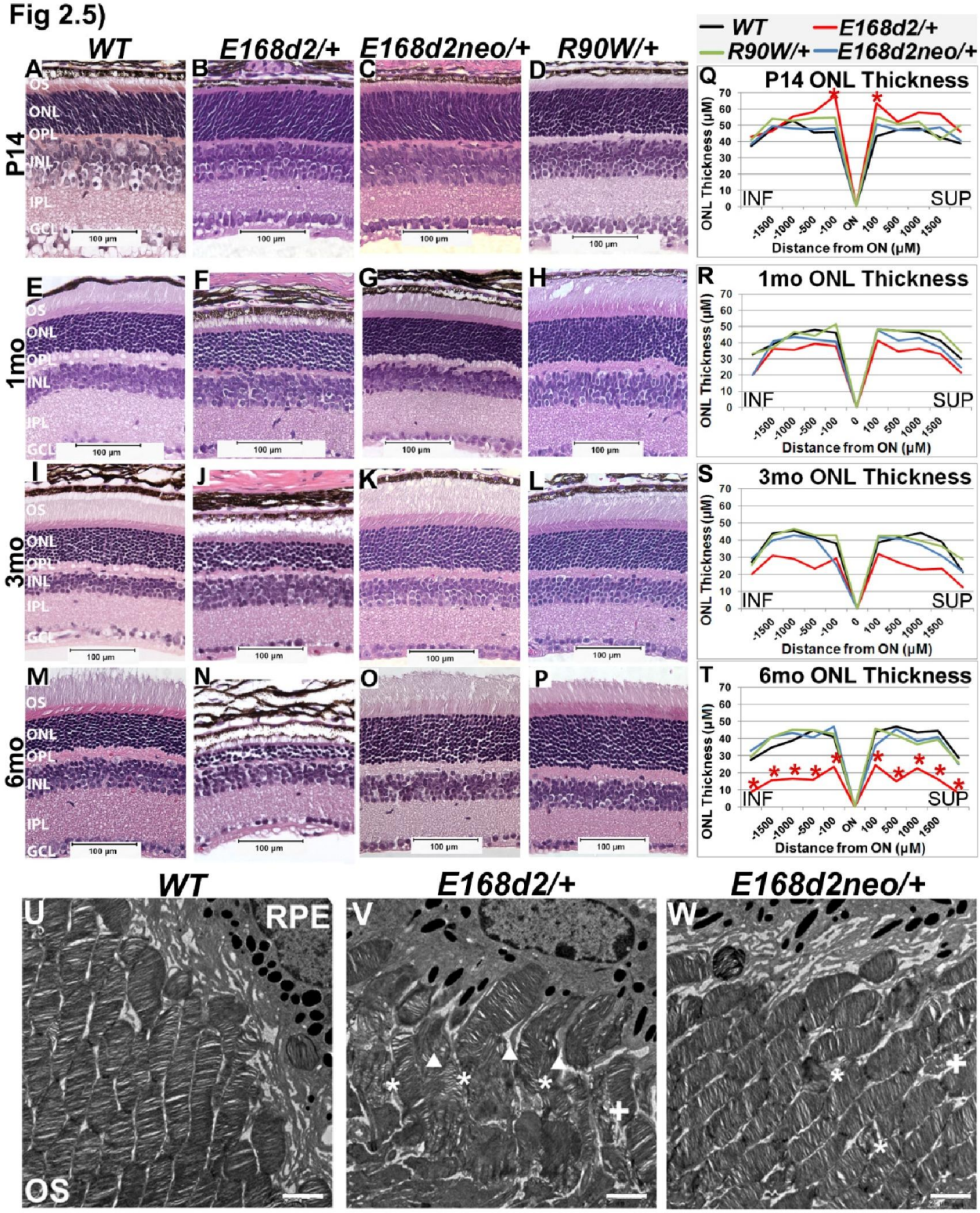
WT
E168d2/+
E168d2neo/+
R90W/+
P14
1mo
3mo
6mo
OS
ONL
OPL
INL
IPL
GCL
100 µm
WT
E168d2/+
R90W/+
E168d2neo/+
P14 ONL Thickness
1mo ONL Thickness
3mo ONL Thickness
6mo ONL Thickness
ONL Thickness (µM)
INF
SUP
Distance from ON (µM)
RPE
OS

Figure 2.5) Heterozygous *E168d2/+* mice, but not *R90W/+*, develop dominant retinopathy. **A-P**) Retinal morphology of the indicated heterozygous mutant mice was assessed by H&E staining of paraffin embedded sagittal sections at P14, 1mo, 3mo, and 6mo. Shortened photoreceptor outer segments and ONL cell loss are apparent in *E168d2/+* retina only. Scale bars: 100μM **Q-T**) ONL thickness was assessed by spider graph morphometry at the indicated ages. *E168d2/+* (red line) shows progressive thinning of the ONL through 6mo, while it's low expression subline, *E168d2neo/+* (blue line), and *R90W/+* (green line) do not. Significant differences in overall ONL thickness were determined by testing genotype*distance interactions (by two-way ANOVA). Significant interactions were observed at P14 ($p=0.03$) and 6mo ($p=0.03$), followed by testing individual comparisons to *WT:* *$p<0.05$. INF-inferior retina, SUP-superior retina. **U-W**) The ultra structure of rod outer segment (OS) and nuclear morphology was assessed by transmission electron microscopy. Micrographs of rod outer segments proximal to RPE from *WT* control (**U**), *E168d2/+* (**V**) and *E168d2neo/+* mice (**W**). *E168d2/+* OS's are highly disorganized showing 'wave-like' OS membrane stacks '*', vesiculated membranes '+' and vertically oriented OS membranes (triangles). *E168d2neo/+* OS's only show minor 'wave-like' patterns and vesiculated membranes.

Fig 2.6)

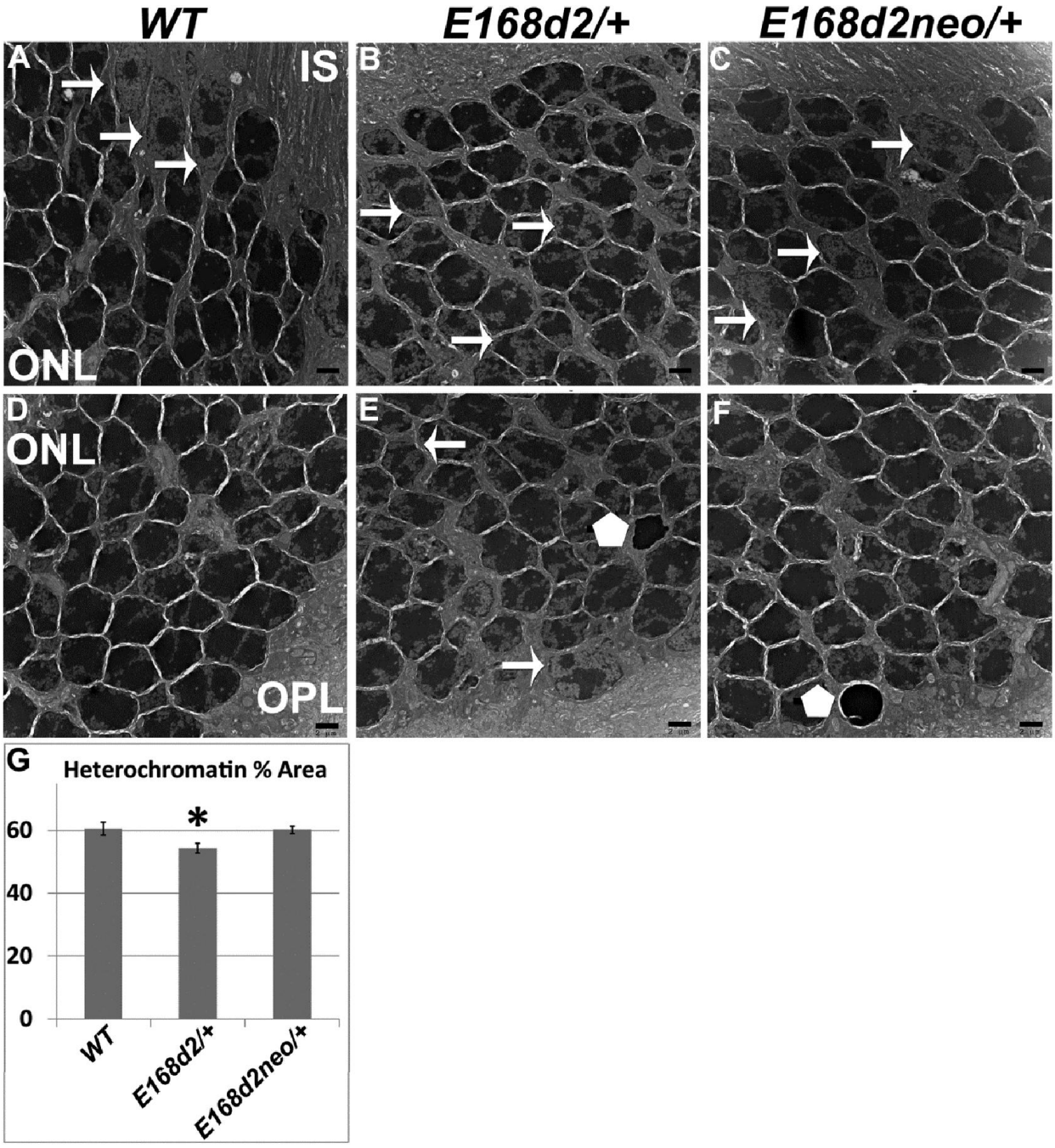
WT
E168d2/+
E168d2neo/+
A
IS
ONL
B
C
D
ONL
OPL
E
F
G
Heterochromatin % Area
*
60
40
20
0
WT
E168d2/+
E168d2neo/+

Figure 2.6) *E168d2/+* mice have disorganized nuclear architecture. **A-F**) Transmission electron micrographs of P21 WT, *E168d2/+* and *E168d2neo/+* retinas showing the ONL nuclei in the region proximal to inner segments (IS) (**A-C**) and OPL (**D-F**). White arrows indicate cone nuclei in *WT* (**A**) and cone-like nuclei in mutant retinas (**B, C, E**). *E168d2/+* have many ONL nuclei with decondensed chromatin (**B, E** white arrows) which are either displaced cones or rods with disorganized nuclear architecture. *E168d2neo/+* also have several photoreceptors with 'cone-like' patterns that are mislocalized to the middle and inner ONL (**C,** white arrows). Highly electron dense nuclei (white pentagon), corresponding with pyknotic nuclei, were identified in the ONL of *E168d2/+* (**E**) and *E168d2neo/+* (**F**) samples but not in *WT* (**D**). **G**) Quantification of percentage area of nuclei consisting of condensed heterochromatin show a significant reduction of rod heterochromatin in *E168d2/+* but not *E168d2neo/+* retinas (*$p<0.05$; Error bars: SEM). Image scale bars: 2μM.

Fig 2.7)

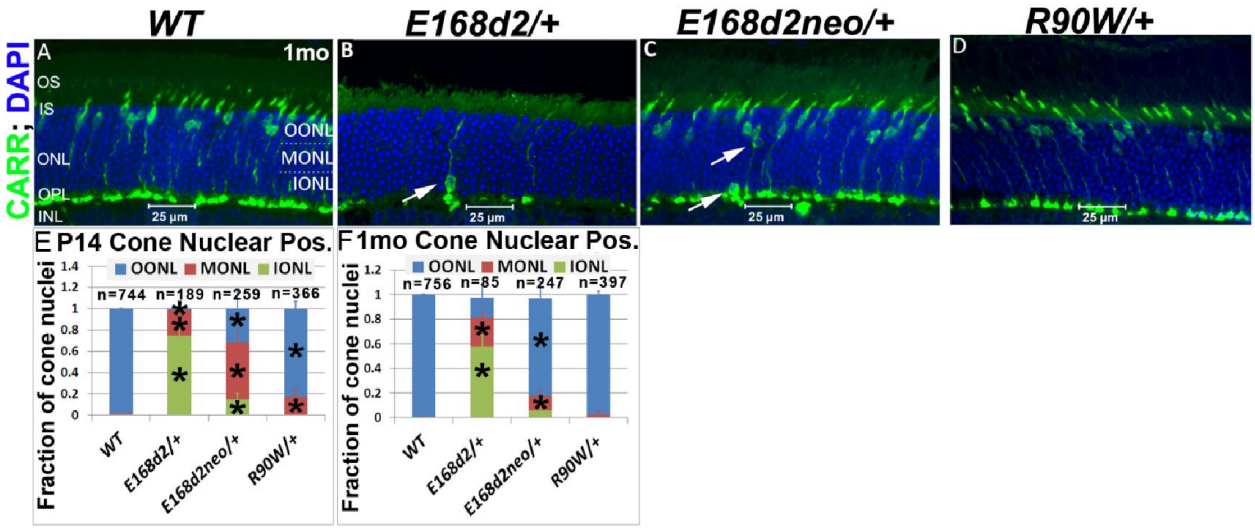
WT
E168d2/+
E168d2neo/+
R90W/+
CARR; DAPI
A
1mo
OS
IS
ONL
OPL
INL
OONL
MONL
IONL
25 µm
B
C
D
E P14 Cone Nuclear Pos.
F 1mo Cone Nuclear Pos.
Fraction of cone nuclei
OONL MONL IONL
n=744 n=189 n=259 n=366
n=756 n=85 n=247 n=397
WT
E168d2/+
E168d2neo/+
R90W/+

Figure 2.7) Heterozygous *E168d2/+*, *E168d2neo/+* and *R90W/+* mice display abnormal cone nuclear localization in developing and adult retina. A-D) Sagittal retinal sections of the indicated mice at 1mo, stained for cone arrestin (CARR) (green) and nuclear marker DAPI (blue). To assess cone nuclear location, the ONL was arbitrarily divided into three zones, outer ONL (OONL), mid ONL (MONL) and inner ONL (IONL). **A**) *WT* cone nuclei were found only in the OONL, while *E168d2/+, E168d2neo/+* and *R90W/+* had varying numbers of cones localized to IONL or MONL (**B**&**C** white arrows). **E, F**) Cone nuclear position was quantified by counting the fraction of CARR+ nuclei in each ONL zone of sagittal retinal sections from P14 or 1MO mice of the indicated genotype (*$p<0.05$).

Fig 2.8)

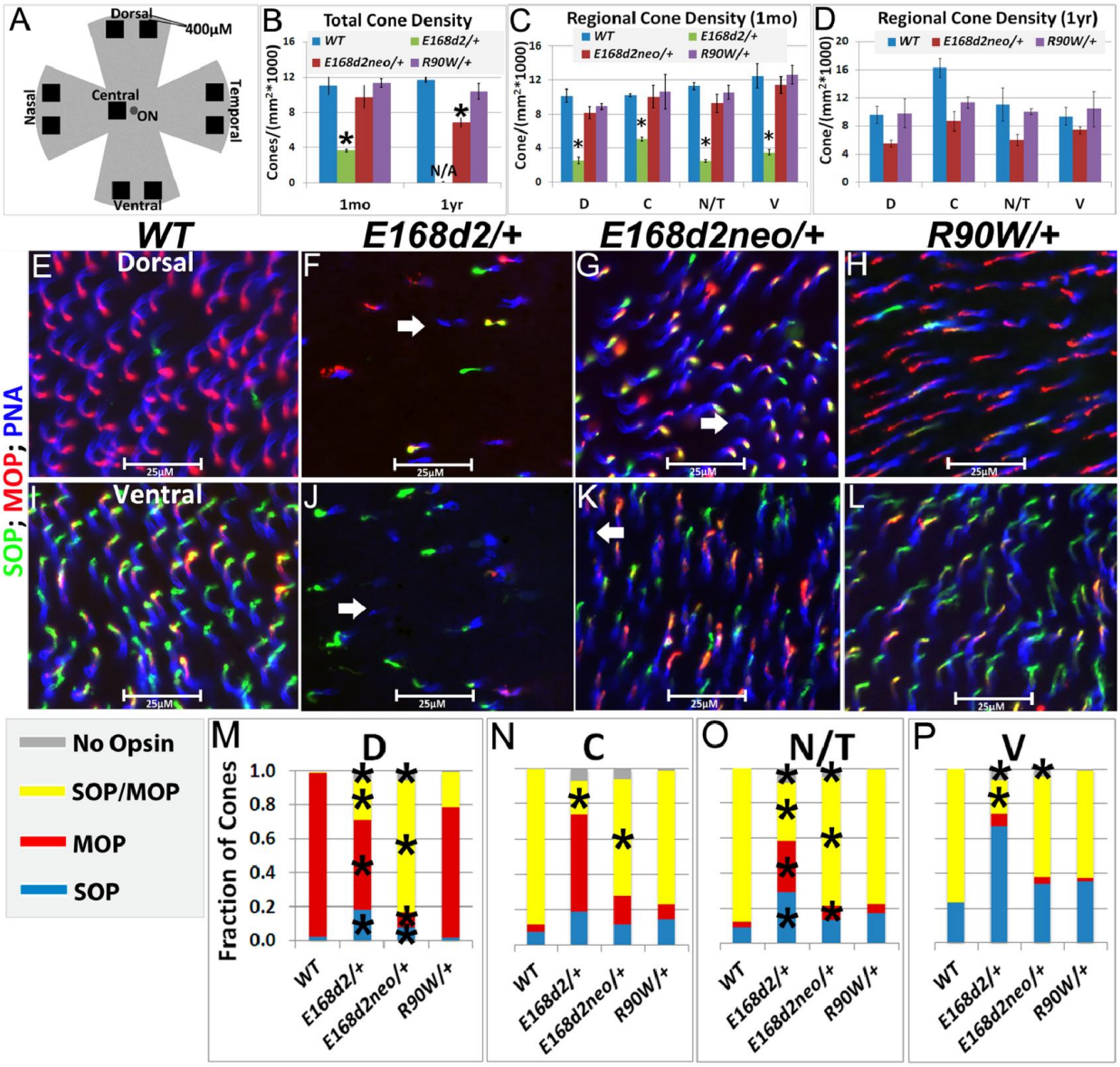
A
Dorsal
400µM
Nasal
Central
ON
Temporal
Ventral
B
Total Cone Density
WT
E168d2/+
E168d2neo/+
R90W/+
Cones/(mm²*1000)
N/A
1mo
1yr
C
Regional Cone Density (1mo)
Cone/(mm²*1000)
D
C
N/T
V
D
Regional Cone Density (1yr)
WT
E168d2neo/+
R90W/+
Cone/(mm²*1000)
D
C
N/T
V
WT
E168d2/+
E168d2neo/+
R90W/+
E
Dorsal
F
G
H
SOP; MOP; PNA
I
Ventral
J
K
L
25µM
No Opsin
SOP/MOP
MOP
SOP
M
D
N
C
O
N/T
P
V
Fraction of Cones
1.0
0.8
0.6
0.4
0.2
0.0
WT
E168d2/+
E168d2neo/+
R90W/+

Figure 2.8) Heterozygous *E168d2/+*, *E168d2neo/+* and *R90W/+* mice display distinct changes in cone density and M/S opsin gradient formation. **A**) Diagram of selected regions of flat-mounted retina for cone density image analyses. **B-D**) Cone density of 1mo and 1yr old mice was determined by counting PNA+ cells on flat-mounted retinas in the dorsal (D), central (C), nasal/temporal (N/T) and ventral (V) regions. Genotype*retinal region interaction (by two-way ANOVA) was significant at 1mo ($p=0.04$) but not 1yr ($p=0.11$), therefore differences in PNA+ cells in each region were tested at 1mo but not 1yr. **B**) Total cone density over all regions (*$p<0.05$). **C-D**) Cone density in each region in 1mo and 1yr old mice (*$p<0.05$). **E-L**) Flat-mounted retinas from 1mo mice of the indicated genotype were stained for OPN1SW (SOP, green), red/green opsin (MOP, red) and the pan cone marker peanut agglutinin (PNA, blue), showing sample images from the dorsal (**E-H**) and ventral (**I-L**) regions. Image scale bars: 25μM. Unlike *WT* samples (**E&I**), *E168d2/+,* (**F&J**) and *E168d2neo/+* (**G&K**) samples show a small number of PNA+ cones that did not express either cone opsin (white arrows). **M-P**) Fraction of cones in each region expressing SOP, MOP, both SOP/MOP or no opsin (*$p<0.05$). Error bars: SEM

Fig 2.9)

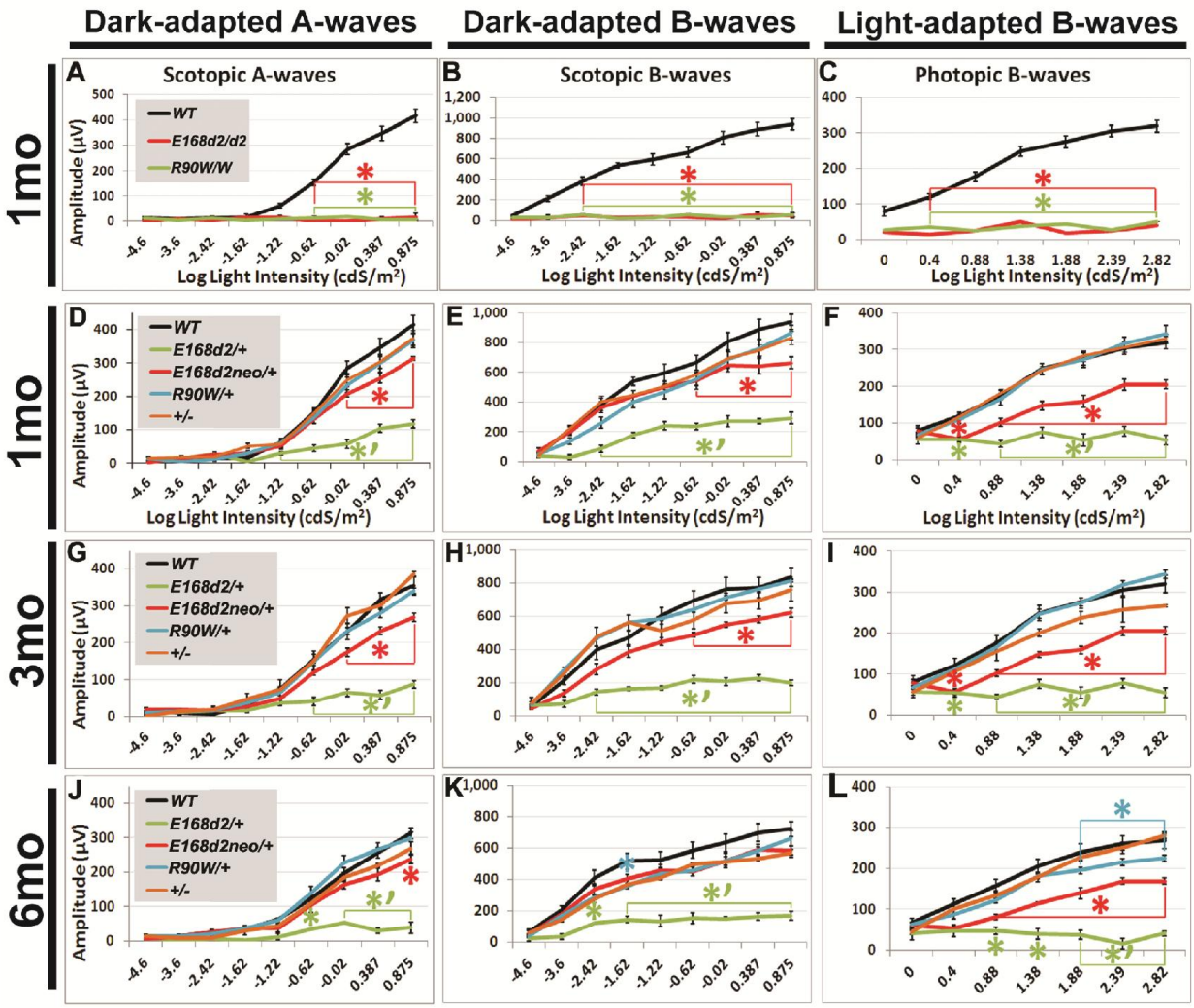
Dark-adapted A-waves
Dark-adapted B-waves
Light-adapted B-waves
1mo
3mo
6mo
A
Scotopic A-waves
B
Scotopic B-waves
C
Photopic B-waves
D
E
F
G
H
I
J
K
L
WT
E168d2/d2
R90W/W
E168d2/+
E168d2neo/+
R90W/+
+/-
Amplitude (μV)
Log Light Intensity (cdS/m²)

Figure 2.9) Graded changes in retinal function in *E168d2* and *R90W* mice. A-C) Retinal function of 1mo homozygous *E168d2/d2* and *R90W/W* mice was assessed by electroretinography. D-L) Retinal function of *E168d2/+, E168d2neo/+* and *R90W/+* and +/- mice was assessed by electroretinography at 1mo (D-F), 3mo (G-I) and 6mo (J-L). Averaged peak amplitude responses for dark-adapted A-waves and B-waves and light-adapted B-waves are plotted against the log of the flash intensity (Log [cd*s/m^2]). Genotype*flash intensity interactions for peak amplitude (by two-way ANOVA), were significant ($p<0.05$) at all ages for each wave form tested. *E168d2/+* mice show severe deficits in all wave responses at each age compared to responses from either *WT* or *E168d2neo/+* mice (green vs. black and red line, respectively). Peak responses in *E168d2neo/+* mice are higher than *E168d2/+* (red vs. green line), but remain significantly decreased compared to *WT* (red vs. black line) with exceptions for 6mo dark-adapted B-waves (K). *R90W/+* and +/- mice have mostly normal retinal function (blue or orange vs. black line) but *R90W/+* have subtle significant deficits in light-adapted B-waves at 6mo (L, blue vs. black line). (Relative to *WT*: *$p<0.05$; relative to *E168d2neo/+*: *'$p<0.05$, brackets indicate all enclosed data points are significant). Error bars: SEM.

Fig. 2.10)

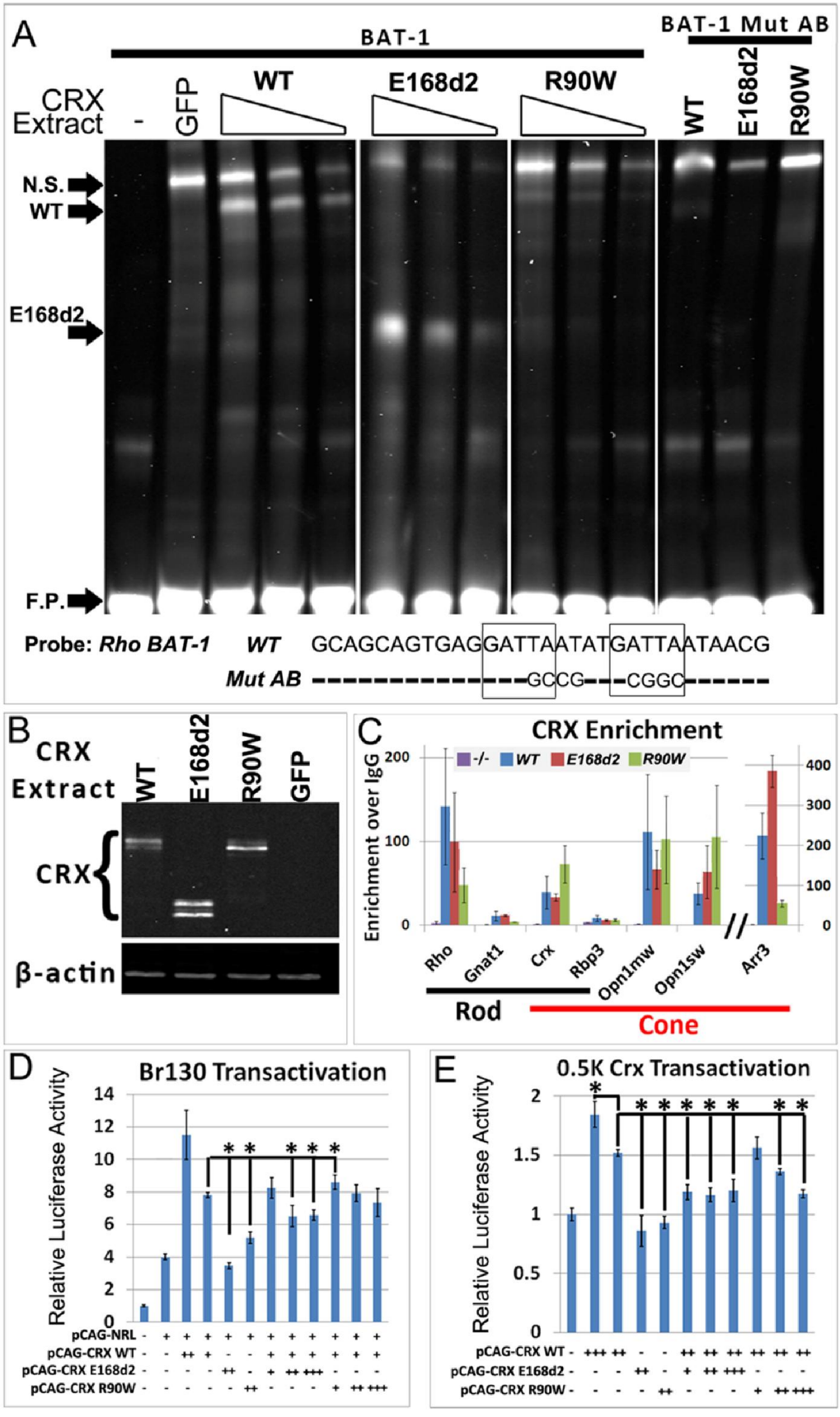
A
BAT-1
BAT-1 Mut AB
CRX Extract
-
GFP
WT
E168d2
R90W
WT
E168d2
R90W
N.S.
WT
E168d2
F.P.
Probe: Rho BAT-1 WT GCAGCAGTGAGGATTAATATGATTAATAACG
Mut AB ----------GCCG---CGGC------
B
CRX Extract
WT
E168d2
R90W
GFP
CRX
β-actin
C
CRX Enrichment
-/-
WT
E168d2
R90W
Enrichment over IgG
Rho
Gnat1
Crx
Rbp3
Opn1mw
Opn1sw
Arr3
Rod
Cone
D
Br130 Transactivation
Relative Luciferase Activity
pCAG-NRL
pCAG-CRX WT
pCAG-CRX E168d2
pCAG-CRX R90W
E
0.5K Crx Transactivation
Relative Luciferase Activity
pCAG-CRX WT
pCAG-CRX E168d2
pCAG-CRX R90W

Figure 2.10) CRX$^{[E168d2]}$ and CRX$^{[R90W]}$ affect target gene transcription through distinct molecular mechanisms. **A**) Electrophoresis mobility shift assays (EMSA) to measure the DNA binding activity of HEK293-expressed CRX$^{[E168d2]}$ and CRX$^{[R90W]}$ protein to the *Rho BAT-1* motif. *CRX* mammalian expression vectors *pCAGIG-CRX WT*, *E168d2* or *R90W* and their negative control vector *pCAG-Gfp* (-) were individually transfected into HEK293 cells. A 2-fold dilution series of nuclear protein extract made from each transfection were incubated with 700IRdye-labeled DNA probes, either *BAT-1* or mutated *BAT-1* lacking CRX-binding sites (*BAT-1 Mut AB*) (sequence below EMSA). The resulting protein/DNA complexes were resolved on 5% non-denaturing PAGE gel and imaged on the LI-COR Odyssey system. Novel bands corresponding to protein/DNA complexes from full-length CRXs (FULL, either WT or LF), truncated CRX (E168d2) and non-specific (N.S.) protein(s), as well as free probe (F.P.) are indicated. **B**) Western blot for the amount of CRX protein (antibody 119b-1) present in each nuclear extract. To compare binding activity, CRX protein levels from different nuclear extracts were normalized and equal ratios were used for EMSA reactions. **C**) Quantitative chromatin immunoprecipitation assays for promoter occupancy of CRX in P14 *WT* and *E168d2/d2*, *R90W/W* and *-/-* mutant retinas. The indicated target gene promoters were used in qPCR assays on CRX-immunoprecipitated chromatin and the results are presented as enrichment of CRX over IgG control. Like WT protein, both CRX$^{[E168d2]}$ and CRX$^{[R90W]}$ are enriched on the promoters analyzed. **D-E**) Dual-luciferase assays showing combined transactivation activity of NRL, CRX, CRX$^{[E168d2]}$ and CRX$^{[R90W]}$ in transfected HEK293 cells on two promoter-luciferase reporters, *Rhodopsin* (*BR-130*) (**D**) and *Crx* (*0.5K* mouse *Crx*) (**E**). Comparing to pcDNA3.1hisc control, for BR-130: all test plasmid combinations were significantly different; for 0.5K Crx: only pCAG-E168d2 and pCAG-R90W were not significantly different. Significant differences of post hoc comparisons are indicated by bracketed '*' (FDR $p<0.09$; comparisons were made to the left most bracket; Error bars: STDEV).

Fig. 2.11)

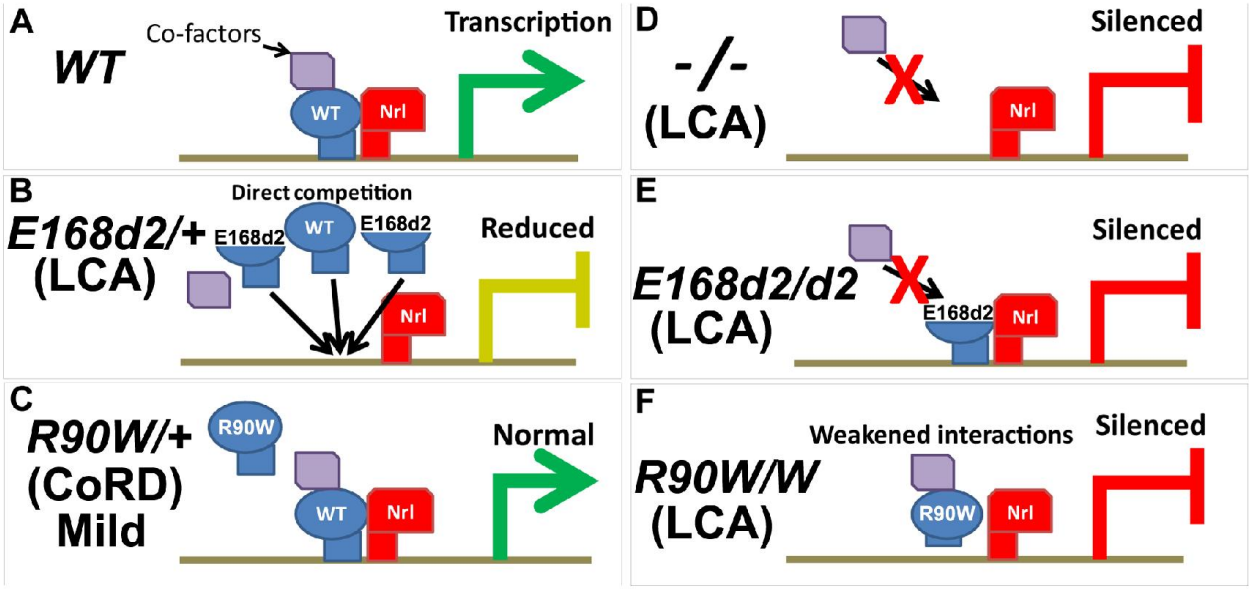
A
WT
Co-factors
WT
Nrl
Transcription
D
-/-
(LCA)
Nrl
Silenced
B
E168d2/+
(LCA)
Direct competition
E168d2
WT
E168d2
Nrl
Reduced
E
E168d2/d2
(LCA)
E168d2
Nrl
Silenced
C
R90W/+
(CoRD)
Mild
R90W
WT
Nrl
Normal
F
R90W/W
(LCA)
Weakened interactions
R90W
Nrl
Silenced

Figure 2.11) Models for CRX$^{[E168d2]}$ and CRX$^{[R90W]}$ mechanisms of pathogenesis in *K-IN* mice. **A**) In *WT* mice, CRX binds to DNA, recruits and synergizes with co-factors including NRL and chromatin modulators to promote target gene transcription. **B**) In *E168d2/+* mice, the antimorphic CRX$^{[E168d2]}$ protein directly competes with CRX WT to act on target gene promoters. Since CRX$^{[E168d2]}$ protein is overexpressed compared to WT, its antimorphic effect is amplified and results in severe reductions in target gene transcription and retinopathy resembling LCA. **C**) In *R90W/+* mice, CRX$^{[R90W]}$ protein does not impair the function of CRX WT and transcription in adult mice is largely normal. *R90W/+* mice have only a mild retinal phenotype similar to a late-onset CoRD. **D**) In -/- mice, the loss of CRX leads to the failure to recruit co-factors to target gene promoters and expression is silenced. **E**) In *E168d2/d2* mice, CRX$^{[E168d2]}$ protein binds to the promoters of target genes, which interferes with the activity of other transcription factors, resulting early-onset LCA with a faster course of retinal degeneration than -/-. **F**) In *R90W/W* mice, CRX$^{[R90W]}$ protein was found to still associate with target gene promoters despite having reduced DNA binding in vitro. However, this confers only modest gains in target gene transcription over -/- and does not establish normal retinal function. Thus, CRX$^{[R90W]}$ protein is a functionally impaired protein but retains some residual transactivation activity. *R90W/W* mice most closely model LCA.

Chapter III

–

Expression Profiling of *Crx Knock-IN* Mouse Retinas

Author: Nicholas Tran

Co-authors: Shiming Chen, Philip Ruzycki

Microarray experimental data and analysis contained within this chapter were adapted from:

Tran NM, Zhang A, Zhang X, Huecker J, Hennig A, Chen S Mechanistically Distinct Mouse Models For *CRX*-Associated Retinopathy. PLOS Genetics, *in press*

Chapter III

Introduction- Assessment of retinal gene expression in *E168d2* and *R90W* mouse models

Given CRX's critical role in photoreceptor development and gene expression, I hypothesized that the distinct phenotypes observed in the *E168d2* and *R90W* mouse models were directly related to unique abnormalities in photoreceptor gene expression. Previous studies have shown that retinal function and morphology are directly related to photoreceptor gene expression and can be greatly affected by disruptions in the retinal transcription factor network[1–6]. Our goal was to correlate the *E168d2* and *R90W* phenotypes with their specific retinal gene expression profiles. We assessed whole-genome mRNA expression in P10 heterozygous and homozygous and P21 heterozygous *E168d2* and *R90W* mice using expression microarrays and RNA-Seq technologies. We validated several expression changes using immunofluorescent histochemistry and qRT-PCR. Given CRX's widespread function in photoreceptor gene expression, phenotypic differences could stem from different types of expression abnormalities. We sought to determine if disease type and severity was affected by changes in different sets of genes or by graded changes in a common set of genes. Assessing the commonalities and differences in gene expression will aid to our understanding of what genes and cellular pathways underlie the distinct pathologies of these mouse models.

In addition, we correlated expression differences with the DNA binding of CRX and the rod-specific transcriptional co-regulator NRL in photoreceptors. Previous studies identified a strong correlation with genomic CRX[7] and NRL[8] DNA-binding and gene expression. Investigating whether this correlation is maintained in *E168d2* and

R90W mice was thought to be especially critical to determine whether or not mutant CRX proteins were primarily affecting direct target genes of WT CRX.

Results

3.1. Gene expression in P10 homozygous *Knock-IN* mice

3.1.i) Microarray analysis of gene expression changes in homozygous mutants

We first compared retinal transcription profiles of homozygous *E168d2neo* and *R90Wneo* mice with *WT* and -/- controls using Illumina gene expression microarrays to determine the effects of mutant CRX protein on retinal gene expression. We chose to use homozygous mice from the *Neo*+ sublines, which express the mutant protein at lower levels than the final lines, for the gene profiling analyses to avoid alterations in gene expression that could arise strictly from mutant CRX overexpression. Unlike subline differences observed in heterozygous mutant mice, morphological and functional characterization demonstrated that the phenotypes of homozygous mice from *neo*+ and final *neo*- sublines were indistinguishable. Expression profiling results were validated by qRT-PCR for several genes in all sublines. RNA from sex-matched pairs of P10 retinas for each genotype was reverse transcribed into cDNA, which was hybridized onto Illumina mouse Ref6 expression microarrays. Microarray analyses showed a high degree of overlap of differentially expressed genes in homozygous *E168d2neo*, *R90Wneo* and *-/-* mice (Fig 3.1A&B). The complete list of differentially expressed genes is available in Tables S2 & S3 (*Tran NM et al. PLOS Genetics 2013*), and the raw datasets are available at NCBI GEO website (http://www.ncbi.nlm.nih.gov/gds, access number: GSE51184). For downregulated genes: 70.6% of *E168d2neo* and 93.5% of *R90Wneo* genes were shared with *-/-* (Fig 3.1A). For upregulated genes: 59.8% of *E168d2neo* and 75% of *R90Wneo* genes were shared with *-/-* (Fig 3.1B).

While *E168d2neo*, *R90Wneo* and *-/-* mutations affected similar sets of genes, distinct degrees of gene expression changes were observed. Heat map analysis showed the majority of shared downregulated genes were more strongly reduced in *E168d2neo* and *-/-* compared to *R90Wneo* (Fig 3.1D). The less reduced expression of downregulated CRX target genes in *R90Wneo* mice suggests that *R90Wneo* retains some weak ability to promote transcription. *E168d2neo* and *-/-* had similar heat map profiles but several key photoreceptor genes were lower in *E168d2neo* including: *Rho*, *Arr3*, *Ramp3*, *Drd4*, *Cpm*, and *Pde6c* (Accessions: NM_145383.1, NM_133205.3, NM_019511.3, NM_007878.2, NM_027468.1, AF411063.1, respectively). The more severe reduction in gene expression in *E168d2* is consistent with its accelerated photoreceptor degeneration compared to *R90W* and *-/-*. It is notable that many shared downregulated genes encode proteins in the phototransduction and visual cycle pathways essential for establishing vision (Fig 3.1E), including: *Opn1sw, Opn1mw, Gnat1, Gnat2, Rcvrn, Pde6a, Pde6g,* (Accessions: NM_007538.3, NM_008106.2, NM_008140.2, NM_008141.2, NM_009038.2, NM_146086.2, NM_012065.2, respectively) *Rho, Arr3,* and *Pde6c*. Other downregulated genes encode proteins with function in key cellular processes, including metabolism and mitochondrial function, membrane stability/function, synaptic function, intercellular transport, and transcription/translation (Fig 3.1E), which likely contribute to the morphological and functional defects. Furthermore, many downregulated genes were associated with the human diseases RP, LCA and CoRD (Table 3.1, https://sph.uth.edu/retnet/), overlapping with those reported for *CRX* mutations.

3.1.ii) RNA-Seq analysis of gene expression changes in homozygous mutants

In addition assessing retinal gene expression using microarrays, we performed Next-generation RNA sequencing (RNA-Seq). Next-generation sequencing provides unbiased

quantitative measurements of an RNA population. It has been shown to yield more robust measures of gene expression allowing for greater resolution of genes expressed at low levels and small differences in expression. RNA-Seq has effectively been used in the *Nrl KO* mouse to identify additional changes in gene expression, when compared to microarray[1,3,8–10]. Taking these findings into account, we decided to further characterize the retinal gene expression of P10 homozygous *E168d2* and *R90W* mice using RNA-Seq.

The mRNA from sex-matched pairs of P10 *WT* and homozygous *E168d2* and *R90W* mouse retinas was sequenced using the Illumina HiSeq platform. Unlike microarray experiments, *E168d2* and *R90W Neo*- mice were used since these mice most closely model human disease. Sequencing reads were aligned to the genome and the raw number of reads in counts per million (CPM) per gene were determined (Table 3.2). Genes with a minimum read count of ≥5 CPM in at least one genotype were analyzed for differential expression compared to *WT*. In *E168d2/d2* retinas 673 genes were found to be differentially expressed by more than 2-fold (425 downregulated, 248 upregulated)(FDR < 0.05). In *R90W/W* mice 264 genes were differentially expressed (196 downregulated, 70 upregulated) by the same criteria. For both genotypes, more differentially expressed genes were detected by the RNA-Seq method than by microarray and a high degree of overlap was observed between the datasets, particularly in downregulated genes (Fig 3.2A-F). In *E168d2*/*d2*, 139 downregulated genes are shared between microarray (56%, 139/250) and RNA-Seq (35%, 139/396) platforms, while a lower percentage of upregulated genes are shared between microarray (39%, 37/96) and RNA-Seq (15%, 37/248) (Fig 3.2A-B). In *R90W*/*W*, 46 downregulated genes are shared between microarray (61%, 46/76) and RNA-Seq (23%, 46/196) platforms (Fig 3.2A-B), while a lower percentage of upregulated genes are shared between microarray (54%, 6/11) and RNA-Seq (9%, 6/70) (Fig 3.2C-D). The improved sensitivity of the RNA-Seq platform is demonstrated by the detection of genes not detected in microarray like *Opn1sw*, a gene expressed in cones

which comprise only 3% of retinal cells. Differentially expressed genes in *E168d2* and *R90W* RNA-Seq data share even more genes than their genotype-matched microarrays (168 downregulated, 48 upregulated) (Fig 3.2E-F), indicating platform-specific differences in gene expression profiles. Overall, RNA-Seq results in homozygous mice match well with microarray results and provide a more robust profile of retinal gene expression in *E168d2* and *R90W* mice.

We analyzed the expression profiles of homozygous *E168d2* and *R90W* retinas with particular focus on the expression of known rod and cone genes. Volcano plots of expression fold-change compared to *WT* show that *E168d2/d2* and *R90W/W* have a general trend favoring downregulation of expression (Fig 3.3A-B). We tracked the expression of 12 genes with known function in photoreceptors (labeled in white, Fig 3.3A-C): genes involved in rod phototransduction (*Rho, Gnat1, Grk1, Rcvrn*), cone phototransduction (*Arr3, Pde6h, Opn1sw, Opn1mw*), transcription in rods (*Esrrβ, Nrl, Nr2e3*), transcription in cones (*Rxrγ*) or transcription in rods/cones (*Crx, Otx2*). *E168d2/d2* and *R90W/W* mice exhibit significantly reduced expression of rod and cone genes involved in phototransduction, a slight reduction in the expression of *Nrl*, while *Rxrγ* was found to be highly overexpressed (Fig 3.3A-B). A scatter plot comparing fold-changes in *E168d2/d2* and *R90W/W*, shows that many genes including several involved in phototransduction (*Arr3, Pde6h, Rho* and *Grk1*) are more strongly downregulated in *E168d2/d2* than *R90W/W* (Fig 3.3C), corresponding with microarray results. These results suggest that both *E168d2/d2* and *R90W/W* have reduced expression of photoreceptor genes and that expression is more strongly impaired in *E168d2/d2* than *R90W/W*.

3.1.iii) Validation of microarray and RNA-Seq results for homozygous mice

To confirm graded changes in target gene expression, levels of several key CRX target genes were validated in homozygous mice of all mutant lines using IF staining (Fig 3.3D-G)

and/or qRT-PCR analyses (Fig 3.3 H-K, Table 3.1, Table 3.3). IF staining showed that homozygous *E168d2neo* retinas failed to produce rhodopsin (RHO) in contrast to *-/-,* which still made a low amount of RHO (Fig 3.3 E vs. G). This suggests that $CRX^{[E168d2]}$ protein has an inhibitory effect on *Rho* expression beyond complete loss of CRX protein. Homozygous *R90Wneo* retinas, on the other hand, produced RHO at a level higher than *-/-* but much lower than *WT* retinas (Fig 3.3 F vs. G & D). Expression changes of a number of genes in the retinas of homozygous mutants from the *neo+* and final *neo-* lines were validated using qRT-PCR, including the rod gene *Rho* and the cone genes *Arr3, Opn1sw* and *Opn1mw* (Fig 3.3 H-K, Table 3.3). The results, presented as fold change (FC) relative to *WT,* from P10 homozygous mice of the 'low expression' subline and final line of each mutation were compared (Fig 3.3H-K). *Rho* expression was essentially abolished in both *E168d2* and *E168d2neo* mice. In contrast, *R90W* and *R90Wneo* mice expressed *Rho* at levels slightly higher than *-/-* (Fig 3.3H). These results are consistent with the microarray and IF results described above. Expression of the cone gene *Arr3* was not detectable in *E168d2* or *E168d2neo* mice, while residual amounts were detected in *R90W, R90Wneo* and *-/-* mice (Fig 3.3I). *Opn1sw* and *Opn1mw* were strongly downregulated in homozygous mice of all models. The loss of expression of genes involved in rod/cone phototransduction explains the loss of visual function in these mice. Together, our results suggest that the *E168d2* mutation produced a direct antimorphic effect on photoreceptor gene expression beyond CRX deficiency, while *R90W* is a hypomorph mutation, resulting in a CRX protein with impaired residual transcriptional regulatory function.

3.2) Gene expression in P10 and P21 heterozygous *Knock-IN* mice

3.2.i) RNA-Seq analysis of gene expression changes in heterozygous mutants

Since *CRX*-associated retinopathies are typically inherited in a dominant fashion, the gene expression profiles of heterozygous *E168d2* and *R90W* mouse retinas were assessed to

determine potential disease pathways contributing to the phenotypes of each model. mRNA from sex-matched retinas of *E168d2/+, E168d2neo/+* and *R90W/+* mice were sequenced, aligned and the fold-change compared to *WT* was determined, as above. Ages P10 and P21 were selected to give both a developmental and a mature retina timepoint. Volcano plots of P10 fold-changes compared to *WT* for *E168d2/+* and *E168d2neo/+* show a general favoring downregulation, while few genes in *R90W/+* were >2-fold different (Fig 3.4A-C). Tracking of the same set of known photoreceptor genes as in homozygous analysis reveals that rod and cone phototransduction genes (*Pde6h, Rho, Rcvrn, Gnat1, Arr3, Opn1sw, Opn1mw*) are downregulated in both *E168d2/+* and *E168d2neo/+*. *Rxrγ* was found to be upregulated in *E168d2/+* but not *E168d2neo/+*. None of these genes were >2-fold differentially expressed in *R90W/+*. *E168d2/+* and *E168d2neo/+* show a high degree of overlap in downregulated (*E168d2/+*: 52%, 71/136 and *E168d2neo/+*: 83%, 71/85) and upregulated (*E168d2/+*: 39%, 24/61 and *E168d2neo/+*: 63%, 24/38) genes (Fig 3.4D-E). The few genes that were differentially expressed in *R90W/+* exhibited overlap with *E168d2/+* (60%, 12/20 downregulated and 58%, 7/12 upregulated) (Fig 3.4F-G).

Volcano plots of P21 *E168d2/+, E168d2neo/+* and *R90W/+* show similar patterns to P10 data with some notable differences (Fig 3.4H-J). While several of the tracked phototransduction genes remained downregulated in *E168d2/+* (*Opn1sw, Pde6h, Rcvrn, Opn1mw, Rho, Arr3*), only the cone-specific *Opn1sw* and *Pde6h* were found to be downregulated in *E168d2neo/+*, this recovery in expression of rod genes is consistent with the improvement in rod morphology and survival in *E168d2neo/+* mouse retinas (Fig 3.4H-I). Few genes overall and none of the tracked genes were differentially expressed in *R90W/+* mouse retinas (Fig 3.4J). *E168d2/+* and *E168d2neo/+* show a high degree of overlap in downregulated (*E168d2/+*: 46%, 69/150 and *E168d2neo/+*: 83%, 69/83) and upregulated (*E168d2/+*: 26%, 12/47 and *E168d2neo/+*: 63%, 12/19) genes (Fig 3.4K-L). The few downregulated genes in *R90W/+* exhibited overlap with

E168d2/+ (81%, 22/27) while the upregulated genes exhibited little overlap (4%, 1/27) (Fig 3.4M-N). At both P10 and P21 more differentially expressed genes were identified in *E168d2*/+, indicating changes may either be stronger in *E168d2/+* pushing them past the 2-fold cut-off or affected in *E168d2/+* but not in *E168d2neo*/+ mouse retinas. To discern between these two possibilities, scatter plots of the fold-change to *WT* of *E168d2/+* vs. *E168d2neo/+* or *R90W/+* were made at P10 and P21 (Fig 3.5A-D). In P10 *E168d2/+* vs. *E168d2neo/+*, few genes were >2-fold different. Of the tracked genes, only the cone-specific *Pde6h* and *Arr3* were >2-fold different, with both being higher in *E168d2neo/+* (Fig 3.5A). Similarly to P10, few genes were >2-fold different in P21 *E168d2/+* vs. *E168d2neo/+*. Of the tracked genes, only *Pde6h* and the rod-specific *Rcvrn* were different with both being higher in *E168d2neo/+* (Fig 3.5B). As expected, in both P10 and P21*E168d2/+* vs. *R90W/+* several genes, including many of the tracked genes, were expressed >2-fold higher in *R90W/+* than *E168d2/+*. Overall these results indicate that photoreceptor transcription is highly disrupted in *E168d2/+* and *E168d2neo/+* but only subtly affected in *R90W/+* correlating with the minor phenotype of *R90W/+* mice. Since few genes are >2-fold different between *E168d2/+* and *E168d2neo/+*, the more severe phenotype of *E168d2*/+ is unlikely to be caused by changes in a distinct set of genes and is more likely related to small graded changes in the same set of changes.

3.2.ii) Validation of RNA-Seq results for heterozyous mutants

To determine if gene expression changes in heterozygous mice followed the same trend as homozygous mutants, expression of the selected CRX target genes, *Rho, Arr3, Opn1sw* and *Opn1mw,* was evaluated in heterozygous mutants using IF staining of retinal sections at 1mo of age (Fig 3.5E-H) and/or qRT-PCR at P10 and P21 (Fig 3.5I-L, Tables 3.3 & 3.4). IF staining for RHO at 1mo showed that *E168d2/+* mice displayed low intensity of RHO staining, some of

which was mislocalized to the ONL (Fig 3.5 F vs. E), suggesting impaired RHO trafficking. This phenotype was not seen in *E168d2neo/+* and *R90W/+* retinas (Fig 3.5G, H vs. E). qRT-PCR analyses showed that *E168d2/+* mice exhibited persistent downregulation of all genes tested in both P10 and P21, despite some degree of recovery at P21 (Fig 3.5I-L, Tables 3.3 & 3.4). Expression of these genes was also decreased in *E168d2neo/+* mice, but significant improvements were seen for *Rho* and *Opn1mw*, compared to *E168d2*/+ mice. The more severe impairment of gene expression in *E168d2/+* compared to *E168d2neo/+* demonstrates the dosage effect of $CRX^{[E168d2]}$ mutant protein. In contrast, *R90W/+* and +/- mice exhibited reduction in the expression of some genes at P10 but normal expression was observed at P21. The degree of expression changes in individual mutants varied from gene to gene. These results suggest that $CRX^{[E168d2]}$ mutant protein actively impaired CRX target gene transcription in the presence of WT protein, consistent with an antimorphic mechanism. This antimorphic effect depends on $CRX^{[E168d2]}$ protein dosage and can be reduced by decreasing $CRX^{[E168d2]}$ expression. In contrast, *R90W/+* essentially phenocopied the phenotype of +/-, suggesting that $CRX^{[R90W]}$ protein did not severely interfere with the function of WT CRX *in vivo*, which allowed for normal photoreceptor gene expression by P21.

3.3. Connecting expression changes with CRX functional role in photoreceptor differentiation

In order to connect the differences in retinal gene expression observed in *E168d2* and *R90W* mice with the functional role of CRX, we performed hierarchical clustering analysis on differentially expressed and compared expression changes with the DNA-binding patterns of CRX and the rod-specific co-regulator NRL. Hierarchical clustering of differentially expressed genes among P10 *E168d2/+, E168d2neo/+, R90W/+, E168d2/d2, R90W/W* and P21 *E168d2/+,*

E168d2neo/+ and *R90W/+* reveals groups of genes that exhibit distinct patterns of expression (Fig 3.6, 3.7). We compared trends in expression in *Nrl KO*, the DNA-binding of CRX in *WT* and *Nrl KO* retinas and the DNA-binding of NRL in *WT* retinas and performed G-profiler pathway analysis on each of these groups.

Here we highlight two of the designated groups which show the most dramatic changes in gene expression. Group 1 (Fig 3.6) is composed of genes that are primarily downregulated across genotypes. Expression of genes within this group is noticeably lower in P10 *E168d2/d2* retinas and graded changes are seen in other genotypes, generally: *R90W/W* < P10 *E168d2/+, E168d2neo/+* < P21 *E168d2/+, E168d2/+* < P10, P21 *R90W/+* (Fig 3.6A). Comparison to the retinal expression of P21 *Nrl KO* mice as determined by RNA-Seq[10], in which rods are converted to a 'cone-like' fate[11], shows that genes in Group 1 are comprised of genes that are both enriched in rods (Fig 3.6A, Log_2(FC *WT/Nrl KO*) column, purple color) or enriched in cones (Fig 3.6A, Log_2(FC *WT/Nrl KO*) column, green color). Additionally, comparison of genes to the genomic binding patterns of CRX[7] and NRL[8] reveal a high degree of CRX binding was associated with genes in group 1 in both *WT* (72%) and *Nrl KO* (57%) retinas and NRL binding in WT (76%) retinas (Fig 3.6A, NRL ChIP and CRX ChIP columns). This suggests a large percentage of genes in Group 1, the most strongly downregulated set of genes, are direct targets of CRX and NRL *in vivo*. G:profiler (http://biit.cs.ut.ee/gprofiler/) pathway analysis shows that genes in Group 1 are highly associated with photoreceptor specific processes including: visual perception, phototransduction, photoreceptor outer segment, retina development in camera-type eye etc. (Fig 3.6B). The Cell Specific Expression Analysis tool (CSEA, http://genetics.wustl.edu/jdlab/csea-tool-2/), which associates inputted gene lists with expression profiles from 27 different brain cell-types (Fig 3.6 C), suggests that genes from Group 1 are highly associated with rod and cone-specific expression.

Group 6 is primarily composed of genes that are the most upregulated across genotypes, excluding group 8 which was largely composed of non-retinal genes attributable to sample contamination (Fig 3.7). Expression is generally more upregulated in P10 *E168d2/d2* mice, suggesting that both downregulation and upregulation of gene expression are most severe in *E168d2/d2* mice (Fig 3.7A). Graded changes are seen amongst genotypes, similar to Group 1, but appear to be more age dependent than genotype dependent with P10 showing greater changes than P21 samples (Fig 3.7A). Comparison to gene expression in P21 *Nrl KO* retinas shows that genes in Group 6 are primarily associated with genes that are either not enriched in rods vs. cones or are specifically enriched in cones (Fig 3.7A, Log_2(FC *WT/Nrl KO*) column, green color). A low degree of CRX DNA-binding in *WT* (24%) and *Nrl KO* (35%) retinas and reduced percentage of NRL DNA-binding in *WT* (57%) retinas compared to genes in group 1. This suggests that the genes in Group 6 are largely indirect targets of CRX and misregulation may be due to secondary effects. G:Profiler analysis shows that genes in Group 6 are associated with 3 GO processes: ion transport, basement membrane and transporter activity (Fig 3.7B). Upregulation of genes involved in ion transport and transporter activity are of interest as phototransduction is driven by cGMP-mediated ion channel response. Of particular interest is *Cngb3* (NM_013927), a cone-specific cyclic nucleotide-gated (CNG) channel that has been associated with achromatopsia and cone degeneration[12,13]. The CSEA tool indicates association of genes in Group 6 most strongly with cones but also several other brain cell types from different brain regions (Fig 3.7C). It is unclear if the association of Group 6 genes with cone-specific expression is indicative of *E168d2* and *R90W* photoreceptors adopting a more 'cone-like' state or shared developmental defects with photoreceptors in *Nrl KO* retinas. However, none of the 'cone-specific' genes identified in Group 6 are associated with cone phototransduction. CSEA results suggest that genes in Group 6 are not exclusively associated with photoreceptor expression, particularly for rods. Overall analysis of genes in Groups 1 and 6 indicate the downregulated genes in *E168d2* and *R90W* mice are primarily direct targets of

CRX and NRL and are associated with photoreceptor-specific functions, while upregulated genes are largely indirect targets of CRX and are largely not associated with photoreceptor function.

Discussion

Our results indicate the increased utility of next-generation RNA sequencing over microarray platforms. Parallel comparison of gene expression by RNA-Seq and microarray in homozygous *E168d2* and *R90W* mice, show that RNA-Seq yields greater numbers of differentially expressed genes and improves the detection of genes expressed at low levels or by a small percentage of the cell population, namely cones in the mouse retina. Cross platform analysis shows a high degree of overlap (Fig 3.2), suggesting that comparing results between platforms is possible. Discussion in this section will focus on results from RNA-Seq experiments due to their improved sensitivity.

Expression profiling of *E168d2* and *R90W* mouse retinas suggests that $CRX^{[E168d2]}$ impairs target gene transcription in a dosage dependent manor, while $CRX^{[R90W]}$ weakly promotes expression. In both heterozygous and homozygous *E168d2* and *R90W* mouse retinas, the expression of a greater number of genes was disrupted and the expression of shared genes was more dramatically altered in *E168d2* retinas. Comparison of expression in *E168d2/d2* to *Crx KO* retinas by microarray, immunofluorescence and qRT-PCR showed that many genes were expressed lower in *E168d2/d2* including: *Rho*, *Arr3*, *Ramp3*, *Drd4*, *Cpm*, and *Pde6c.* This suggests $CRX^{[E168d2]}$ protein had an antimorphic effect on the expression of genes even in the complete absence of WT CRX, possibly by interfering with other co-factors like the homeodomain transcription factor OTX2. Supporting this hypothesis, removal of one allele of *Otx2* from the -/- mouse produced a severe phenotype similar to homozygous *E168d2* mice[14,15].

Chapter III

Since OTX2 and CRX have overlapping spatial and temporal roles in retinal development and share DNA binding domain homology, it is possible that CRX$^{[E168d2]}$ interfered with OTX2 activity, resulting in a stronger phenotype than -/-. Expression of CRX target genes in *R90W/W* was largely improved compared to *E168d2/d2*, correlating with modestly improved morphology (Fig 3.3C, F).

Expression profiling of heterozygous *E168d2, E168d2neo* and *R90W* mouse retinas at P10 and P21 reveal distinct changes in gene expression that correlate with phenotypic severity. Downregulation of CRX target genes associated with photoreceptor function was seen in *E168d2/+* and *E168d2neo/+* at both time points (Fig 3.4), while few genes were downregulated in *R90W/+* retinas. While many critical photoreceptor genes are expressed lower in *E168d2/+* compared to *E168d2neo/+*, overall their expression profiles appear strikingly similar and very few genes were found to be more than 2-fold different between them (Fig 3.4A-B, D-E, H-I, K-L, Fig 3.5A-B). This suggests that the dramatically improved phenotype of *E168d2neo/+* in comparison to *E168d2/+* is related to only modest improvements in the expression of CRX target genes. This finding could have significant impact when considering therapeutic strategies as small gains in CRX target gene transcription could yield large gains in retinal phenotype.

Hierarchical clustering of expression data over all genotypes reveals subsets of genes with characteristic expression patterns with distinct associations with cellular pathways, CRX and NRL DNA-binding and cell-type specific expression (Fig 3.6, 3.7). Genes within the group showing the strongest downregulation across genotypes are associated with pathways related to the function of photoreceptors in vision, a high percentage of CRX and NRL binding, and exhibit either rod or cone-specific enrichment of expression in *WT* mouse retinas (Fig 3.6A-C). Genes within the group showing the strongest upregulation across genotypes are associated with pathways related to the function of ion channels, a low percentage of CRX and NRL

binding, and exhibit either cone-specific enrichment or are not enriched in *WT* retinas (Fig 3.7A-C).

Overall our results suggest that mutations affecting the function of CRX primarily cause the downregulation of direct target genes, which are highly associated with visual processes in photoreceptors. Phenotypic differences between the *E168d2, E168d2neo* and *R90W* mouse models are due to graded changes in expression in similar sets of genes and small changes in expression levels of these genes can have a dramatic effect on retinal phenotype.

For detailed Materials and methods see Appendix B.

Chapter III

References

1. Hsiau, T. H. *et al.* The cis-regulatory logic of the mammalian photoreceptor transcriptional network. *PLoS One* **2e643,** (2007).

2. Yoshida, S. *et al.* Expression profiling of the developing and mature Nrl-/- mouse retina: identification of retinal disease candidates and transcriptional regulatory targets of Nrl. *Hum. Mol. Genet.* **13,** 1487–503 (2004).

3. Akimoto, M. *et al.* Targeting of GFP to newborn rods by Nrl promoter and temporal expression profiling of flow-sorted photoreceptors. *Proc Natl Acad Sci U S A* **103,** 3890–3895 (2006).

4. Corbo, J. C. & Cepko, C. L. A hybrid photoreceptor expressing both rod and cone genes in a mouse model of enhanced S-cone syndrome. *PLoS Genet.* **1,** 0140–0153 (2005).

5. Hennig, A. K., Peng, G.-H. & Chen, S. Transcription coactivators p300 and CBP are necessary for photoreceptor-specific chromatin organization and gene expression. *PLoS One* **8,** e69721 (2013).

6. Blackshaw, S., Fraioli, R. E., Furukawa, T. & Cepko, C. L. Comprehensive analysis of photoreceptor gene expression and the identification of candidate retinal disease genes. *Cell* **107,** 579–589 (2001).

7. Corbo, J. C. *et al.* CRX ChIP-seq reveals the cis-regulatory architecture of mouse photoreceptors. 1512–1525 (2010). doi:10.1101/gr.109405.110.CRX

8. Hao, H. *et al.* Transcriptional regulation of rod photoreceptor homeostasis revealed by in vivo NRL targetome analysis. *PLoS Genet.* **8,** e1002649 (2012).

9. Mustafi, D. *et al.* Defective photoreceptor phagocytosis in a mouse model of enhanced S-cone syndrome causes progressive retinal degeneration. *FASEB J.* **25,** 3157–76 (2011).

10. Brooks, M. J., Rajasimha, H. K., Roger, J. E. & Swaroop, A. Next-generation sequencing facilitates quantitative analysis of wild-type and Nrl(-/-) retinal transcriptomes. *Mol. Vis.* **17,** 3034–54 (2011).

11. Daniele, L. L. *et al.* Cone-like morphological, molecular, and electrophysiological features of the photoreceptors of the Nrl knockout mouse. *Invest Ophthalmol Vis Sci* **46,** 2156–2167 (2005).

12. Nishiguchi, K. M., Sandberg, M. a, Gorji, N., Berson, E. L. & Dryja, T. P. Cone cGMP-gated channel mutations and clinical findings in patients with achromatopsia, macular degeneration, and other hereditary cone diseases. *Hum. Mutat.* **25,** 248–58 (2005).

13. Liu, C., Sherpa, T. & Varnum, M. D. Disease-associated mutations in CNGB3 promote cytotoxicity in photoreceptor-derived cells. *Mol. Vis.* **19,** 1268–81 (2013).

14. Koike, C. *et al.* Functional roles of Otx2 transcription factor in postnatal mouse retinal development. *Mol Cell Biol* **27,** 8318–8329 (2007).

15. Nishida, A. *et al.* Otx2 homeobox gene controls retinal photoreceptor cell fate and pineal gland development. *Nat. Neurosci.* **6,** 1255–1263 (2003).

Chapter III

Tables

Table 3.1) Downregulated RP, CoRD, LCA disease genes in P10 homozygous *Crx E168d2neo* and *R90Wneo* mice

Retinitis pigmentosa, autosomal dominant	Retinitis pigmentosa, autosomal recessive	Retinitis pigmentosa, X-linked	Cone or cone-rod dystrophy, autosomal dominant	Cone or cone-rod dystrophy, autosomal recessive	Cone or cone-rod dystrophy, X-linked	Leber congenital amaurosis, autosomal dominant	Leber congenital amaurosis, autosomal recessive
Genes/Loci	Genes/Loci	Genes/Loci	Genes/Loci	Genes/Loci	Genes/Loci	Genes/Loci	Genes/Loci
BEST1	ABCA4	OFD1	(---)	ABCA4	CACNA1F	CRX	AIPL1
CA4	BEST1	RP2	AIPL1	ADAM9	COD2	IMPDH1	CABP4
CRX	C2ORF71	RP6	CORD4	C8ORF37	RPGR	OTX2	CEP290
FSCN2	C8ORF37	RP24	CRX	CACNA2D4			CRB1
GUCA1B	CERKL	RP34	GUCA1A	CDHR1			CRX
IMPDH1	CLRN1	RPGR	GUCY2D	CERKL			GUCY2D
KLHL7	CNGA1		PITPNM3	CNGB3			IQCB1
NR2E3	CNGB1		PROM1	CNNM4			KCNJ13
NRL	CRB1		PRPH2	CORD8			LCA5
PRPF3	DHDDS		RCD1	KCNV2			LRAT
PRPF6	EYS		RIMS1	PDE6C			MERTK
PRPF8	FAM161A		SEMA4A	PDE6H			NMNAT1
PRPF31	IDH3B		UNC119	RAX2			RD3
PRPH2	IMPG2			RDH5			RDH12
RDH12	LRAT			RLBP1			RPE65
RHO	MAK			RPGRIP1			RPGRIP1
ROM1	MERTK						SPATA7
RP1	NR2E3						TULP1
RP63	NRL						
RP9/PAP1	PDE6A						
RPE65	PDE6B						
SEMA4A	PDE6G						
SNRNP200	PRCD						
TOPORS	PROM1						
	RBP3						
	RGR						
	RHO						
	RLBP1						
	RP1						
	RP22						
	RP29						
	RP32						
	RPE65						
	SAG						
	SPATA7						
	TTC8						
	TULP1						
	USH2A						
	ZNF513						

Table 3.1) Downregulated RP, CoRD, LCA disease genes in P10 homozygous *Crx E168d2neo* and *R90Wneo* mice. List of human genes associated with RP, CoRD or LCA whose mouse homologs were identified as being significantly downregulated in P10 microarray of P10 *E168d2neo/neo* or *R90Wneo/Wneo* mice.

Chapter III

Table 3.2) RNA-Seq Read Statistics

Sample ID	ATGACAG	CACCTCC	ATCGAGC	TACTCTA	AGACTGA	CTTGGAA	CCGATTA	GGCAGCG	TGCCCAT	TTTAACT	GGTCCTC	CGGTGGC
Genotype	*WT*	*WT*	*WT*	*E168d2neo/+*	*E168d2neo/+*	*E168d2neo/+*	*E168d2/+*	*E168d2/+*	*E168d2/+*	*R90W/+*	*R90W/+*	*R90W/+*
Age	P10	P10	P10	P10	P10	P10	P10	P10	P10	P10	P10	P10
Reads	27,028,041	24,267,068	28,777,255	35,006,903	29,685,884	38,480,806	34,487,432	25,801,389	28,901,509	29,194,605	25,722,267	31,633,043
Total mapped reads	26,058,498	23,391,189	27,733,983	33,794,352	28,633,410	37,131,356	33,269,023	24,870,183	27,940,547	28,160,862	24,870,589	30,537,240
Percent Mapped Reads	96.4%	96.4%	96.4%	96.5%	96.5%	96.5%	96.5%	96.4%	96.7%	96.5%	96.7%	96.5%
Genes detected	25,527	25,221	25,509	25,914	25,631	26,126	25,932	25,451	25,428	25,678	25,125	25,608
Transcripts detected	79,548	78,930	79,546	80,366	79,990	80,754	80,480	79,574	79,456	79,901	78,999	79,927
# of genes ≥ 5 RPKM	25066	24773	25048	25444	25133	25614	25453	24974	24921	25225	24653	25128
# of genes ≥ 10 RPKM	25008	24732	24998	25374	25084	25558	25407	24917	24849	25168	24581	25068
# of genes ≥ 25 RPKM	24930	24638	24912	25293	24991	25474	25322	24833	24759	25087	24500	24995

Sample ID	CCATCAT	TAACAAG	GAGGCGT	ACTGTCG	GTATTTG	GAGTACG
Genotype	*E168d2/d2*	*E168d2/d2*	*E168d2/d2*	*R90W/W*	*R90W/W*	*R90W/W*
Age	P10	P10	P10	P10	P10	P10
Reads	29,196,532	28,213,713	35,076,477	29,577,419	30,234,871	40,073,473
Total mapped reads	28,107,847	27,170,939	33,826,437	28,535,857	29,186,597	38,713,866
Percent Mapped Reads	96.3%	96.3%	96.4%	96.5%	96.5%	96.6%
Genes detected	25,623	25,597	25,985	25,612	25,597	26,093
Transcripts detected	79,953	79,758	80,540	79,870	79,923	80,916
# of genes ≥ 5 RPKM	25182	25125	25534	25143	25094	25647
# of genes ≥ 10 RPKM	25102	25082	25484	25083	25039	25583
# of genes ≥ 25 RPKM	25026	24991	25406	25008	24947	25509

Sample ID	ACAGATA	CTCAATG	AAATGCA	ACGCGGG	GGAGTCC	CGTCGCT	TCAACTG	TGTTTGT	TACATGG	GTTCTCA	CTGGTGG	AAACCTT
Genotype	*WT*	*WT*	*WT*	*E168d2neo/+*	*E168d2neo/+*	*E168d2neo/+*	*E168d2/+*	*E168d2/+*	*E168d2/+*	*R90W/+*	*R90W/+*	*R90W/+*
Age	P21	P21	P21	P21	P21	P21	P21	P21	P21	P21	P21	P21
Reads	34,792,825	31,461,693	37,264,811	32,793,416	39,973,932	38,171,765	29,435,801	28,863,056	31,321,556	29,755,830	28,187,343	35,778,449
Total mapped reads	33,609,099	30,358,516	35,957,842	31,608,129	38,611,708	36,830,032	28,475,972	27,997,384	30,298,787	28,806,455	27,259,006	34,639,489
Percent Mapped Reads	96.6%	96.5%	96.5%	96.4%	96.6%	96.5%	96.7%	97.0%	96.7%	96.8%	96.7%	96.8%
Genes detected	25,733	25,431	25,937	25,407	25,777	25,627	25,359	25,459	25,548	25,125	25,174	25,701
Transcripts detected	79,925	79,533	80,496	79,472	80,229	79,992	79,389	79,384	79,574	78,982	79,057	80,154
# of genes ≥ 5 RPKM	25313	25001	25480	24970	25341	25156	24911	25005	25117	24697	24733	25274
# of genes ≥ 10 RPK	25271	24936	25439	24930	25287	25094	24850	24956	25041	24650	24664	25229
# of genes ≥ 25 RPK	25188	24870	25358	24850	25221	25000	24760	24867	24972	24583	24603	25145

Table 3.2) Read statistics from RNA-Seq experiments. Read information for individual samples from Illumina Hi-Seq runs.

Table 3.3) qRT-PCR Expression in P10 mouse retinas

		Fold change to *WT*						Fold change to *WT*				
Gene	^Overall p-value (heterozygous mice)	*E168d2/+*	*E168d2neo/+*	*R90W/+*	*R90Wneo/+*	*+/-*	^Overall p-value (homozygous mice)	*E168d2/d2*	*E168d2neo/d2neo*	*R90W/W*	*R90Wneo/Wneo*	*-/-*
Rho	0.011	0.19*	0.27*	1.00	0.38*	0.45*	0.003	4.4e-04*	6.1e-03*	0.26*	0.03*	0.01*
Arr3	0.017	0.06*	0.20*	0.78	0.97	1.20	0.004	5.0e-04*	3.1e-03*	0.06*	0.10*	0.06*
Opn1sw	0.017	0.06*	0.13*	0.35	0.42	0.62	0.082	0.04*	0.04*	0.05	0.12	0.03
Opn1mw	0.008	0.03*	0.07*	0.35	.20*	0.17*	0.047	7.2e-03*	4.8e-03*	7.2e-3*	0.01*	2e-03*
Dnaic1	0.042	0.26	0.27*	0.34*	0.69	0.9	0.016	0.48*	0.66*	0.22*	0.7*	0.65
Myo7a	0.293	0.36	0.46	0.47	0.6	0.74	0.028	0.43	0.32*	0.37*	0.78*	0.27*
Crx	0.0008	1.66*	1.03	1.18	0.93	0.8	0.0003	2.06*	1.46*	0.97	0.68*	0.00*
Otx2	0.067	0.72	0.99	1.24	1.18*	1.62*	0.118	1.49	1.39	1.32	1.7	1.54
Crxos1	0.247	0.62	0.84	0.76	0.58	1.12	0.010	0.36*	0.4*	0.62	0.62*	0.42*
Nrl	0.056	1.11	1.43	1.97*	1.36	0.81	0.108	0.52	0.54	0.64	0.5	0.47
Nr2e3	0.107	1.25	1.49	1.17	1.27	1.16	0.695	1.17	1.10	1.15	1.13	0.44*
Rxrγ	0.008	2.4*	1.68*	1.14	1.70*	1.01	0.046	11.10*	6.55*	6.92*	7.69*	5.8*
Thrb	0.027	0.7	0.76*	1.15*	0.94	1.09	0.166	0.7	0.76	0.78	1.08	0.92
Pias3	0.060	0.52	0.54	0.61	0.73	0.96	0.228	0.71	0.46	0.68	0.66	0.37

^Overall p-value for each primer set was tested in heterozygous and homozygous mice; p<0.09 was considered marginally significant

*p<0.05; reference genes Tuba1b and Ubb

Table 3.3) qRT-PCR Expression in P10 mouse retinas. ^Overall p-value for each primer set was tested in heterozygous and homozygous mice; p<0.09 was considered marginally significant. For all comparisons to *WT*: *p<0.05; reference genes *Tuba1b* and *Ubb*.

Table 3.4) qRT-PCR Expression in P21 mouse retinas

		Fold change to *WT*				
Gene	^Overall p-value (heterozygous mice)	*E168d2/+*	*E168d2neo/+*	*R90W/+*	*R90Wneo/+*	*+/-*
Rho	0.023	0.41*	0.72	0.86	1.08	1.18
Arr3	0.010	0.36*	0.38*	0.88	0.77*	0.91
Opn1sw	0.044	0.37*	0.32*	0.64	0.72*	0.60*
Opn1mw	0.007	0.22*	0.43*	1.05	0.89	0.96
Dnaic1	0.015	0.20*	0.26*	0.79	0.79*	0.67*
Myo7a	0.017	0.51*	0.34*	0.85	1.04	1.07
Crx	0.008	3.28*	1.70*	1.22	0.7	1.05
Otx2	0.138	1.79	1.07	1.60	1.56	1.80
Crxos1	0.311	0.61	0.49	0.93	0.85	0.89
Nrl	0.609	1.02	0.83	0.73	0.96	1.07
Nr2e3	0.600	1.45	1.54	1.39	1.13	1.01
Rxry	0.503	1.17	1.33	1.11	1.16	1.1
Thrb	0.055	0.8	0.66*	0.31	1.13	0.79
Pias3	0.847	0.75	0.83	0.94	1.27	1.08

^Overall p-value for each primer set was tested in heterozygous; p<0.09 was considered marginally significant

*p<0.05; reference genes Tuba1b and Ubb

Table 3.4) qRT-PCR Expression in P21 mouse retinas. ^Overall p-value for each primer set was tested in heterozygous; p<0.09 was considered marginally significant. For all comparisons to *WT*: *p<0.05; reference genes *Tuba1b* and *Ubb*.

Fig 3.1)

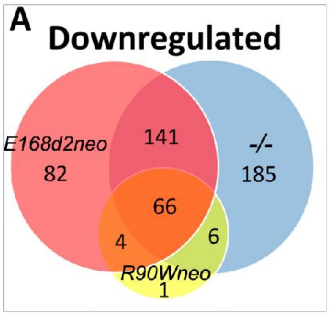

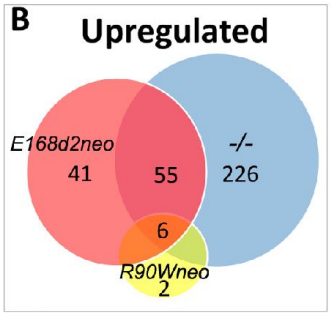

C

Percentage of Genes bound by WT CRX				
	Downregulated		Upregulated	
	WT retinas	*Nrl KO* retinas	*WT* retinas	*Nrl KO* retinas
E168d2neo	76.8	61.3	46.7	55.0
R90Wneo	83.0	62.8	41.7	41.7
-/-	68.8	53.6	40.7	50.5
Shared	84.4	60.9	66.7	66.7

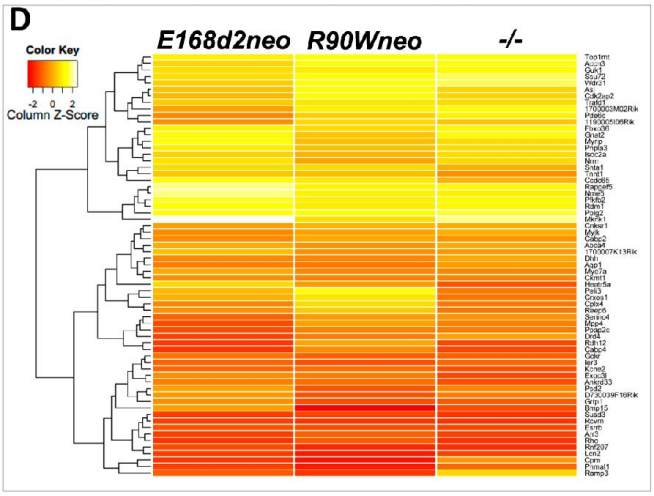

E

Cellular Processes of Downregulated Genes
Phototransduction/Visual cycle
Abca4, Arr3, Gnat2, Pde6c, Rcvrn, Rdh12, Rho
Aipl1, Gnat1, Guca1b, Opn1mw, Pde6a, Pde6g, Ppef2, Rgs9bp, Rpgrip1, Rtbdn, Sag, Tulp1
Metabolism, Mitochondrial function
Asl, Ckmt1, Gckr, Guk1, Ier3, Isoc2a, Nme5, Pfkfb2, Pnpla3,Ppap2c, Top1mt
Abcg4, Acadvl, Akap1, Asrgl1, Avpi1, B4galt1, Cds1, Mrpl49, Neu4, Nos3, Pdia5, Pgc, Pmm1, Ppargc1b, Rbks, Rhot2, Stard7, Timm44, Zdhhc12
Membrane Stability/function
Ankrd33, Cpm, Nrm, Reep6, Serinc4, Snta1, Susd3
Chst12, Impg1, Lrfn2, Prph2, Slc16a6, Slc24a1, Slc25a10, Slc25a35, Slc38a3, Slc5a5, Slco4a1, Spg7, Vtn
Synaptic function
Cplx4, Drd4, Mpp4, Psd2
Als2, Cacna1f, Gng8, Igsf9, Prrt1, Syngr1
Intercellular transport
Exoc3l, Heatr5a, Lcn2, Mylk, Myo7a, Myrip, Tnnt1
Actb, Dnaic1, Dynlrb2, Osbp2, Spire2
Transcription/translation
Crxos1, Esrrb, Polg2, Rdm1, Ssu72
Cables2, Dpf3, Gtf3a, Hemk1, Hmgn1, Icmt, Plagl2, Tdrd7, Thoc5, Tob2, Vsx1
Color Key:
Down in *E168d2neo, R90Wneo, -/-*
Down in *E168d2neo* and *-/-* only

Chapter III

Figure 3.1) Graded changes in retinal gene expression in homozygous *E168d2*, *R90W* and *-/-* mice. **A-B**) Venn diagram showing genes differentially expressed at P10 as identified by Illumina gene expression mouseRef6 microarray. *E168d2neo/d2neo*, *R90Wneo/Wneo* and *-/-* mice show a high degree of overlap in differentially expressed genes. **C**) Percentages of differentially expressed genes found to be directly bound by WT CRX protein in *WT* and *Nrl KO* retinas by ChIP-Seq, showing association of differentially expressed genes with direct CRX targets. **D**) Heat map of commonly downregulated genes in *E168d2neo/d2neo*, *R90Wneo/Wneo* and -/- mice show graded changes in gene expression of commonly downregulated genes. **E**) Cellular processes associated with commonly downregulated genes, based on gene ontology provided by Mouse Genome Informatics, showing a widespread effect of *Crx* mutations on visual and cellular pathways.

Fig 3.2)

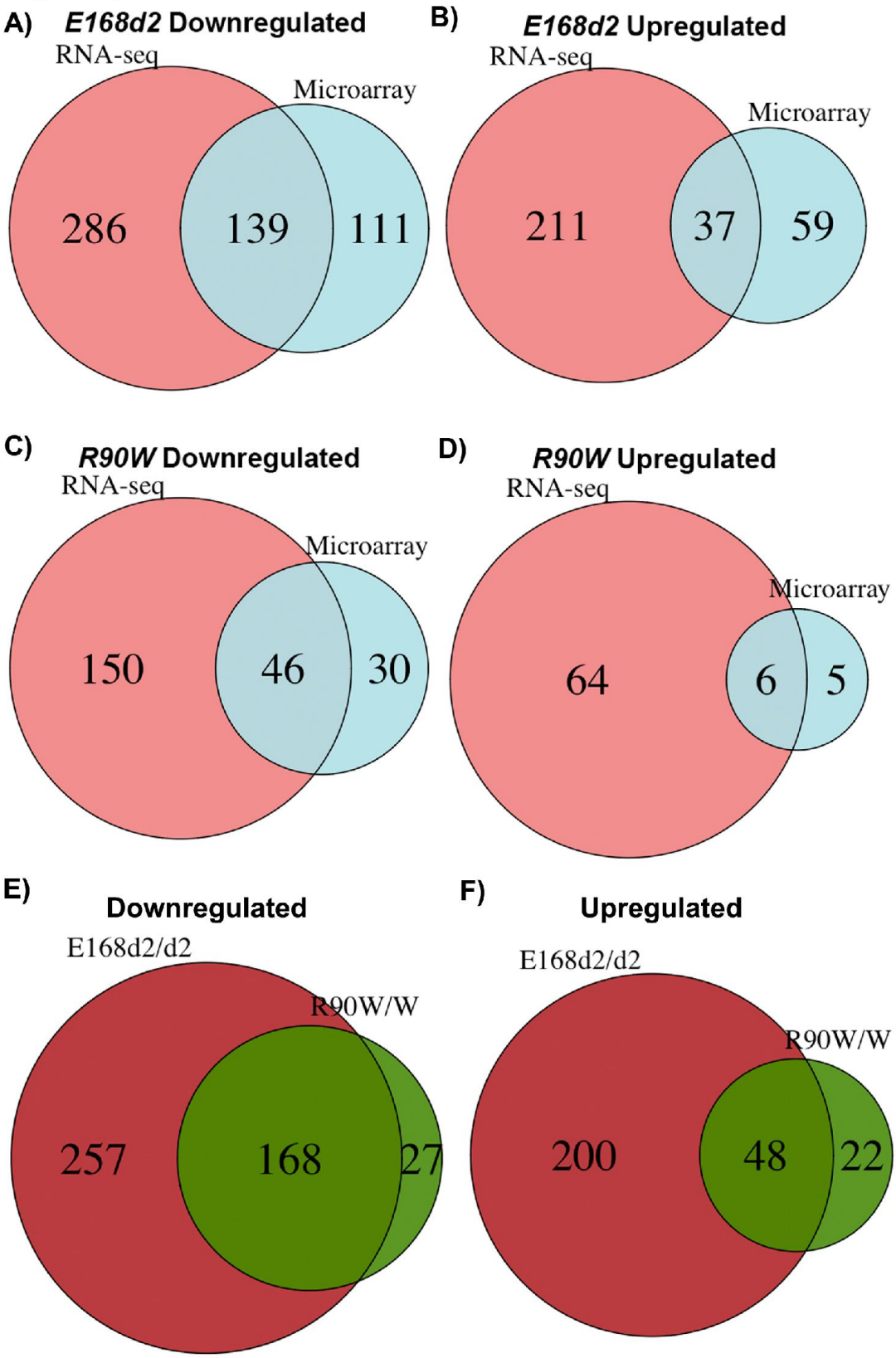
A)
E168d2 Downregulated
RNA-seq
Microarray
286
139
111
B)
E168d2 Upregulated
RNA-seq
Microarray
211
37
59
C)
R90W Downregulated
RNA-seq
Microarray
150
46
30
D)
R90W Upregulated
RNA-seq
Microarray
64
6
5
E)
Downregulated
E168d2/d2
R90W/W
257
168
27
F)
Upregulated
E168d2/d2
R90W/W
200
48
22

Figure 3.2) Venn diagrams showing the overlap of differentially expressed genes determined by microarray and by RNA-Seq. Venn diagram of showing the number of genes >2-fold differentially expressed in RNA-Seq and Microarray experiments in A-B) P10 *E168d2/d2*, C-D) P10 *R90W/W*. Venn diagram of showing the number of genes >2-fold differentially expressed in RNA-Seq in E-F) *E168d2/d2* and *R90W/W* mouse retinas.

Fig 3.3)

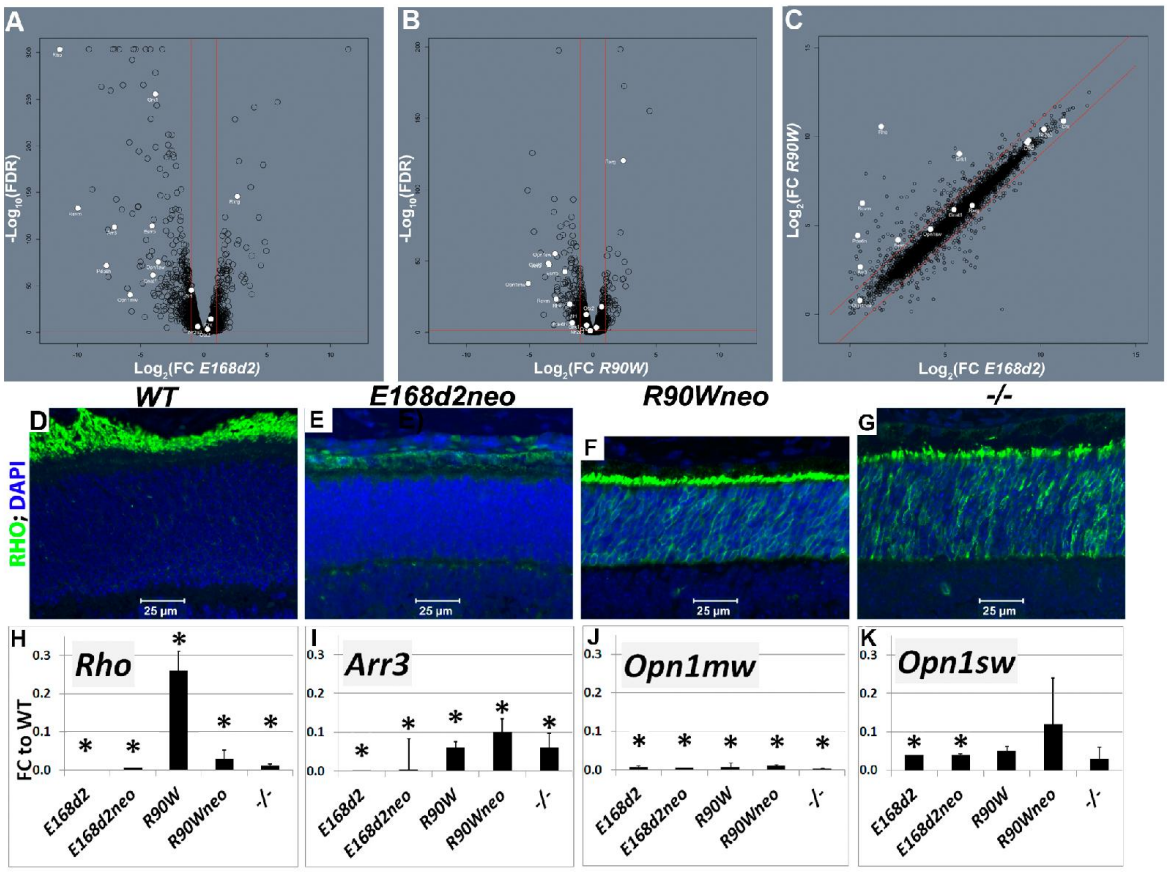
A
B
C
-Log10(FDR)
Log2(FC E168d2)
Log2(FC R90W)
Log2(FC R90W)
Log2(FC E168d2)
WT
E168d2neo
R90Wneo
-/-
D
E
F
G
RHO; DAPI
25 µm
H
I
J
K
Rho
Arr3
Opn1mw
Opn1sw
FC to WT
E168d2
E168d2neo
R90W
R90Wneo
-/-

Figure 3.3) Expression pattern in homozygous *E168d2* and *R90W* mice. A-B) Volcano plots showing the distribution of gene expression in P10 *E168d2/d2* (A) and *R90W/W* (B) mouse retinas by RNA-Seq. Log_2 fold-change (FC) is plotted against the strength of significance as determined by the $-log_{10}$ False discovery rate (FDR). Genes above the horizontal red line are significantly differentially expressed in the indicated genotype, compared to *WT.* Genes to the left of the left-most vertical red line are downregulated and genes to the right of the right-most vertical red line are upregulated compared to *WT*. 12 genes with kown function in rods/cones were labels in white to illustrate the patterns on gene expression. C) Scatter plots of the Log_2 fold-change (FC) to *WT* of *E168d2*/d2 vs. *R90W/W* at P10. Genes above the top red line are expressed >2-fold higher in the genotye indicated on the veritcal axis. Genes below the bottom red line are expressed >2-fold higher in the genotype indicated on the horizontal axis. D-G) P14 paraffin embedded sagittal retinal sections of *E168d2/d2, R90W/W and -/-* mice were stained with Rhodopsin (RHO, green) and DAPI (blue), and imaged by wide field fluorescence at 40x. Note that RHO is absent in *E168d2/d2*, while mislocalized to ONL in *R90W/W* and *-/-*. H-K) Validation of microarray results by qRT-PCR analyses on selected CRX target genes, *Rho, Arr3, Opn1mw* and *Opn1sw* in retinas of the indicated mouse strains at P10 shown as FC relative to *WT*. (*p<0.05; Error bars: STDEV).

Fig 3.4)

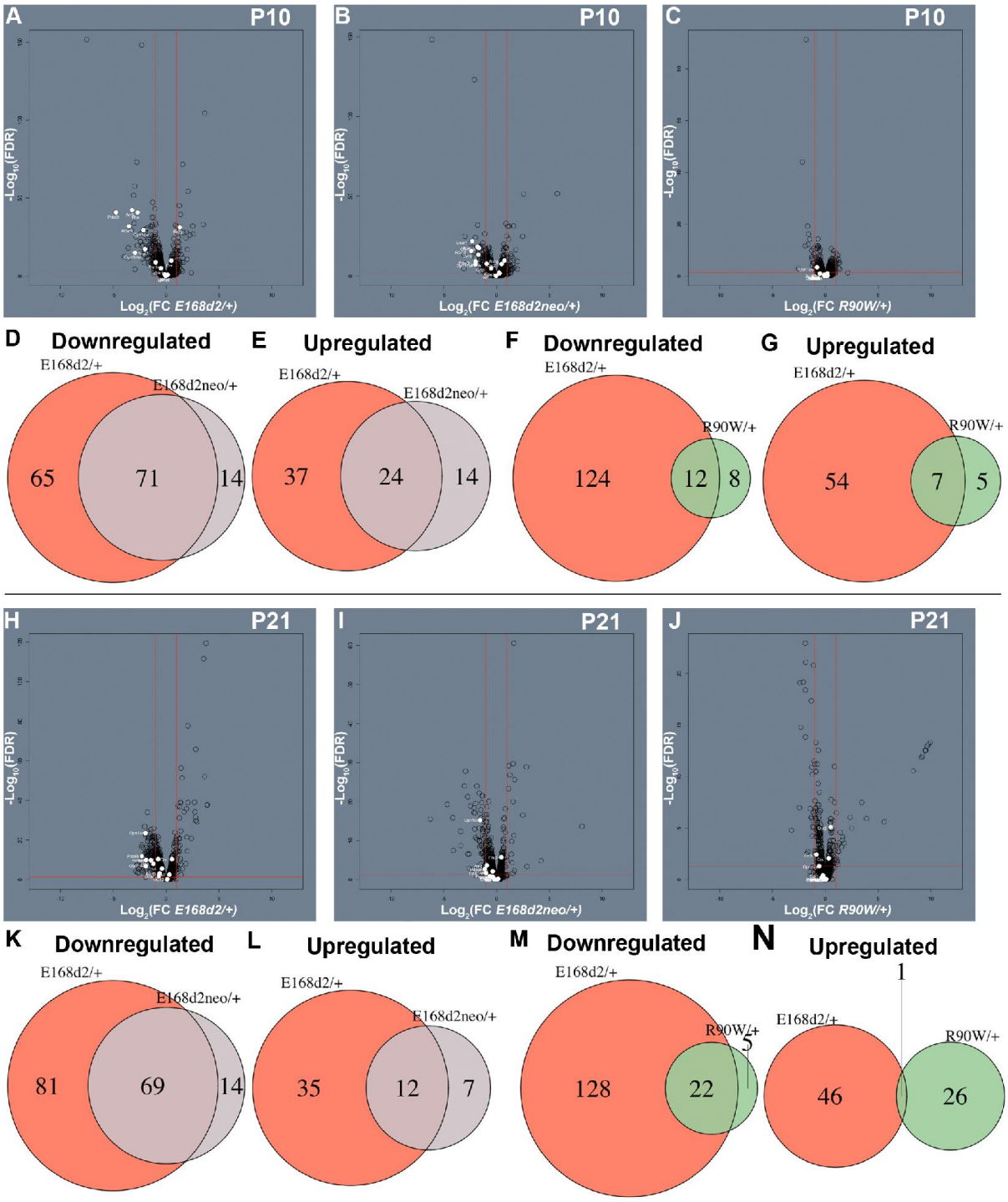
A
P10
-Log10(FDR)
Log2(FC E168d2/+)
B
P10
-Log10(FDR)
Log2(FC E168d2neo/+)
C
P10
-Log10(FDR)
Log2(FC R90W/+)
D
Downregulated
E168d2/+
E168d2neo/+
65
71
14
E
Upregulated
E168d2/+
E168d2neo/+
37
24
14
F
Downregulated
E168d2/+
R90W/+
124
12
8
G
Upregulated
E168d2/+
R90W/+
54
7
5
H
P21
-Log10(FDR)
Log2(FC E168d2/+)
I
P21
-Log10(FDR)
Log2(FC E168d2neo/+)
J
P21
-Log10(FDR)
Log2(FC R90W/+)
K
Downregulated
E168d2/+
E168d2neo/+
81
69
14
L
Upregulated
E168d2/+
E168d2neo/+
35
12
7
M
Downregulated
E168d2/+
R90W/+
128
22
5
N
Upregulated
1
E168d2/+
R90W/+
46
26

Figure 3.4) Expression patterns in heterozygous *E168d2* and *R90W* mice. A-B) Volcano plots showing the distribution of gene expression in P10 *E168d2*/+ (A) and *R90W*/+ (B) mouse retinas by RNA-Seq. Log_2 fold-change (FC) is plotted against the strength of significance as determined by the $-log_{10}$ False discovery rate (FDR). Genes above the horizontal red line are significantly differentially expressed in the indicated genotype, compared to *WT.* Genes to the left of the left-most vertical red line are downregulated and genes to the right of the right-most vertical red line are upregulated compared to *WT*. 12 genes with known function in rods/cones were labeled in white to illustrate patterns in gene expression. D-E) Venn diagrams showing the number of genes >2-fold differentially expressed in P10 *E168d2/+* vs. *E168d2neo/+* and F-G) *E168d2/+* vs. *R90W/+* mouse retinas. H-J) Volcano plots showing the fold change and significance by FDR for all genes in P21 *E168d2/+* (H), *E168d2neo/+* (I) and *R90W/+* (J) mouse retinas. 12 genes with known function in rods/cones were labeled in white to illustrate patterns in gene expression. K-L) Venn diagrams showing the number of genes >2-fold differentially expressed in P21 *E168d2/+* vs. *E168d2neo/+* and M-N) *E168d2/+* vs. *R90W/+* mouse retinas.

Fig 3.5)

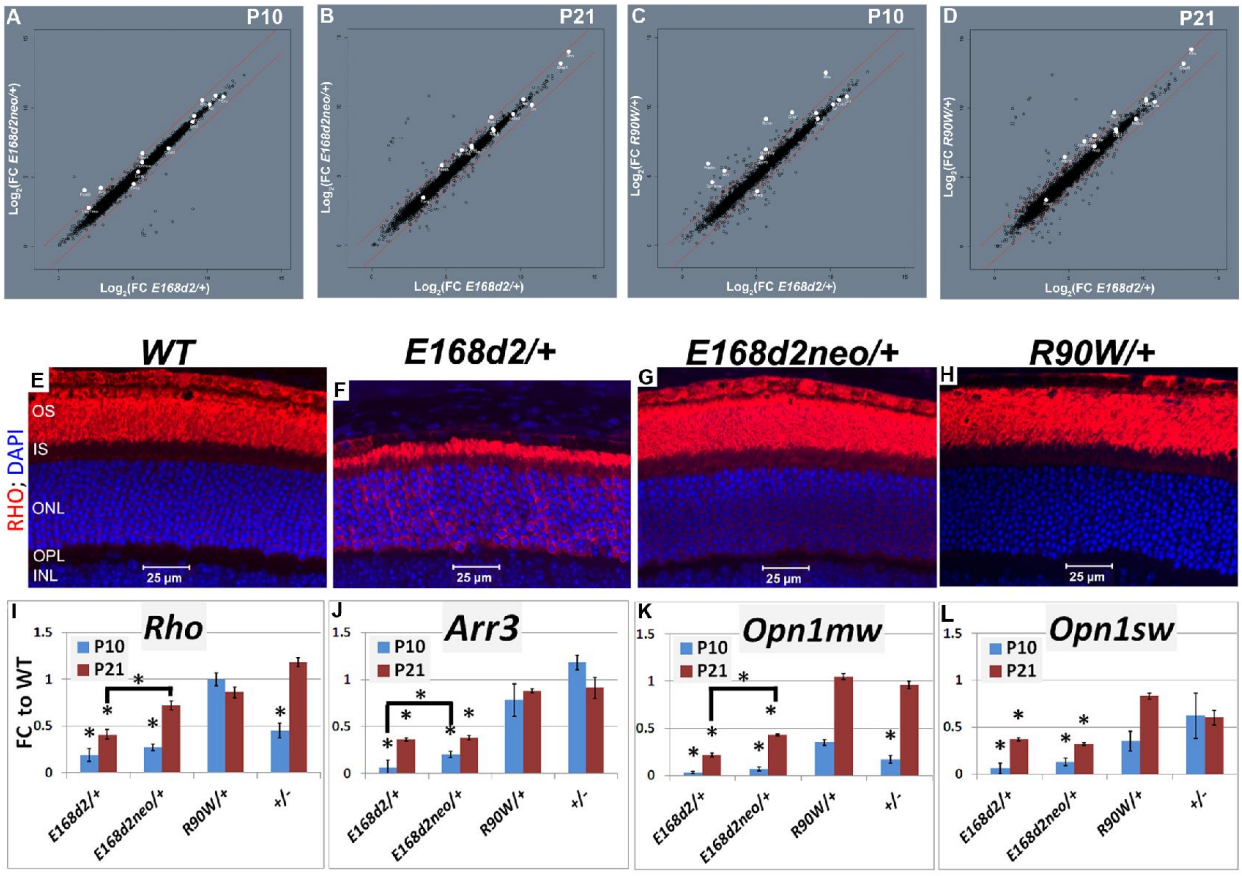
A
P10
B
P21
C
P10
D
P21
WT
E168d2/+
E168d2neo/+
R90W/+
E
F
G
H
OS
IS
ONL
OPL
INL
RHO; DAPI
25 µm
I
Rho
J
Arr3
K
Opn1mw
L
Opn1sw
FC to WT
P10
P21
E168d2/+
E168d2neo/+
R90W/+
+/-

Figure 3.5) Retinal gene expression in heterozygous *E168d2*, *E168d2neo* and *R90W* mouse retinas. A-D) Scatter plots of the Log_2 fold-change (FC) to *WT* of *E168d2*/+ vs. *E168d2neo*/+ at P10 (A) and P21 (B) and of *E168d2*/+ vs. *R90W*/+ at P10 (C) and P21 (D). Genes above the top red line are expressed >2-fold higher in the genotye indicated on the veritcal axis. Genes below the bottom red line are expressed >2-fold higher in the genotype indicated on the horizontal axis. E-H) Paraffin embedded sagittal retinal sections of 1mo WT and the indicated heterozygous mutant mice were stained with mouse monoclonal anti-Rhodopsin RetP-1 antibody (Chemicon) (RHO, red) and DAPI nuclear conterstaining (blue), and imaged by widefield fluorescence at 40x. Scale bars 25μM. *E168d2*/+ shows reduced RHO staining intensity in rod OS's and mislocalized RHO in ONL. I-L) qRT-PCR analysis of four CRX target genes, *Rho*, *Arr3*, *Opn1mw*, *Opn1sw* in the indicated heterozygous mice at P10 and P21 (*p<0.05; bracketed *FDR p<0.09; Error bars: SEM).

Fig 3.6)

A

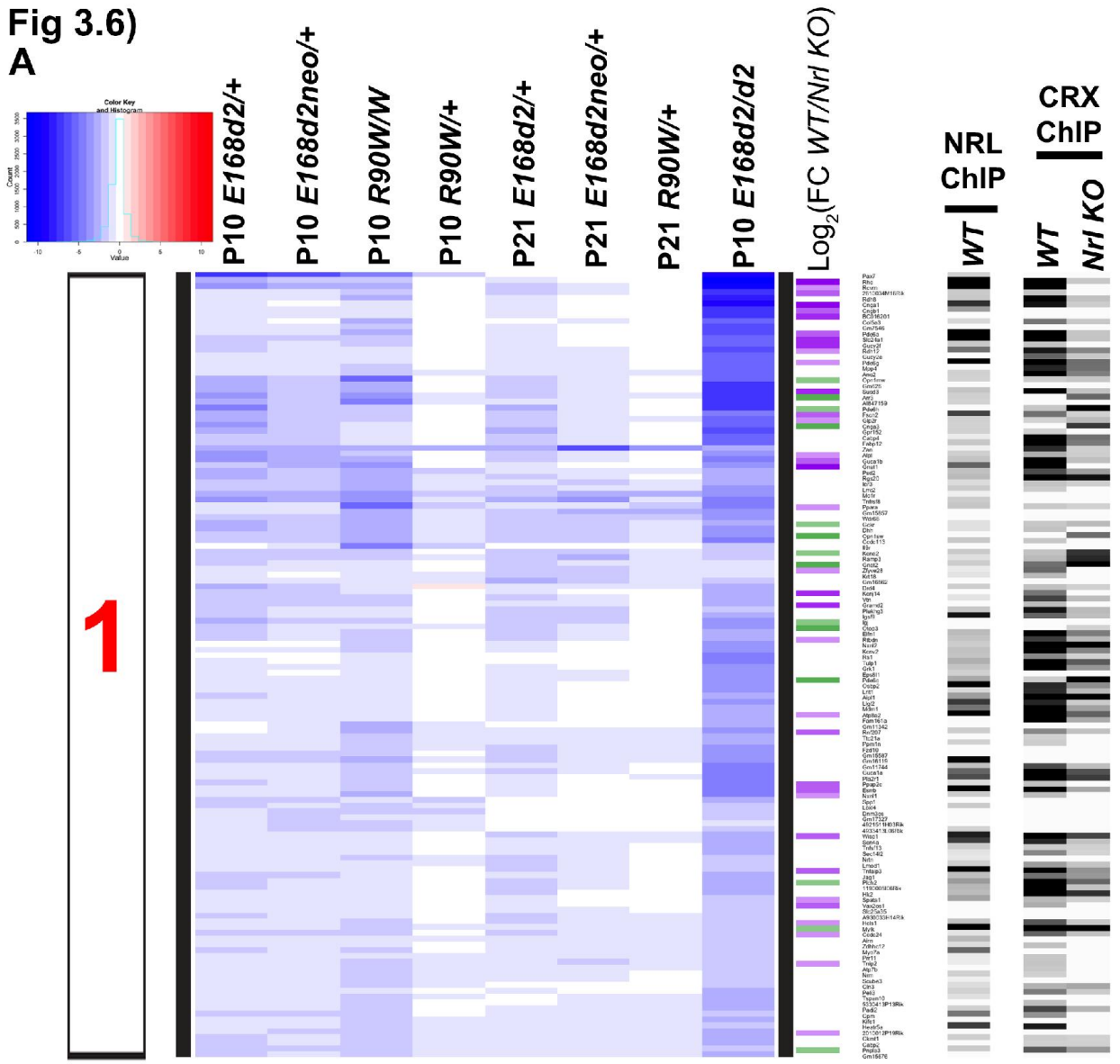

B

G:Profiler Pathway Analysis

P-value	Pathway	Pathway name	Genes in Pathway
1.97E-29	GO:0007601	visual perception	MYO7A,GUCA1A,GM11744,PDE6C,GRK1,TULP1,RS1,GNAT2,OPN1SW,GNAT1,GUCA1B,CNGA3,PDE6H,ARR3,OPN1MW,PDE6G,GUCY2E,RDH12,GUCY2F,PDE6A,CNGA1,RDH8,RCVRN,RHO
2.44E-21	GO:0007602	phototransduction	GUCA1A,AIPL1,PDE6C,GRK1,TULP1,RS1,GNAT2,OPN1SW,GNAT1,GUCA1B,OPN1MW,BC016201,RCVRN,RHO
7.07E-13	GO:0001750	photoreceptor outer segment	GUCA1A,TULP1,GNAT2,OPN1SW,GNAT1,GUCA1B,CNGA3,ARR3,OPN1MW,CNGA1,RHO
7.01E-07	GO:0060041	retina development in camera-type eye	MDM1,PDE6C,GRK1,TULP1,RS1,GNAT2,GNAT1,CNGA3,PDE6A,RHO
1.67E-05	GO:0030553	cGMP binding	PDE6C,CNGA3,PDE6H,PDE6G,CNGA1
5.73E-04	GO:0009881	photoreceptor activity	TULP1,OPN1SW,OPN1MW,RHO
8.24E-04	GO:0047555	3',5'-cyclic-GMP phosphodiesterase activity	PDE6C,PDE6H,PDE6G,PDE6A
1.09E-03	GO:0016020	membrane	PNPLA3,CKMT1,CPM,TSPAN10,CLN3,NRM,ATP7B,MYO7A,ZDHHC12,MYLK,HCLS1,SLC25A35,HK2,PLCH2,JAG1,SEC14L2,TNFSF13,SCN4A,LOXL4,NXNL1,PPAP2C,PLA2R1,GUCA1A,GM11744,FZD10,ATP8A2,LRIT1,OSBP2,PDE6C,GRK1,TULP1,RS1,KCNV2,ELFN1,OTOP3,IGSF9,GRAMD2,KCNJ14,DRD4,ZFYVE28,GNAT2,RAMP3,KCNE2,IL9R,OPN1SW,DHH,TNFRSF8,MC1R,IER3,RGS20,PSD2,GNAT1,GUCA1B,ALPL,ZAN,CNGA3,GLP2R,SUSD3,OPN1MW,ANO2,MPP4,GUCY2E,GUCY2F,SLC24A1,PDE6A,BC016201,CNGA1,RHO
6.01E-03	GO:0046058	cGMP metabolic process	GUCA1A,AIPL1,GUCA1B,GUCY2E,GUCY2F
1.34E-02	GO:0005223	intracellular cGMP activated cation channel activity	CNGA3,BC016201,CNGA1
1.53E-02	GO:0006796	phosphate-containing compound metabolic process	CKMT1,CLN3,ATP7B,MYLK,HCLS1,HK2,PLCH2,TNFAIP3,PPAP2C,GUCA1A,FZD10,AIPL1,GRK1,ELFN1,VTN,DRD4,ZFYVE28,GNAT2,GCKR,MC1R,GNAT1,GUCA1B,ALPL,PDE6H,ARR3,PDE6G,GUCY2E,GUCY2F,PDE6A,RHO
3.92E-02	GO:0018298	protein-chromophore linkage	OPN1SW,OPN1MW,RHO
4.97E-02	GO:0008048	calcium sensitive guanylate cyclase activator activity	GUCA1A,GUCA1B

C

CSEA Results

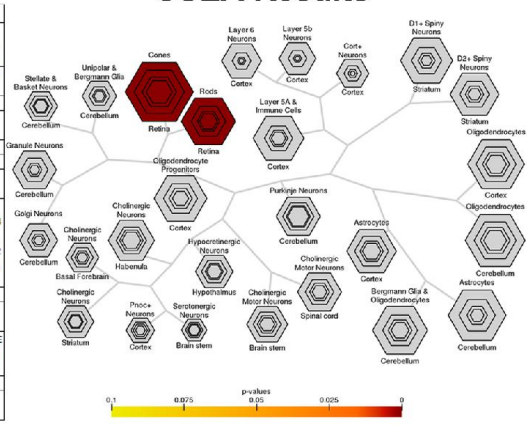

Figure 3.6) Patterns in Group 1 genes in *E168d2* and *R90W* retinas. A) Hierarchical cluster analysis of gene expression in P10 and P21 *E168d2* and *R90W* mouse retinas. Log_2 fold-change (FC) to *WT* is shown in a graded color heat map with blue being downregulated and red being upregulated (upper left). Genotypes and ages are shown for each column and gene symbols are listed for each row. Gene subsets were selected based on overall expression patterns among genotypes. Group 1 showed the most downregulated expression among differentially expressed genes. Heatmaps were paired with RNA-Seq expression in P21 *Nrl KO* mouse retinas. Genes downregulated in *Nrl KO* are shown in purple and upregulated in green. Enrichment of DNA-binding for each genes by NRL in P21 *WT* mouse retinas and CRX in *WT* and *Nrl KO* mouse retinas as determined by ChIP-Seq are shown with black being the highest enrichment. B) G:profiler pathway analysis showing cellular pathways (GO processes) that are significantly associated with genes in Group 1. The Pvalue, GO process ID, Pathway name and the genes in Group 1 associated with each GO process are listed. C) Cell specific expression analysis (CSEA) results showing the cell-type specific expression in *WT* mouse retinas for genes in Group 1. Colored hexagons indicate cell-types that have been associated with the specific expression of queried genes, darker colors indicate higher significance. Hexagon rings indicate the specificity of gene expression with genes belonging to the inner-most rings associated with the most cell-type specific gene expression and outer-most rings associated with the least specific expression.

Fig 3.7)

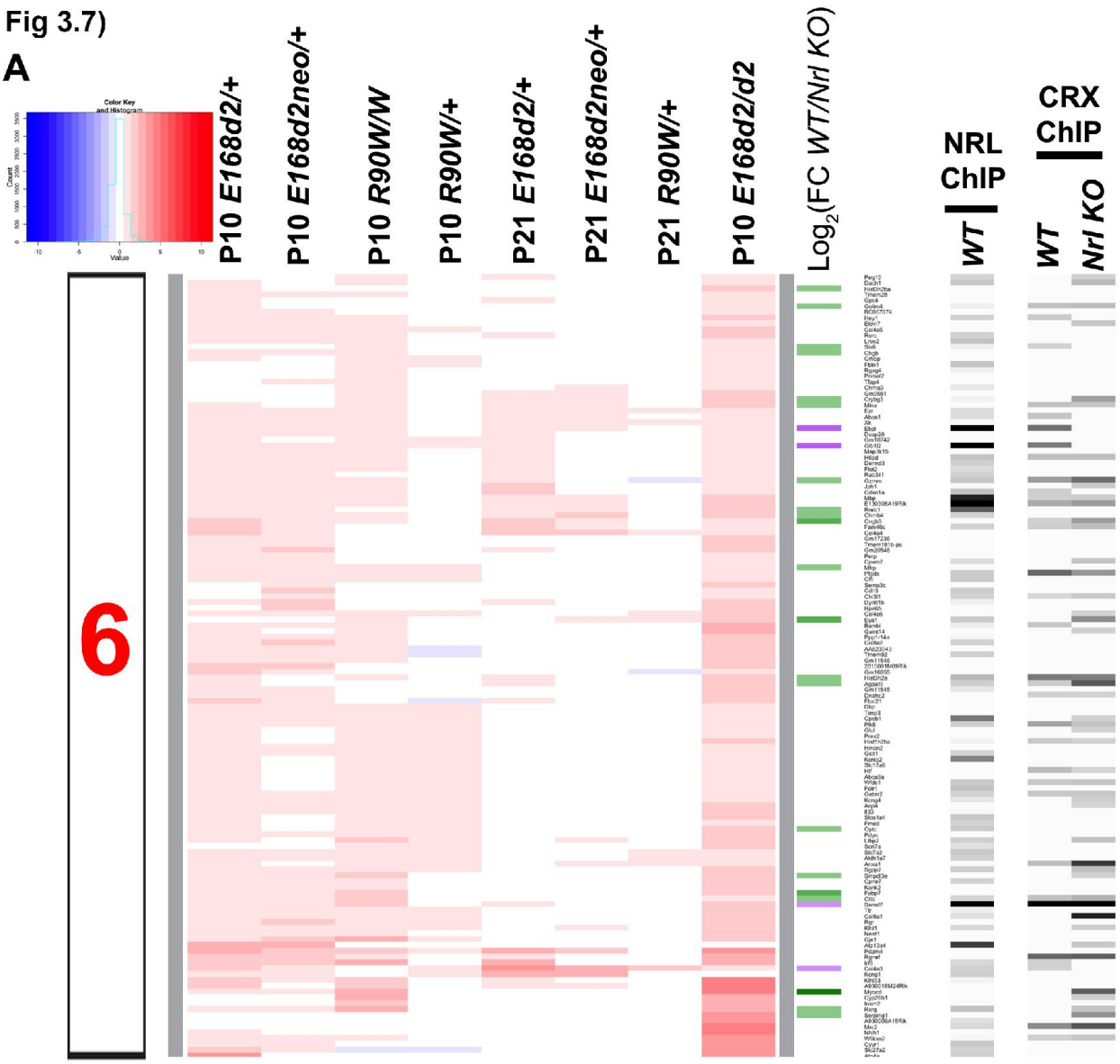

B

G:Profiler Pathway Analysis

P-value	Pathway	Pathway name	Genes in Pathway
2.29E-02	GO:0006811	ion transport	ATP4A,SLC27A2,KCNG1,ATP13A4,ANXA1,SLC7A2,SCN7A,SLCO1A4,KCNG4,GABRR2,FOLR1,SLC17A8,KCNIP2,CNGB3,CHRNB4,XK,ABCA1,CHRNA3,CRHBP
3.98E-06	GO:0005604	basement membrane	COL4A3,COL8A1,HMCN2,TIMP3,COL9A2,COL4A6,COL4A4,FBLN1,COL4A5
3.81E-03	GO:0005215	transporter activity	ATP4A,SLC27A2,KCNG1,ATP13A4,FABP7,SLC7A2,SCN7A,SLCO1A4,AQP4,KCNG4,GABRR2,FOLR1,SLC17A8,KCNIP2,PTGDS,CNGB3,CHRNB4,ABCA1,CHRNA3

C

CSEA Results

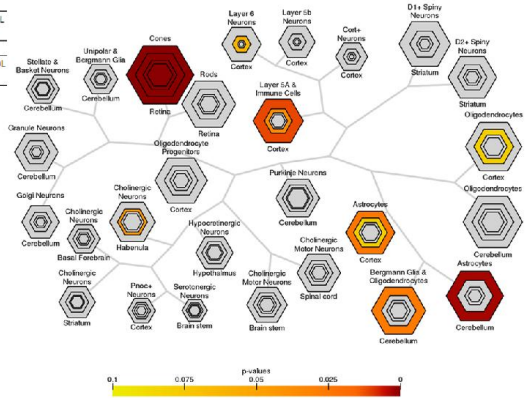

Figure 3.7) Patterns in Group 6 genes in *E168d2* and *R90W* retinas. A) Hierarchical cluster analysis of gene expression in P10 and P21 *E168d2* and *R90W* mouse retinas. Log_2 fold-change (FC) to *WT* is shown in a graded color heat map with blue being downregulated and red being upregulated (upper left). Genotypes and ages are shown for each column and gene symbols are listed for each row. Gene subsets were selected based on overall expression patterns among genotypes. Group 6 showed the most upregulated expression among differentially expressed genes. Heatmaps were paired with RNA-Seq expression in P21 *Nrl KO* mouse retinas. Genes downregulated in *Nrl KO* are shown in purple and upregulated in green. Enrichment of DNA-binding for each genes by NRL in P21 *WT* mouse retinas and CRX in *WT* and *Nrl KO* mouse retinas as determined by ChIP-Seq are shown with black being the highest enrichment. B) G:profiler pathway analysis showing cellular pathways (GO processes) that are significantly associated with genes in Group 6. The Pvalue, GO process ID, Pathway name and the genes in Group 6 associated with each GO process are listed. C) Cell specific expression analysis (CSEA) results showing the cell-type specific expression in *WT* mouse retinas for genes in Group 6. Colored hexagons indicate cell-types that have been associated with the specific expression of queried genes, darker colors indicate higher significance. Hexagon rings indicate the specificity of gene expression with genes belonging to the inner-most rings associated with the most cell-type specific gene expression and outer-most rings associated with the least specific expression.

Chapter IV

-

Mechanisms of Overexpression of Truncated CRX Proteins

Author: Nicholas Tran

Experiments utilizing the *Crx*^{RDY} feline model were performed and analyzed by Laurence Ocelli (Simon Peterson-Jones lab, Michigan State University) and Nicholas Tran. All other work was performed and analyzed by Nicholas Tran.

Chapter IV

Introduction- Allele-specific overexpression of *CRX* truncation mutations

E168d2 mice express abnormally high levels of both mutant mRNA and its protein product. We predicted that overexpression was related to the intrinsic properties of *E168d2* mRNA, driven either by transcription efficiency or post-transcription mRNA stability. Since a previous study of human *CRX* mutants in *Drosophila* shows that another frameshift mutation $I138^{fs48}$ is overly stable[1], we also wanted to examine whether allelic expression imbalance may be a general characteristic of frameshift CRX mutations. For this reason we sought to investigate if mutant *Crx* overexpression is conserved by investigating the expression of *Crx* in a feline model of *CRX* retinopathy, Crx^{Rdy}, which carries a similar type frameshift mutation as *E168d2*. We also examined mutations *in vitro* to determine if overexpression is a common feature of human disease-causing mutations from this class. Additionally, we investigated the mechanism of *E168d2* overexpression by assessing in the post-transcriptional stability of the mutant transcript both *in vitro* and *ex vivo*.

While frameshift mutations that generate early stop codons can lead to transcript degradation in a well-characterized process called nonsense-mediated mRNA decay (NMD)[2], there is little previous evidence of these types of mutations causing transcript over-stability. Therefore, allele-specific overexpression of *Crx* transcripts may indicate not only a novel mechanism of disease but may be interesting biologically.

Chapter IV

Results

4.1. Allelic expression levels of mouse, feline and human CRX mutants

4.1.i) Phenotype and expression of Crx mRNA and protein in the feline disease model, Crx^{Rdy}

The Crx^{Rdy} cat carries the frameshift mutation *Crx n.546delC* and is associated with dominant and progressive retinopathy characteristic of LCA[3–7]. *Crx n.546delC* results in the introduction of an early stop-codon and was predicted to lead to the expression of a truncated CRX protein that was only 14 amino acids longer than $CRX^{[E168d2]}$. Assessment of cone and rod morphology in heterozygous Crx^{Rdy} cats at 6wk by immunofluorescent staining of sagittal retinal sections with mCARR and Rho antibodies reveals striking similarity to the *CrxE168d2* mouse phenotype at 1mo (Fig 4.1A-H). 6wk heterozygous Crx^{Rdy} cats have noticeably fewer mCARR positive cells compared to *WT* (Fig 4.1D vs. C). While the ONL maintains normal thickness through 6wk, rod outer segments are shortened and Rhodopsin is mislocalized to the nucleus/cell body (Fig 4.1H vs. G). The morphology of Crx^{Rdy} cones and rods suggest that, similar to *E168d2* mice, both photoreceptor types are affected and cone loss occurs earlier and is more severe. Thus, the Crx^{Rdy} cat model closely resembles the phenotype of *E168d2* mice, indicating it is a well-matched large animal model.

The expression of CRX protein was assessed by Western blot at P1, P14, 6wk, 12wk and 20wks in *WT* and Crx^{Rdy} cats (Fig 4.1I). Crx^{Rdy} cats express both WT and a truncated mutant CRX at all ages (Fig 4.1I). Similar to *E168d2* mice, the truncated mutant CRX protein in Crx^{Rdy} cats is expressed at higher levels than the full-length WT CRX protein. By 20wks of age, the expression of WT CRX is barely detectable, while expression of the truncated protein is still robust. The expression level of *Crx* mRNA was determined by qRT-PCR at P14, 6wk and 20wk in WT and heterozygous Crx^{Rdy} cats (Fig 4.1J). The expression of total *Crx* mRNA was

measured since we were unable to design allele-specific qRT-PCR primers, as we did for *E168d2* and *R90W* mice (Fig 2.2J). Total *Crx* was overexpressed by ~2-fold in heterozygous Crx^{Rdy} cats compared to *WT* cats at each time point by (Fig 4.1J). This is similar to the level of total *Crx* in heterozygous *E168d2/+* mice. Collectively, these results show that both *E168d2* mice and Crx^{Rdy} cats have allele-specific overexpression of mutant *Crx* mRNA and protein, suggesting that this characteristic is conserved between the two animal models.

4.1.ii. Mouse, human and cat truncating Crx mutations are overexpressed in vitro

To test if other truncating mutations are also overexpressed, we assessed their expression *in vitro* by Western blot and qRT-PCR. First, however, it was necessary to determine whether *E168d2* and *Rdy* expression *in vitro* recapitulated expression patterns observed *in vivo* in the mouse and cat models. Mouse and human *Crx WT*, *E168d2* and *R90W* and cat *Crx WT* and *Rdy* were each cloned into the pCAGIG plasmid, in which expression is driven by the pCAG promoter and co-expresses Gfp from an internal ribosomal entry site. Equal concentrations of each plasmid were independently transfected into HEK 293 cells, cultured for 48hrs and nuclear protein was collected for Western blot experiments. Similar to the pattern in *E168d2* and *R90W* mouse retinas, E168d2 protein level was elevated and R90W protein level was reduced, compared to WT *in vitro* (Fig 4.2A). The cat CRX Rdy protein was also elevated compared to cat WT *in vitro*, similar to mutant expression in Crx^{Rdy} cats (Fig 4.2B). Since E168d2 and Rdy proteins were overexpressed even when expression was driven by a common promoter *in vitro*, it suggest that *in vitro* transfection accurately recapitulated *in vivo* expression patterns and is a valid method for assessing the expression patterns of *Crx* mutants. Subsequently, the expression of human CRX E168d2 and R90W were tested. Similar to mouse E168d2 and R90W proteins, E168d2 protein was elevated and R90W was reduced compared to

WT level *in vitro* (Fig 4.2C), suggesting expression patterns were conserved between mouse and human mutants. Finally, early stop codons were cloned into an Xpress tagged human *CRX* gene at the amino acids number 107, 160, 168, 208 and 254 (Fig 4.2D) and the expression levels of their mRNA and protein were tested. These constructs encode the full-length human *CRX* transcript but result in the translation of a truncated CRX protein, comparable to frameshift truncation mutations. Plasmids were designated as 'U constructs' since they represent truncation mutations that convert portions of *CRX's* coding region into a novel 3' UTR. Each of the truncated U constructs tested expressed mutant *CRX* at significantly higher levels compared to *WT* (Fig 4.2E). The U constructs U160, U168 and U208 also expressed protein at higher levels compared to WT (Fig 4.2F). The constructs U107 and U254 did not overexpress *CRX* protein, despite overexpressing *CRX* mRNA (Fig 4.2F vs. E), this suggests that the stability of U107 and U254 proteins may have been compromised. These results require further confirmation since they were performed in individual transfections making it impossible to control for variations in transfection efficiencies. Experiments are being designed to test expression of multiple constructs co-transfected into a single population of cells, which should improve the reliable of results. Collectively, these results support our hypothesis that mutant CRX overexpression is a common characteristic among several truncating mutations and is conserved between mouse, cat and human *CRX*.

4.2. Assessment of the stability of *WT* and mutant *Crx* mRNA

To determine if mRNA stability was a mechanism for the overexpression of *E168d2*, we measured the degradation of *Crx* transcripts *in vitro* and *in vivo* over time. To control for potential inconsistencies among transfection experiments, unique 10bp barcodes were inserted into the 3' tail of human *Crx WT* and *E168d2* constructs (Fig 4.3A) to allow for the analysis of

transcripts from co-transfected plasmids by qRT-PCR. To control for the possibility that barcodes affected mRNA expression or stability, *CRX WT* was tagged with 4 unique barcodes and *E168d2* was tagged with 2 bar codes (Table 4.1) and the combined results were analyzed. *CRX WT* and *E168d2* constructs tagged distinct barcodes were co-transfected in pairs into HEK 293 cells. After 48hrs, transfected cells were treated with Actinomycin D, which blocks mRNA transcription[8–11] and incubated then harvested at 4hrs or 8hrs. mRNA was collected and the expression of *CRX* mRNA was determined by qRT-PCR, results were normalized to the expression level at time 0hrs. Fig 4.3B shows that *WT CRX* mRNA transcripts were degraded by ~30% at 4hrs and ~42% at 8hrs, while *E168d2* only degraded by ~4% at 4hrs and ~17% at 8hrs. Thus, *E168d2* transcripts degraded more slowly than *WT CRX* suggesting that *E168d2* transcripts may be more stable that *WT* transcripts. The stability of *CRX WT, E168d2* and *R90W* mRNA was also tested *ex vivo* by treating explanted P10 retinas from *WT* and homozygous *E168d2/d2* and *R90W/W* mice with Actinomycin D. *Crx WT* and *R90W* showed comparable degredation at 4hrs (*WT* ~43%, *R90W* ~57%) and 8hrs (*WT* ~70%, *R90W* ~65%) (Fig 4.3C). In contrast, *E168d2* transcripts were less degraded at 4hrs (~30%) and 8hrs (~30%) (Fig 4.3C), suggesting that *E168d2* transcripts degrade at a slower rate than either *Crx WT* or R90W transcripts *ex vivo*. Degradation of *WT* and *E168d2* transcripts was also assessed in heterozygous *E168d2/+* retinas and allele-specific primers were used to assess the levels of each mRNA species. *WT* transcripts were more degraded at 4hrs (*WT* ~35%, *E168d2* 21%) and 8hrs (*WT* ~55%, *E168d2* ~15%), suggesting that *E168d2* degrades at a slower rate than *Crx WT* transcripts within the same retinal cells. This additionally suggests that the slower degradation of *E168d2* is not due to the disease state in *E168d2* retinas but is likely due to properties intrinsic to *E168d2* transcripts. Collectively, these results indicate the *E168d2* mRNA is more stable than *Crx WT mRNA*, implicating intrinsic RNA stability as a likely mechanism of mutant allele overexpression in *E168d2* mice.

Chapter IV

Discussion

Our results show that overexpression of mutant *Crx* is a common characteristic among several truncating *Crx* mutations and is conserved between mice, cats and humans. *E168d2* mice and Crx^{Rdy} cats have similar patterns of *Crx* mRNA and protein expression (Fig 4.1A-J), demonstrating both that allelic-expression imbalance isn't restricted to a particular *Crx* mutation and that it is conserved between species. This strengthens the utility of both the *E168d2* mouse and Crx^{Rdy} cat as matched large and small animal models for studying common mechanisms of disease for *Crx* mutations of this type. *In vitro* testing of human *CRX* truncation mutations matched the overexpression patterns in mouse and cat animal models (Fig 4.2A-C) suggesting that mutants of this type could be conserved for human mutants as well. The overexpression of *E168d2* was linked to increased mRNA stability compared to *WT Crx* (Fig 4.3A-D), suggesting that overexpression may be caused by alteration in the intrinsic properties of mutant *Crx* transcripts. In contrast, mouse and human R90W protein levels were decreased (Fig 4.2A) and its mRNA transcript stability was not significantly affected (Fig 4.3C). This suggests that mutations of this type may not match the patterns observed in truncated mutants. Overall these results support the hypothesis that truncation mutations within the C-terminal region of *Crx* alter mRNA stability leading to the overexpression of the mutant *Crx* allele. This characteristic is conserved among several truncating mutants and between species including humans, suggesting it may play an important role in disease. These results also reveal how accurate animal models of disease can be used to identify previously unknown mechanisms of disease. Results also have implications for designing mutation class-specific therapy strategies, possibly targeting mutant allele expression.

For detailed materials and methods please see Appendix B

Chapter IV

References

1. Terrell, D. *et al.* OTX2 and CRX rescue overlapping and photoreceptor-specific functions in the Drosophila eye. *Dev. Dyn.* **241,** 215–28 (2012).

2. Schweingruber, C., Rufener, S. C., Zünd, D., Yamashita, A. & Mühlemann, O. Nonsense-mediated mRNA decay - mechanisms of substrate mRNA recognition and degradation in mammalian cells. *Biochim. Biophys. Acta* **1829,** 612–23 (2013).

3. Menotti-Raymond M, Deckman KH, David VA, Myrkalo J, O'Brien SJ, N. K. Mutation discovered in a feline model of human congenital retinal blinding disease. *Invest Ophthalmol Vis Sci* (2010).

4. Jacobson, S. G., Kemp, C. M., Narfström, K. & Nilsson, S. E. Rhodopsin levels and rod-mediated function in Abyssinian cats with hereditary retinal degeneration. *Exp. Eye Res.* **49,** 843–52 (1989).

5. Chong, N. H., Alexander, R. a, Barnett, K. C., Bird, a C. & Luthert, P. J. An immunohistochemical study of an autosomal dominant feline rod/cone dysplasia (Rdy cats). *Exp. Eye Res.* **68,** 51–7 (1999).

6. Leon, a & Curtis, R. Autosomal dominant rod-cone dysplasia in the Rdy cat. 1. Light and electron microscopic findings. *Exp. Eye Res.* **51,** 361–81 (1990).

7. Leon, A. & Curtis, R. Autosomal Qominant Dysplasia findings in the Rdy Cat 2 . Electrophysiological. 489–502 (1991).

8. Tani, H. *et al.* Genome-wide determination of RNA stability reveals hundreds of short-lived noncoding transcripts in mammals. *Genome Res.* **22,** 947–56 (2012).

9. Tani, H. & Akimitsu, N. Genome-wide technology for determining RNA stability in mammalian cells: historical perspective and recent advantages based on modified nucleotide labeling. *RNA Biol.* **9,** 1233–8 (2012).

10. Chen, C.-Y. a, Ezzeddine, N. & Shyu, A.-B. *Messenger RNA half-life measurements in mammalian cells. Methods Enzymol.* **448,** 335–57 (Elsevier Inc., 2008).

11. Raghavan, A. & Bohjanen, P. R. Microarray-based analyses of mRNA decay in the regulation of mammalian gene expression. *Brief. Funct. Genomic. Proteomic.* **3,** 112–24 (2004).

Chapter IV

Table 4.1) Barcoded human Crx plasmid constructs

Plasmid	hCRX	Barcode #	XbaI-barcode-XbaI	Barcode	PCR primer F	PCR Primer R
pcDNA3.1 hisc	WT	1 reverse	TCTAGAGAGGATCCAGTCTAGA	GAGGATCCAG	GCGCCTACAGCCCCG	CTAGTCTAGACTGGATCCTC
pcDNA3.1 hisc	WT	2 forward	TCTAGACCGGATCCAATCTAGA	CCGGATCCAA	GCGCCTACAGCCCCG	CTCTAGTCTAGATTGGATCCGG
pcDNA3.1 hisc	WT	2 reverse	TCTAGATTGGATCCGGTCTAGA	TTGGATCCGG	GCGCCTACAGCCCCG	CTAGTCTAGACCGGATCCAA
pcDNA3.1 hisc	WT	3 reverse	TCTAGAGGCTGAAGCGTCTAGA	GGCTGAAGCG	GCGCCTACAGCCCCG	CTAGTCTAGACGCTTCAGCC
pcDNA3.1 hisc	DN	1 reverse	TCTAGAGAGGATCCAGTCTAGA	GAGGATCCAG	GCGCCTACAGCCCCG	CTAGTCTAGACTGGATCCTC
pcDNA3.1 hisc	DN	2 reverse	TCTAGATTGGATCCGGTCTAGA	TTGGATCCGG	GCGCCTACAGCCCCG	CTAGTCTAGACCGGATCCAA

Table 4.1) Barcoded human Crx plasmid constructs. Table shows the unique barcodes inserted into the 3' end of an Xpress tagged human CRX expressed from the pcDNA3.1hisc vector.

Fig 4.1)

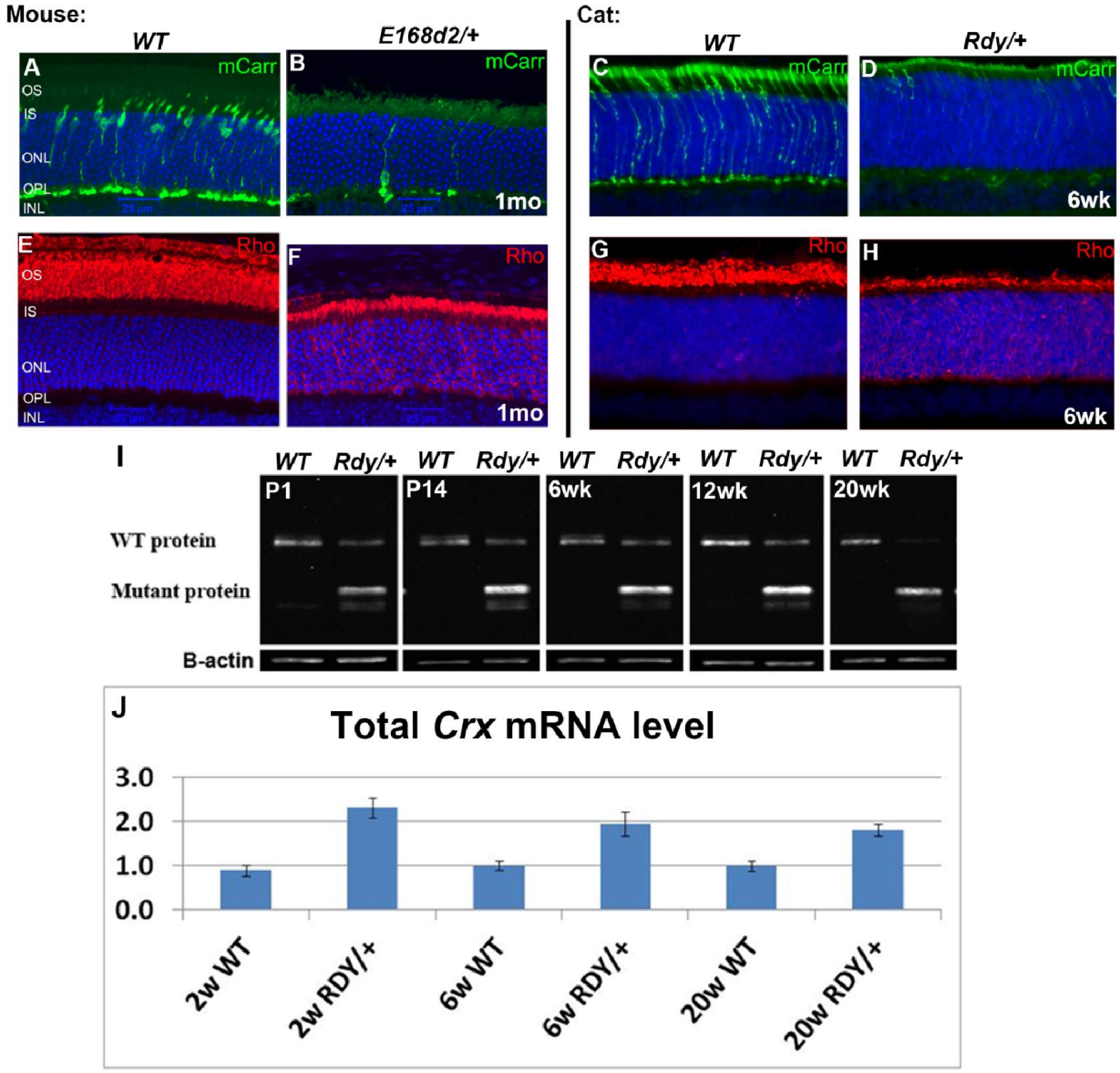
Mouse:
WT
E168d2/+
Cat:
WT
Rdy/+
A
mCarr
OS
IS
ONL
OPL
INL
B
mCarr
1mo
C
mCarr
D
mCarr
6wk
E
Rho
OS
IS
ONL
OPL
INL
F
Rho
1mo
G
Rho
H
Rho
6wk
I
WT
Rdy/+
WT
Rdy/+
WT
Rdy/+
WT
Rdy/+
WT
Rdy/+
P1
P14
6wk
12wk
20wk
WT protein
Mutant protein
B-actin
J
Total Crx mRNA level
3.0
2.0
1.0
0.0
2w WT
2w RDY/+
6w WT
6w RDY/+
20w WT
20w RDY/+

Chapter IV

Figure 4.1) Photoreceptor morphology and CRX expression in *Crx*^{Rdy} cats. A-D) Cone morphology in 1mo *WT* and *E168d2/+* mice (A-B) and 6wk *WT* and *Crx*$^{Rdy/+}$ cats (C-D) as determined by immunofluorescent staining for mCarr (green) of retinal sagittal sections, counterstain: DAPI (blue). Rod morphology in 1mo *WT* and *E168d2/+* mice (E-F) and 6wk *WT* and *Crx*$^{Rdy/+}$ cats (G-H) as determined by immunofluorescent staining for Rho (red) of retinal sagittal sections, counterstain: DAPI (blue). Scale bars: 25μM. I) Western blots of nuclear protein lysates from P1, P14, 6wk, 12wk and 20wk old *WT* and *Crx*$^{Rdy/+}$ cat retinas showing expression of CRX and β-actin. J) qRT-PCR results from 2wk, 6wk and 20wk old *WT* and *Crx*$^{Rdy/+}$ cat retinas showing the normalized expression of total *Crx* mRNA. Error bars: SEM.

Fig 4.2)

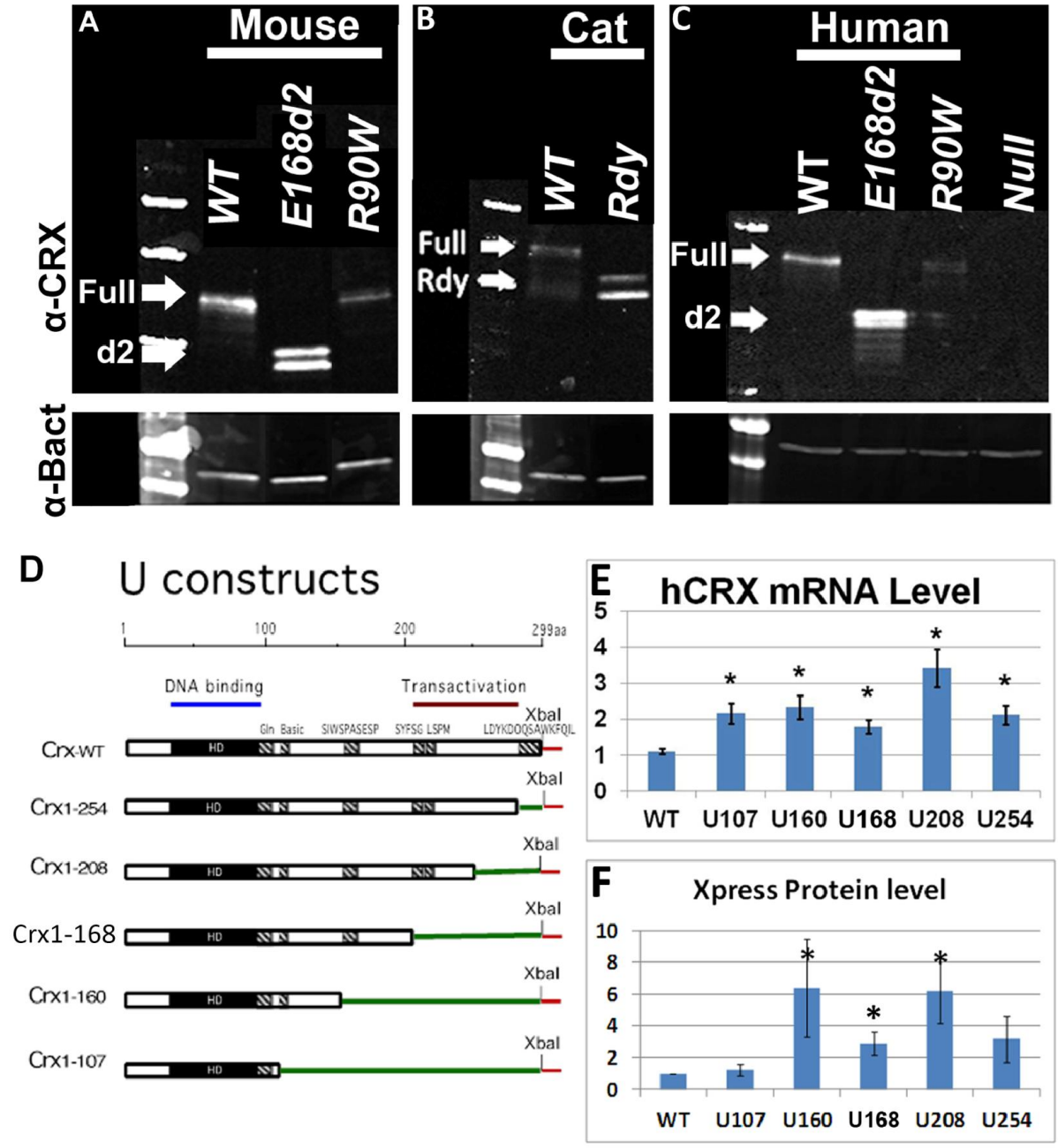
A
Mouse
WT
E168d2
R90W
α-CRX
Full
d2
α-Bact
B
Cat
WT
Rdy
Full
Rdy
C
Human
WT
E168d2
R90W
Null
Full
d2
D
U constructs
1
100
200
299aa
DNA binding
Transactivation
XbaI
Gln Basic
SIWSPASESP
SYFSG LSPN
LDYKDQQSAWKFQIL
Crx-WT
Crx1-254
Crx1-208
Crx1-168
Crx1-160
Crx1-107
HD
E
hCRX mRNA Level
5
4
3
2
1
0
WT
U107
U160
U168
U208
U254
F
Xpress Protein level
10
8
6
4
2
0
WT
U107
U160
U168
U208
U254

Figure 4.2) Expression of *Crx* mutants mRNA and protein *in vitro*. A-C) Western blots showing the expression of WT and mutant mouse, cat and human CRX proteins from pCAG constructs *in vitro*. β-actin expression is shown below as a loading control. 'α' symbol indicates antibody against the indicated gene. D) Schematic showing the plasmid design of human *CRX* 'U constructs'. From top to bottom: *CRX- WT, U254, U208, U168, U160* and *U107*. CRX protein domains associated with DNA binding (blue) and transactivation (red) are highlighted above. E) Quantification of human *CRX* 'U construct' mRNA expression *in vitro* measured by qRT-PCR. Results were normalized to *Ubb* and *Gapdh*. F) Quantification of human CRX 'U construct' protein expression *in vitro* measured by Western blot as determined by Xpress level normalized to β-ACTIN (β-ACT). Error bars: SEM, *P-val<0.05

Fig 4.3)

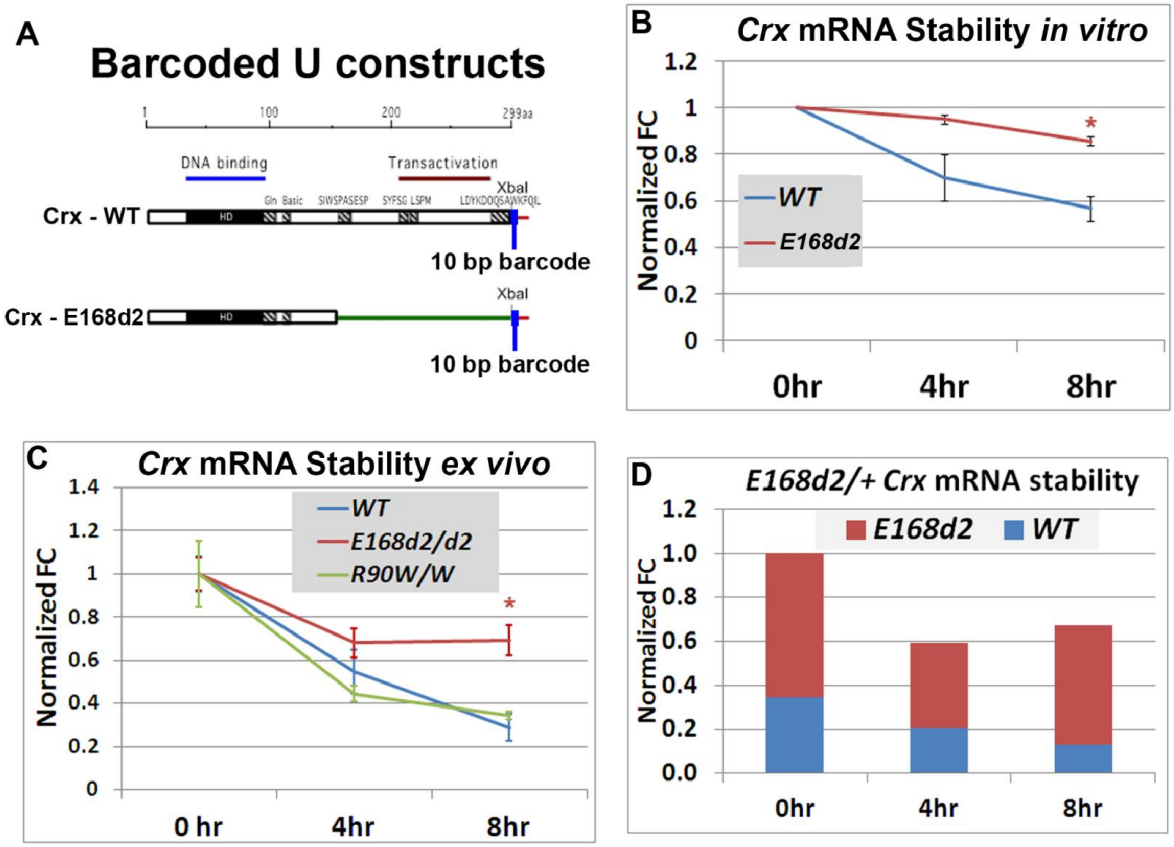
A
Barcoded U constructs
1
100
200
299aa
DNA binding
Transactivation
XbaI
Gln Basic
SIWSPASESP
SYFSG LSPM
LDYKDDDSAJWKFQIL
Crx - WT
HD
10 bp barcode
XbaI
Crx - E168d2
HD
10 bp barcode
B
Crx mRNA Stability in vitro
Normalized FC
1.2
1
0.8
0.6
0.4
0.2
0
WT
E168d2
*
0hr
4hr
8hr
C
Crx mRNA Stability ex vivo
Normalized FC
1.4
1.2
1
0.8
0.6
0.4
0.2
0
WT
E168d2/d2
R90W/W
*
0 hr
4hr
8hr
D
E168d2/+ Crx mRNA stability
Normalized FC
1.2
1.0
0.8
0.6
0.4
0.2
0.0
E168d2
WT
0hr
4hr
8hr

Figure 4.3) Stability of *Crx* mRNA *in vitro* and *ex vivo*. A) Schematic showing the design of barcoded human *CRX WT* and *E168d2* 'U constructs'. 10 base pair (bp) barcodes were inserted into the 3' end of human *WT* (4 distinct barcodes) and *E168d2* 'U constructs' (2 distinct barcodes). WT and *E168d2* construct carrying distinct barcodes were co-transfected in pairs for the analysis of expression within the same cell population. Co-transfected barcoded *WT* and *E168d2* constructs were treated with Actinomycin D for 4hrs or 8hrs and harvested. B) qRT-PCR showing the fold-change (FC) of *CRX* mRNA at 4hrs and 8hrs following the addition of Actinomycin D from transfected HEK 293 cells. Results were normalized to *Ubb* and *Gapdh* levels and shown relative to *CRX* expression at 0hrs. C) qRT-PCR showing the fold-change (FC) of Crx mRNA at 4hrs and 8hrs following the addition of Actinomycin D to P10 retinal explants from the indicated genotype. D) qRT-PCR showing the fold-change (FC) of Crx mRNA at 4hrs and 8hrs following the addition of Actinomycin D to P10 retinal explants from *E168d2*/+ mice. Allele-specific primers (Table 2.1) were used to selectively amplify *WT* and *E168d2* transcripts. The height of the bar indicates the expression of total Crx and the colors indicate the portion of expression composed of *WT* (blue) and *E168d2* (red) transcripts. Error bars: SEM, *P-val<0.05.

Chapter V

-

Assessment of Potential Therapeutic Strategies for *CRX*-Associated Retinopathies

Author: Nicholas Tran

Experiments and analysis contained within this chapter were performed by Nicholas Tran. Viral vectors for gene therapy experiments were subcloned and packaged by Sanford Boye and William Hauswirth (University of Florida).

Chapter V

Introduction: Hurdles to developing mechanism-based therapeutic strategies for *CRX*-associated retinopathies

Currently, **t**he vast majority of genetic retinopathies have few, if any, viable therapeutic strategies. This is in part because the enormously diverse genetic causes of retinopathies have made it difficult to generate accurate animal models to understand disease pathology and design appropriate treatments. The *E168d2* and *R90W* mouse models, along with the Crx^{Rdy} cat model, provide accurate disease models for multiple forms of *CRX*-associated disease. However, the generation and characterization of appropriate animal models is only the first hurdle to developing effective therapy for degenerative retinopathies.

The next challenge in developing effective therapy is delivering therapeutic agents to photoreceptor cells. The photoreceptor layer is completely avascular and is separated from the choroid by the blood-retina barrier. This makes small molecule drug delivery difficult unless the drug is taken up by the supporting retinal epithelial layer (RPE), which directly contacts photoreceptors, or is directly inserted into the eye, a highly invasive procedure. Nonetheless, progress in small molecule approaches has been made in both of these instances. Retinoids, critical components of phototransduction, that are naturally trafficked to the RPE where they are processed and delivered to the photoreceptors, have been used to treat congenital blindness, measles related childhood blindness and retinitis pigmentosa[1–3]. A variety of retinal diseases have been treated using slow-release capsules containing small molecule drugs or recombinant proteins proving effective in improving retinal function or photoreceptor survival[4,5].

Retinopathy is directly linked to mutations in genes whose function cannot be replaced by therapeutic agents. Targeting general pathways using drugs are often insufficient to completely rescue photoreceptor function and survival. This is expected to be the case for *CRX*-associated disease, since CRX plays such a critical role in photoreceptor transcription.

Additionally, drug-based treatment approaches require repeated dosing often with undesirable side effects or prohibitive costs. Substantial progress has been made in gene replacement strategies using recombinant adeno-associated virus (*rAAV*) mediated gene therapy[6–14]. The retina is an ideal tissue for targeting *rAAV* gene therapy, since it is immune-privileged, part of a self-contained accessible organ and has good epitope specificity for *rAAV* infection. Despite these advantages, there is still a need to identify *rAAV* serotypes which improve infection efficiencies and reduce toxicity. Additionally, with genes like *CRX*, that regulate the expression of many downstream target genes, the expression level needs to be carefully titrated as WT overexpression could be just as damaging as the disease itself.

Since retinopathies frequently result in the degeneration of photoreceptors, there is often a limited time window for effective delivery of therapeutic reagants. While some progress has been made in cell based therapies involving the transplantation, integration and differentiation of stem cells into mature photoreceptors, implantation rates are low and even successful approaches have only yielded modest gains in retinal function[15,16]. Nonetheless, cell replacement therapies may develop into viable treatment options in advanced retinal degeneration in the future.

Currently, there are no treatment strategies for *CRX*-associated diseases. Since CRX influences many cellular processes, designing targeted therapy is exceptionally difficult. The availability of phenotypically and mechanistically distinct models for *CRX*-associated disease greatly improve our ability to develop novel therapies. *E168d2*, *E168d2neo* and *R90W* present unique mechanistic challenges for therapy to address. Like -/- mice, *E168d2*/+, *E168d2/d2* and *R90W/W* mice all have highly abnormal photoreceptor morphology and undergo rapid degeneration, which may restrict the time course and effectiveness of treatment. The improved phenotype of *E168d2neo*/+ mice, compared to *E168d2/*+, provides evidence that gene replacement strategies that shift the ratio of WT to mutant CRX could be effective at improving

vision and promoting rod and cone survival in cases were a mutant protein is toxic and/or overexpressed. Previous studies have shown this strategy to be effective in treating a dominant-negative adRP RHO animal model[9,17]. Lastly, the similarity of the *E168d2*/+ mouse and the Crx^{Rdy} cat provide excellently matched small and large animal models. Therapies that are proven to be effective in the *E168d2/+* mouse can immediately be tested in the Crx^{Rdy} cat, which improves our ability to develop translational therapies.

Here we present the preliminary testing of a small molecule based approach using 13-cis retinoic acid (13-cis RA) (Sigma-Aldrich) to target the visual cycle, and *rAAV*-mediated approaches for *CRX* gene delivery and mutant protein silencing in the retina.

Results

5.1. Preventing retinal degeneration by targeting the visual cycle

Analysis of the gene expression profiles of *E168d2* and *E168d2neo* retinas identified many photoreceptor specific genes that are downregulated including genes involved in retinoid recycling like *Rdh12*, *Irbp* and *Abca4*. Genes involved in retinoid recycling are critical for the sensitivity of photoreceptors to light-induced stress due to their role in processing retinoid by-products of phototransduction[18–23]. This led to the hypothesis that heterozygous *E168d2* and *E168d2neo* mice might have increased sensitivity to light-induced degeneration. To test this hypothesis, we subjected adult *WT, E168d2/+* and *E168d2neo/+* mice to an 8hr 11.5-13.5KLUX light damage (LD) treatment. After 7 days of recovery in 12hr light-dark ambient light conditions, mice were sacrificed and retinal morphology was assessed by histological H&E staining of paraffin embedded retinal sagittal sections. All mice tested were on a congenic C57BL6/J background, which is highly resistance to light damage[18]. As expected, no thinning of the ONL was observed in LD treated *WT* mice compared to littermates raised under normal light

conditions (Fig 5.1 D vs. A). Surprisingly, however, *E168d2neo*/+ and *E168d2*/+ mice differed in their susceptible to light damage. *E168d2neo*/+ mice show reduced outer segment length and thinning of the ONL following light exposure (Fig 5.1 E vs. B), suggesting *E168d2neo* sensitized the mice to light-induced degeneration. In contrast, *E168d2*/+ mice were minimally affected by light damage (Fig 5.1 F vs. C), suggesting these mice were not sensitized to light-induced degeneration. These results suggest that despite expressing the same mutant CRX protein, *E168d2neo/+* and *E168d2/+* mice were differentially sensitized to light-induced retinal degeneration.

To test if the increased sensitivity to light damage in *E168d2neo*/+ mice was linked to the retinoid pathway, mice were treated with 13-cis RA. 13-cis RA blocks the visual cycle in the RPE[24], leading to decreased burden on the retinoid pathway in photoreceptors. Targeting the visual cycle using the retinoids 13-cis RA or retinalymine has been shown to be effective at preventing light-induced degeneration[3,18,20,24–26]. Light-induced degeneration is associated with the accumulation of toxic by-products including A2E derived from inactivated all-trans retinal[3,18,20,22,24–27]. Drugs that inhibit the visual cycle reduce the amount of active 13-cis retinal that is delivered to the photoreceptors and hence reduce the burden on the recycling and clearance of inactivated retinoids. Mice were treated 12hrs and redosed 30min before LD treatment. 13-cis RA did not have any effect on *WT* and *E168d2*/+ retinal morphology following LD treatment (Fig 5.1 H vs. G & M vs. L), which were not sensitized to light damage. In *E168d2neo*/+ mice, however, 13-cis RA treatment preserved retinal morphology following LD treatment compared to DMSO controls (Fig 5.1 J vs. I), suggesting 13-cis RA was protective for *E168d2neo*/+ photoreceptor survival. Retinal function of 13-cis RA treated and DMSO treated *E168d2neo*/+ mice was measured using ERG's 7 days after LD. 13-cis RA treatment of *E168d2neo/+* reduced the loss of rod and cone function following LD exposure (Fig 5.1N-P green vs. red lines), suggesting 13-cis RA protected retinal function from light-induced damage.

Collectively, light damage experiments reveal that *E168d2neo*/+ and *E168d2*/+ mice are differentially susceptible to light-induced retinal degeneration, suggesting distinct pathways to degeneration in these mice. As *E168d2*/+ do not have increased sensitivity to light damage but have expensive photoreceptor degeneration, *E168d2*/+ were dark-reared for 3mo to see if degeneration was dependent on light conditions. *E168d2*/+ mice raised in constant darkness had similar morphology to littermates raised under normal light conditions (Fig 5.1Q), suggesting degeneration was light-independent. Overall, results suggest that photoreceptor degeneration in *E168d2neo*/+ mice is accelerated by intense light exposure, while photoreceptor degeneration in *E168d2*/+ is light-independent.

5.2. Improving visual function by rAAV-mediated gene delivery

The graded phenotypes of *E168d2*/+ and *E168d2neo*/+ mice suggest modulating the ratios of WT:mutant CRX might be effective at improving retinal integrity and function. The antimorphic nature of this mutant protein may necessitate not only the delivery of a *WT* copy of the *CRX* gene but also the silencing of the antimorphic allele. The ability of *rAAV*-mediated *CRX* and *CRX shRNA* gene therapy to transduce photoreceptors and affect downstream target gene expression was tested. The effectiveness of *CRX* gene delivery was first tested in *Crx* -/- mice. A high titer of *rAAV5* carrying 3xFLAG tagged human *CRX* or *Green fluorescent protein* (*Gfp)* expressed under the photoreceptor specific *Rhodopsin Kinase* (*GRK)* promoter[28] were co-injected into the subretinal space of P0 *Crx* -/- mice. Retinas were collected at P21 for assessment of morphology and gene expression by fluorescent immunohistochemistry. Sagittal retinal frozen sections were stained with antibodies against FLAG, which marked cells expressing delivered CRX, and CARR, a cone-specific CRX target gene which was not expressed in uninfected *Crx* -/- retina (Fig 5.2A). *rAAV* infected retinas show expression of Carr that was completely restricted to FLAG positive cells (Fig 5.2B, white arrows), suggesting that

delivered human CRX was able to drive the expression of the downstream CRX gene CARR in *Crx* -/- retinas. *rAAV5* carrying *Crx* shRNA/ mCherry expressed under the *GRK* promoter was injected into the subretinal space of P0 *WT* mice to determine if silencing of *Crx* expression by shRNA was capable of affecting the expression of downstream CRX target genes. As above, eyes were collected at P21 for morphological analysis by immunofluorescence. Sagittal retinal frozen sections were stained with peanut agglutanin (PNA), a marker for all cones, and an antibody against CARR. PNA positive cones expressing mCherry showed were negative for CARR (Fig 5.2C, red arrows), suggesting that *CRX* shRNA effectively downregulated the expression of this CRX target genes. Collectively, these experiments suggest that *rAAV*-mediated *CRX* and *Crx* shRNA gene therapy was effective at infecting photoreceptors and affecting the expression of a CRX target gene, suggesting it may be a viable approach for targeted therapy.

The greatest limitation of the *rAAV5* experiments described above was the low infection efficiency of the viral vector. While local infection rates near the injection site could reach ~50-60%, overall only ~1-5% of photoreceptors were infected across the entire retina. Given the low infection efficiency, the potential for improving retinal function using *rAAV5* CRX gene therapy is negligible. To address this, we sought to identify *rAAV* serotypes with improved infection efficiency in the retina. To this end, the infection efficiency of several *rAAV* serotypes carrying *Gfp* expressed under the control of the ubiquitous U11 promoter was tested in *WT* and *Crx* -/- mice. Eyes were dissected at P21 and Gfp expression across the retina was imaged. The serotypes *rAAV5*, *rAAV2* triple tyrosine mutant (*rAAV2 Trip*), and *rAAV2* quadruple tyrosine mutant (*rAAV2 Quad*) were found to be capable of infecting *WT* and *Crx* -/- photoreceptors (Fig 5.2D-I). Similar to previous studies[29], *rAAV2 Trip* gave the highest rate of infection of photoreceptors. *rAAV2* Trip expressing *Gfp* under the control of the *GRK* promoter showed efficient infection of *WT*, *E168d2*/+ and *Crx* -/- retinas (Fig 5.2 J-L), suggesting this *rAAV*

serotype may improve efficacy of *rAAV5*-mediated gene therapy. *rAAV2* Trip *CRX* and *CRX* shRNA gene therapy approaches are currently in development in the lab.

Discussion

Preliminary testing of therapy approaches aimed at preventing retinal degeneration and restoring function demonstrate both the utility of having accurate disease models and the significant hurdles still remaining for therapy development. The dominant retinopathy mouse models *E168d2* and *E168d2neo* express the same mutant CRX protein at different levels (Fig 2.2), correlating with their phenotypic severity. The distinct phenotypes of these mice was found to be associates with small changes in the expression level of a common set of genes (Fig 3.4-3.7), suggesting critical thresholds for target gene expression and phenotypic severity. Taking into account the similarities of *E168d2* and *E168d2neo* mouse models, it was surprising that degeneration in each of these models seems to be driven by different mechanisms. *E168d2*/+ mouse retinas undergo progressive rapid photoreceptor degeneration under normal light conditions (Fig 2.5). Degeneration was found to be light-independent (Fig 5.1Q) and photoreceptors are not sensitized to light damage (Fig 5.1 F vs. C). In contrast, *E168d2neo*/+ undergo slow degeneration of cones but not rods under normal light conditions (Fig 2.5, Fig 2.8) and photoreceptors were highly sensitized to light damage (Fig 5.1 E vs. B). 13-cis RA treatment in *E168d2neo*/+ mice was effective at protecting the retinas from light-induced degeneration (Fig 5.1 J vs. I), suggesting that degeneration is associated with the retinoid pathway. *E168d2neo*/+ mice have significantly higher retinal function than *E168d2*/+ mice when raised under normal light conditions (Fig 2.9), suggesting sensitivity to light damage may have requisite levels of baseline retinal function. These results demonstrate that even reasonably similar diseases i.e. dominantly inherited retinopathies caused by the same mutant protein and

affecting similar sets of genes, could have vastly different responses to therapy, necessitating the careful design and evaluation of therapeutic approaches.

Testing of gene delivery approaches in *Crx* mutant mice currently remain in preliminary stages but offers promising results. First, *rAAV5*-mediated gene delivery of human *CRX* to *Crx* -/- mouse retinas was shown to drive the expression of the downstream CRX target gene *Carr* (Fig 5.2B). Second, *rAAV5*-mediated shRNA knock-down of endogenous *Crx* was effective at downregulating CARR expression in the cones of *WT* retinas (Fig 5.2C). These results indicate that gene therapy approaches were capable of rescuing or silencing CRX function, suggesting that gene therapy is a viable approach for targeting downstream pathways of CRX. However, infection efficiency was too low to significantly affect overall retinal function. The efficacy of *Crx* gene therapy using an alternate *rAAV* serotype with improved infection efficiency, *rAAV2 Trip*, is currently being evaluated. The design of effective gene therapy approaches in *E168d2* mice will be immediately applicable to the well-matched Crx^{Rdy} cat model, improving our understanding of its overall effectiveness and safety.

For detailed materials and methods please see Appendix B

Chapter V

References

1. Mayo-wilson, E., Imdad, A., Herzer, K., Yawar, M. & Noordin, Z. A. B. Vitamin A supplements for preventing mortality , illness , and blindness in children aged under 5 : systematic review and meta-analysis. 1–19 (2011). doi:10.1136/bmj.d5094

2. Bello, S., Mm, M., Ri, E. & Oduwole, O. Routine vitamin A supplementation for the prevention of blindness due to measles infection in children (Review). (2011).

3. Palczewski, K. Retinoids for treatment of retinal diseases. *Trends Pharmacol. Sci.* **31,** 284–95 (2010).

4. Wang, J., Jiang, A., Joshi, M. & Christoforidis, J. Drug delivery implants in the treatment of vitreous inflammation. *Mediators Inflamm.* **2013,** 780634 (2013).

5. Wen, R., Tao, W., Li, Y. & Sieving, P. a. CNTF and retina. *Prog. Retin. Eye Res.* **31,** 136–51 (2012).

6. Maguire, A. M. *et al.* Safety and efficacy of gene transfer for Leber's congenital amaurosis. *N Engl J Med* **358,** 2240–2248 (2008).

7. Bennicelli, J. *et al.* Reversal of blindness in animal models of leber congenital amaurosis using optimized AAV2-mediated gene transfer. *Mol Ther* **16,** 458–465 (2008).

8. Sahel, J.-A. & Roska, B. Gene therapy for blindness. *Annu. Rev. Neurosci.* **36,** 467–88 (2013).

9. Chadderton, N. *et al.* Improved retinal function in a mouse model of dominant retinitis pigmentosa following AAV-delivered gene therapy. *Mol. Ther.* **17,** 593–9 (2009).

10. Surace, E. M. & Auricchio, A. Versatility of AAV vectors for retinal gene transfer. *Vis. Res* **48,** 353–359 (2008).

11. Acland, G. M. *et al.* Gene therapy restores vision in a canine model of childhood blindness. *Nat Genet* **28,** 92–95 (2001).

12. Cideciyan, A. V *et al.* Human gene therapy for RPE65 isomerase deficiency activates the retinoid cycle of vision but with slow rod kinetics. *Proc. Natl. Acad. Sci. U. S. A.* **105,** 15112–7 (2008).

13. Mancuso, K. *et al.* Gene therapy for red-green colour blindness in adult primates. *Nature* **461,** 784–787 (2009).

14. Colella, P. & Auricchio, A. Gene therapy of inherited retinopathies: a long and successful road from viral vectors to patients. *Hum. Gene Ther.* **23,** 796–807 (2012).

15. Lamba, D. a, Gust, J. & Reh, T. a. Transplantation of human embryonic stem cell-derived photoreceptors restores some visual function in Crx-deficient mice. *Cell Stem Cell* **4,** 73–9 (2009).

16. MacLaren, R. E. *et al.* Retinal repair by transplantation of photoreceptor precursors. *Nature* **444,** 203–7 (2006).

17. O'Reilly, M. *et al.* A transgenic mouse model for gene therapy of rhodopsin-linked Retinitis Pigmentosa. *Vision Res.* **48,** 386–91 (2008).

18. Wenzel, A., Reme, C. E., Williams, T. P., Hafezi, F. & Grimm, C. The Rpe65 Leu450Met variation increases retinal resistance against light-induced degeneration by slowing rhodopsin regeneration. *J Neurosci* **21,** 53–58 (2001).

19. White, D. A., Fritz, J. J., Hauswirth, W. W., Kaushal, S. & Lewin, A. S. Increased sensitivity to light-induced damage in a mouse model of autosomal dominant retinal disease. *Invest Ophthalmol Vis Sci* **48,** 1942–1951 (2007).

20. Maeda, A. *et al.* Redundant and unique roles of retinol dehydrogenases in the mouse retina. *Proc. Natl. Acad. Sci. U. S. A.* **104,** 19565–70 (2007).

21. Hao, W. *et al.* Evidence for two apoptotic pathways in light-induced retinal degeneration. *Nat Genet* **32,** 254–260 (2002).

22. Sparrow, J. R., Nakanishi, K. & Parish, C. a. The lipofuscin fluorophore A2E mediates blue light-induced damage to retinal pigmented epithelial cells. *Invest. Ophthalmol. Vis. Sci.* **41,** 1981–9 (2000).

23. Maeda, T. *et al.* NIH Public Access. **50,** 4917–4925 (2009).

24. Sieving, P. a *et al.* Inhibition of the visual cycle in vivo by 13-cis retinoic acid protects from light damage and provides a mechanism for night blindness in isotretinoin therapy. *Proc. Natl. Acad. Sci. U. S. A.* **98,** 1835–40 (2001).

25. Maeda, A. *et al.* Effects of Potent Inhibitors of the Retinoid Cycle on Visual Function and Photoreceptor Protection from Light Damage in Mice □. 1220–1229 (2006). doi:10.1124/mol.106.026823.

26. Radu, R. a *et al.* Treatment with isotretinoin inhibits lipofuscin accumulation in a mouse model of recessive Stargardt's macular degeneration. *Proc. Natl. Acad. Sci. U. S. A.* **100,** 4742–7 (2003).

27. Sparrow, J. R. *et al.* A2E, a byproduct of the visual cycle. *Vision Res.* **43,** 2983–2990 (2003).

28. Khani, S. C. *et al.* AAV-mediated expression targeting of rod and cone photoreceptors with a human rhodopsin kinase promoter. *Invest Ophthalmol Vis Sci* **48,** 3954–3961 (2007).

29. Petrs-Silva, H. *et al.* Novel properties of tyrosine-mutant AAV2 vectors in the mouse retina. *Mol. Ther.* **19,** 293–301 (2011).

30. Khani, S. C. *et al.* AAV-mediated expression targeting of rod and cone photoreceptors with a human rhodopsin kinase promoter. *Invest Ophthalmol Vis Sci* **48,** 3954–3961 (2007).

31. Kay, C. N. *et al.* Targeting photoreceptors via intravitreal delivery using novel, capsid-mutated AAV vectors. *PLoS One* **8,** e62097 (2013).

32. Bennett, J. *et al.* Stable transgene expression in rod photoreceptors after recombinant adeno-associated virus-mediated gene transfer to monkey retina. *Proc Natl Acad Sci U S A* **96,** 9920–9925 (1999).

33. Zolotukhin, S. *et al.* Production and purification of serotype 1, 2, and 5 recombinant adeno-associated viral vectors. *Methods* **28,** 158–67 (2002).

34. Jacobson, S. *et al.* Safety of Recombinant Adeno-Associated Virus Type 2–RPE65 Vector Delivered by Ocular Subretinal Injection. *Mol. Ther.* **13,** 1074–1084 (2006).

Fig 5.1)

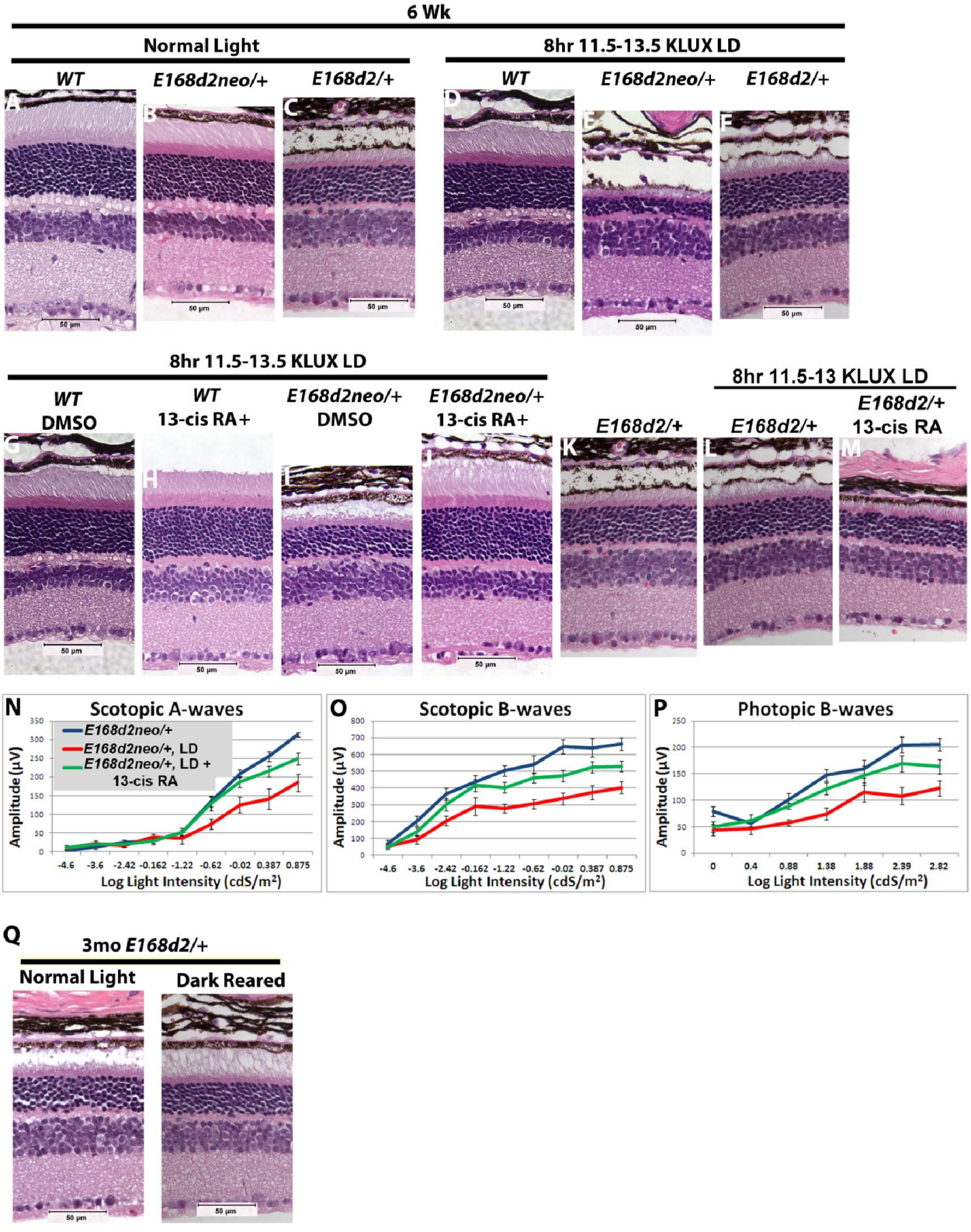
6 Wk
Normal Light
8hr 11.5-13.5 KLUX LD
WT
E168d2neo/+
E168d2/+
WT
E168d2neo/+
E168d2/+
A
B
C
D
E
F
50 µm
8hr 11.5-13.5 KLUX LD
WT DMSO
WT 13-cis RA+
E168d2neo/+ DMSO
E168d2neo/+ 13-cis RA+
8hr 11.5-13 KLUX LD
E168d2/+
E168d2/+
E168d2/+ 13-cis RA
G
H
I
J
K
L
M
N
Scotopic A-waves
E168d2neo/+
E168d2neo/+, LD
E168d2neo/+, LD + 13-cis RA
Amplitude (µV)
Log Light Intensity (cdS/m²)
-4.6 -3.6 -2.42 -0.162 -1.22 -0.62 -0.02 0.387 0.875
O
Scotopic B-waves
Amplitude (µV)
Log Light Intensity (cdS/m²)
P
Photopic B-waves
Amplitude (µV)
0 0.4 0.88 1.38 1.88 2.39 2.82
Log Light Intensity (cdS/m²)
Q
3mo E168d2/+
Normal Light
Dark Reared

Chapter V

Figure 5.1) Light-induced retinal degeneration in *E168d2* mice. A-C) Morphology of 6wk old WT, *E168d2neo*/+ and *E168d2*/+ mouse retinas under normal light conditions, as determined by H&E staining of paraffin embedded retinal sagittal sections. D-F) Morphology of 6wk old *WT*, *E168d2neo*/+ and *E168d2*/+ mouse retinas 7 days following 8hr 11-13.5KLUX light damage (LD), as determined by H&E staining of paraffin embedded retinal sagittal sections. H-M) Morphology of 6wk old WT, *E168d2neo*/+ and *E168d2*/+ mouse retinas 7 days following 8hr 11-13.5KLUX LD with pre-treatment of 13-cis RA vs. DMSO control, as determined by H&E staining of paraffin embedded retinal sagittal sections. Scale bars: 50μM. N-P) Scotopic and photopic electroretingrams of 6wk old *E168d2neo*/+ 7 days following 8hr 11-13.5KLUX LD with pre-treatment of 13-cis RA (green line) vs. DMSO control (red line) and non-LD control mice (blue line). Q) Morpology of 3mo *E168d2*/+ mice raised in normal light vs. constant darkness, as determined by H&E staining of paraffin embedded retinal sagittal sections.

Fig 5.2)

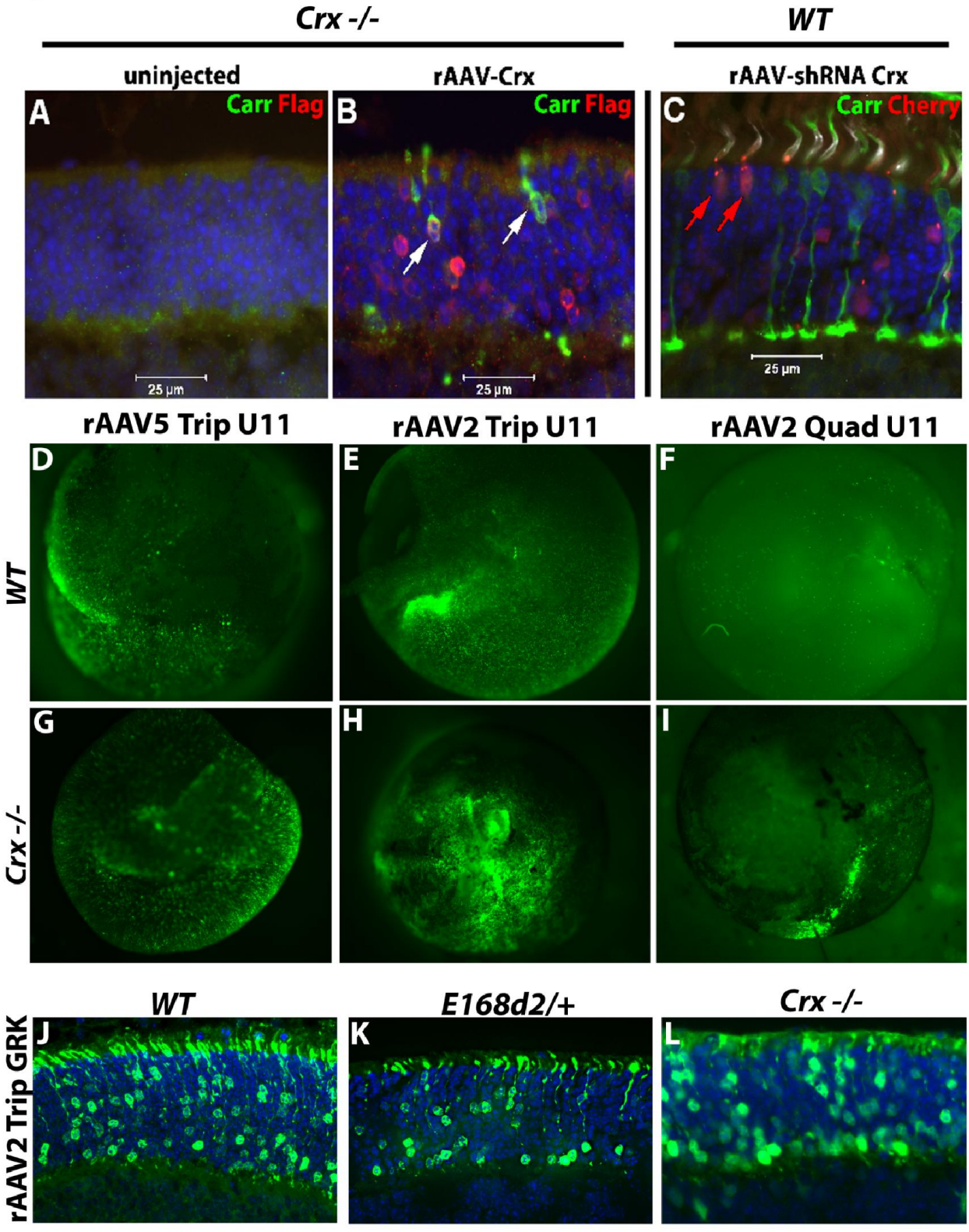
Crx -/-
WT
uninjected
rAAV-Crx
rAAV-shRNA Crx
A
Carr Flag
B
Carr Flag
C
Carr Cherry
25 µm
25 µm
25 µm
rAAV5 Trip U11
rAAV2 Trip U11
rAAV2 Quad U11
D
E
F
WT
G
H
I
Crx -/-
WT
E168d2/+
Crx -/-
rAAV2 Trip GRK
J
K
L

Figure 5.2) Evaluation of *rAAV*-mediated *CRX* and *Crx* shRNA gene therapy approaches. A-B) Fluorescent immunohistochemistry showing the expression of delivered 3xFLAG-tagged human CRX, as determined by detection with a monoclonal FLAG antibody (red), and the cone-specific CRX target gene, CARR (green), in frozen retinal sagittal sections, 21 days following infection with *rAAV5 GRK-hCRX*. C) Fluorescent immunohistochemistry showing the expression of delivered *mCrx* mCherry shRNA, as determined by mCherry expression (red), the cone-specific CRX target gene, CARR (green), and the general cone marker PNA (white) in frozen retinal sagittal sections, 21 days following infection with *rAAV5 mCrx shRNA*. Scale bars: 25μM. D-I) Fluorescent macroscope images showing the expression of GFP in retinas of *WT* and *-/-* mice, 21 days following infection with *rAAV5*, *rAAV2 triple Y-F* or *rAAV2 quadruple Y-F* mutant viral capsids containing *CBA* (*UF11)-Gfp* viral constructs. J-L) Fluorescent images of retinal sagittal sections showing the expression of GFP in *WT, E168d2/+* and *-/-* mouse retinas, 21 days following infection with *AAV2 triple Y-F* containing a *GRK-Gfp* viral construct.

Chapter VI

-

Conclusions and Future Directions

Author: Nicholas Tran

Chapter VI

While great progress has been made in the identification of the genetic causes of blindness, the lack of appropriate animal models has often greatly hampered our understanding of disease pathology and the underlying cellular mechanisms. Such is the case for blinding diseases linked to mutations in gene *CRX*. CRX is a retinal transcription factor that plays a critical role in regulating gene expression in photoreceptors. Previous studies indicate that different disease causing *CRX* mutations distinctly alter the molecular function of CRX protein, falling into at least two functional groups. The two primary classes of CRX mutant proteins are antimorphic c-terminal truncated proteins which actively impair target gene transcription and hypomorphic proteins with substitution mutations with reduced ability to bind DNA. Antimorphic truncation mutations are associated with severe forms of dominant CoRD and LCA[1–10], while hypomorphic substitution mutations are associated with less severe forms[11–13]. A few specific substitution mutations maintain DNA-binding activity and are associated with more severe disease and are thought to be distinct from the hypomorphic group[11,13]. The relationship between mutation type and disease severity lead us to the hypothesis that phenotypic variability was, at least in part, caused by mechanistically distinct groups of mutant CRX proteins.

To test this hypothesis, we selected two *CRX* mutations for further study as representative mutations for the two main groups: *E168d2,* which produces a truncated, antimorphic protein and is associated with severe dominant retinopathy, and *R90W*, which produces a hypomorphic protein with reduced DNA-binding and is associated with a mild dominant retinopathy. We generated two *Knock-IN* mouse lines, *Crx E168d2* and *R90W*. We found that *E168d2* and *R90W* mice accurately recapitulated their associated human phenotypes, establishing them as viable models for studying the pathobiology of *CRX*-associated disease and supporting the hypothesis that mutation type influences disease severity.

Chapter VI

The phenotypes of *E168d2* and *R90W* mouse retinas were characterized in detail by assessing retinal morphology, function and gene expression. Homozygous *E168d2/d2* and *R90W/W* mice both show incomplete maturation and progressive degeneration of photoreceptors, which did not form outer segments or establish physiological function. Expression of CRX target genes was more reduced in *E168d2/d2* retinas, compared to *R90W/W* and *Crx -/-*, correlating with more rapid photoreceptor degeneration giving evidence that E168d2 protein has an antimorphic effect *in vivo*. Heterozygous *E168d2/+* had strong dominant phenotype with rapid photoreceptor degeneration occurring first in cones and reduced retinal function, while *R90W/+* mice largely only had a mild deficit in retinal function at late ages. This suggests that distinct molecular defects in CRX protein cause different retinal phenotypes and likely account for much of the phenotypic variation in human patients.

Unexpectedly *E168d2* mRNA and protein were overexpressed in *E168d2* mouse retinas compared to *WT Crx*. Since E168d2 protein was found to have antimorphic activity, the expression level could be an important genetic modifier of disease severity. This prediction was tested by characterizing the phenotype of the mouse *E168d2neo,* which expresses the same E168d2 protein but at lower levels due to the inclusion of an intronic *neo* cassette. Heterozygous *E168d2neo*/+ mice had a dramatically less severe phenotype than *E168d2*/+ mice, demonstrating that mutant expression level is a critical modifier of phenotypic outcome. Expression profiling additionally showed that similar subsets of genes were affected in *E168d2* and *E168d2neo* mice but were slightly less severe in *E168d2neo* mice. This showed that small changes in the expression of a large set of genes had a big impact on phenotypic outcome. The *E168d2* and *E168d2neo* mice suggest that the truncated CRX protein E168d2 has antimorphic activity whose expression level directly affected phenotypic outcome.

It was unclear if the mutant protein overexpression phenotype of *E168d2* mice was representative of a general characteristic of truncated CRX proteins or specific to this mutation.

Chapter VI

A previous study in *Drosophila* had identified that another human *CRX* frameshift mutation, *I138*^{fs48}*,* is overly stable[14]. To investigate this further, the expression of *Crx* mRNA and protein in the *Crx*^{Rdy} feline model was assessed. *Crx*^{Rdy} cat carry a frameshift mutation in an endogenous Crx allele, *n.546delC,* which was predicted to encode a truncated CRX protein just 14 A.A. longer than *E168d2*. *Crx*^{Rdy} cats expressed the truncated mutant *Crx* mRNA and protein at higher levels than *WT Crx*, similar to *E168d2* mice. This result showed that overexpression of mutant *Crx* was observed for two different truncation mutations and was even conserved between two species, suggesting a common mechanism. Several human *CRX* truncation mutations were tested *in vitro* and were also found to be expressed at higher levels than *WT CRX*. Collectively, these results demonstrate that several truncated CRX mutations were overexpressed suggesting a possible shared mechanism for mutations of this type. This finding could have critical implications for understanding *CRX*-associated disease pathology, as mutant expression level was a strong genetic modifier of the *E168d2* mouse phenotype.

To understand the nature of truncated *Crx* overexpression, the stability of *WT* and *E168d2* mRNA was tested. *E168d2* mRNA was shown to be more stable than *WT Crx* both *in vitro* and *in vivo* in both heterozygous and homozygous mice. These results link the overexpression of a truncated mutant *Crx* with altered mRNA stability. Currently, experiments are being planned to determine whether altered mRNA stability is common between additional disease causing *Crx* mutations. The stability of multiple forms of *Crx* can be assessed simultaneously *in vitro* using the barcoding technique first tested with *WT* and *E168d2* (Fig 4.2A-B). Barcodes are being cloned into several human disease causing mutations to allow for the high throughput assessment of *CRX* mRNA stability. Additionally, the use of Actinomycin D to generally block transcription could affect the natural mRNA degredation pathways yielding a result that is not truly representative of the *in vivo* state. To improve upon these experiments, BrU-based mRNA labeling pulse-chase experiments, based on previous established

techniques[15,16], are being designed to track the half-life of *Crx* mRNA under natural conditions. Finally, the specific mechanism of increased mRNA stability is currently unknown. Further study to characterize the *Crx* sequence requirements and potential interacting proteins/RNAs will be necessary to begin to elucidate this mechanism. It is also of interest to assess if altered mRNA stability is common among truncating mutations of other genes, namely homeobox family members, possibly indicative of a conserved mechanism.

The *Crx E168d2* and *R90W Knock-IN* mice demonstrate the value of having mechanism-based true-to-disease animal models. They improve upon current understanding of disease pathology in distinct forms of *CRX*-associated retinopathy and allow the identification of the underlying cellular pathways. Phenotypic severity in these mice were associated with graded changes in the expression of similar sets of genes. However, small changes in target gene expression level, as seen between *E168d2* and *E168d2neo* mice, could have dramatic impact on phenotype, susceptibility to different stressors and effectiveness of therapeutic strategy. The observation of mutant overexpression of *E168d2* mRNA and protein and its link to altered mRNA stability identify a previously unknown characteristic of this *CRX* mutation, further demonstrating the utility of having human mutation based animal models. The severe dominant retinal phenotype and shared mutant allele overexpression in the *E168d2* mouse and the Crx^{Rdy} cat give strong evidence that these mutants cause disease through common mechanisms. This both allows for the cross-validation of findings in each model and increases their utility as animal models for a larger group of disease causing mutations. While these animal models surely do not serve as representative models for all forms of *CRX*-associated disease, their utility as accurate disease models clearly extend beyond their specific *Crx* mutation.

The availability of viable animal models for distinct forms of *CRX*-associated disease will allow for the development and testing of novel therapeutic strategies. The *E168d2* mouse and Crx^{Rdy} cat additionally provide matched small and large animal models. Therapies found to be

effective in the mouse can be directly translated to the cat, increasing the utility of these studies. Previously, the efficacy of rAAV-mediated gene therapy and stem cell transplantation were tested in *Crx KO* mice with both approaches being successful in achieving modest gains in retinal morphology and function[17,18]. However, the *Crx KO* mouse is not truly representative of human disease inheritance or pathology. The *E168d2* and *E168d2neo* mice demonstrate the importance of having accurate disease models. These mice displayed differential susceptibility to light damage and effectiveness of 13-cis RAL treatment. Therefore, the efficacy of drugs targeting the visual cycle could be highly context specific for *CRX*-associated diseases. While targeting the visual cycle may have potential for protecting photoreceptors from degeneration, it will not improve retinal function in *CRX*-associated diseases. rAAV-mediated *CRX* gene therapy approaches may currently have the most potential for rescuing retinal function for these diseases. The emergence of retinal functional defects occurs before photoreceptor degeneration, suggesting a possible window for effective gene therapy. The antimorphic activity of some *Crx* mutants may necessitate a combinatorial approach to remove the antimorphic effects and rescue gene function. This can be achieved by combining *Crx* shRNA to knockdown endogenous gene expression with gene delivery of an shRNA resistant *CRX.* Preliminary evaluation of rAAV-mediated gene therapy shows that *Crx* shRNA and human *CRX,* which is *Crx* shRNA resistant, are effective at regulating downstream targets but that infection efficiency needs to be improved to have therapeutic benefit. Further evaluation of rAAV serotypes and expression vectors need to be tested to optimize gene therapy approaches.

In conclusion, the generation and characterization of mechanistically distinct animal models have greatly improved our understanding of *CRX*-associated disease. The phenotypic variation in human patients is, at least in part, driven by mutant proteins with different molecular properties. Mutant proteins fall into functional groups reflective of their molecular activity and are associated with distinct forms of *CRX* disease. We now have animal models which

accurately recapitulate many of these disease forms. We have used these models to understand their unique pathologies and identify underlying disease mechanisms including the unexpected finding of mutant allele-specific overexpression of frameshift mutations due to increased mRNA stability. These models demonstrate the importance of carefully and comprehensively designing and characterizing animal models to understand human disease. Our work will make it possible for the accurate testing of potential therapeutic strategies with the hope that these approaches could eventually by translated to human patients.

Chapter VI

References

1. Sohocki, M. M. *et al.* A range of clinical phenotypes associated with mutations in CRX, a photoreceptor transcription-factor gene. *Am J Hum Genet* **63,** 1307–1315 (1998).

2. Jacobson, S. G. *et al.* Retinal degenerations with truncation mutations in the cone-rod homeobox (CRX) gene. *Invest Ophthalmol Vis Sci* **39,** 2417–2426 (1998).

3. Hanein, S. *et al.* Leber congenital amaurosis: comprehensive survey of the genetic heterogeneity, refinement of the clinical definition, and genotype-phenotype correlations as a strategy for molecular diagnosis. *Hum. Mutat.* **23,** 306–17 (2004).

4. Dharmaraj, S. R. *et al.* Mutational analysis and clinical correlation in Leber congenital amaurosis. *Ophthalmic Genet.* **21,** 135–50 (2000).

5. Galvin, J. a, Fishman, G. a, Stone, E. M. & Koenekoop, R. K. Evaluation of genotype-phenotype associations in leber congenital amaurosis. *Retina* **25,** 919–29

6. Nakamura, M., Ito, S. & Miyake, Y. Gene in a Japanese Patient With. **24,** 465–467 (1998).

7. Zhang, Q. *et al.* Screening for CRX gene mutations in Chinese patients with Leber congenital amaurosis and mutational phenotype. *Ophthalmic Genet.* **22,** 89–96 (2001).

8. Lotery, a J. *et al.* Mutation analysis of 3 genes in patients with Leber congenital amaurosis. *Arch. Ophthalmol.* **118,** 538–43 (2000).

9. Wang, P., Guo, X. & Zhang, Q. Further evidence of autosomal-dominant Leber congenital amaurosis caused by heterozygous CRX mutation. *Graefes Arch. Clin. Exp. Ophthalmol.* **245,** 1401–2 (2007).

10. Huang, L. *et al.* CRX variants in cone-rod dystrophy and mutation overview. *Biochem. Biophys. Res. Commun.* **426,** 498–503 (2012).

11. Mitton, K. P. *et al.* The leucine zipper of NRL interacts with the CRX homeodomain. A possible mechanism of transcriptional synergy in rhodopsin regulation. *J. Biol. Chem.* **275,** 29794–9 (2000).

12. Swaroop, A. *et al.* Leber congenital amaurosis caused by a homozygous mutation (R90W) in the homeodomain of the retinal transcription factor CRX: direct evidence for the involvement of CRX in the development of photoreceptor function. *Hum Mol Genet* **8,** 299–305 (1999).

13. Chen, S. *et al.* Functional analysis of cone-rod homeobox (CRX) mutations associated with retinal dystrophy. *Hum Mol Genet* **11,** 873–884 (2002).

14. Terrell, D. *et al.* OTX2 and CRX rescue overlapping and photoreceptor-specific functions in the Drosophila eye. *Dev. Dyn.* **241,** 215–28 (2012).

15. Tani, H. *et al.* Genome-wide determination of RNA stability reveals hundreds of short-lived noncoding transcripts in mammals. *Genome Res.* **22,** 947–56 (2012).

16. Chen, C.-Y. a, Ezzeddine, N. & Shyu, A.-B. *Messenger RNA half-life measurements in mammalian cells. Methods Enzymol.* **448,** 335–57 (Elsevier Inc., 2008).

17. Watanabe, S. *et al.* Tropisms of AAV for subretinal delivery to the neonatal mouse retina and its application for in vivo rescue of developmental photoreceptor disorders. *PLoS One* **8,** e54146 (2013).

18. Lamba, D. a, Gust, J. & Reh, T. a. Transplantation of human embryonic stem cell-derived photoreceptors restores some visual function in Crx-deficient mice. *Cell Stem Cell* **4,** 73–9 (2009).

Appendix A - Materials and Methods

Ethics statement

All procedures involving mice were approved by the Animal Studies Committee of Washington University in St. Louis, and performed under Protocols # 20090359 and 20120246 (to SC). Experiments were carried out in strict accordance with recommendations in the Guide for the Care and Use of Laboratory Animals of the National Institutes of Health (Bethesda, MD), the Washington University Policy on the Use of Animals in Research; and the Guidelines for the Use of Animals in Visual Research of the Association for Research in Ophthalmology and Visual Science (http://www.arvo.org/animals/). Every effort was made to minimize the animals' suffering, anxiety, and discomfort.

Mice

Mice were housed in a barrier facility operated and maintained by the Division of Comparative Medicine of Washington University School of Medicine. All mice used for experiments were backcrossed to *C57BL6/J* mice obtained from Jackson Laboratories (Bar Harbor, ME, Stock number 000664) for at least 5 generations. *Knock-IN* of *E168d2neo* and *R90Wneo* were generated by the Mouse Genetics Core, Department of Ophthalmology and Visual Sciences, Washington University (Saint Louis, MO). *E168d2neo* and *R90Wneo* constructs were transfected into *129Sv/J* SCC#10 (ATCC SCRC-1020) embryonic stem cells and Knock-IN was achieved by homologous recombination into the endogenous *mCrx* locus and selected by *neomycin*. The targeted ES cells were injected into *C57BL6/J* blastocysts to form chimeric *Knock-IN E168d2neo* and *R90Wneo* mice. Germline transmission of *E168d2neo* and *R90Wneo* was identified by PCR genotyping and Sanger sequencing of genomic DNA from

F1 mice (Fig 2.1, *Tran NM et al. PLOS Genetics 2013*, Fig S1; Table 2.1). *Crx*$^{-/-}$ mice were provided by Dr. Constance Cepko, Harvard University (Boston, MA).

PCR Genotyping

Genomic DNA was prepared from mouse tail tissue using the Gentra Puregene Tissue Kit (Qiagen). PCR amplification was performed using Jumpstart RedTaq (Sigma-Aldrich). Primer sets (Table 2.1) are as follows: For all mice: *neo* (Neo-F/R) and Crx (Total Crx-F/R); for *E168d2* colony: *WT Crx* allele (E168d2 WT-F, E168d2-R), *E168d2* allele (E168d2 Mut-F, E168d2-R); for *R90W* colony: *WT Crx* allele (R90W WT-R, R90W-R), *R90W* allele (R90W Mut-F, R90W-R).

Sanger sequencing of genomic DNA

Genomic DNA was prepared from mouse tail tissue using the Gentra Puregene Tissue Kit (Qiagen). *mCrx* DNA was amplified by PCR using the Genomic *mCrx* Int/Ex4-F/R primer pair (Table 2.1). Sanger sequencing was performed by the Protein and Nucleic Acid Chemistry Laboratory (Washington University, Saint Louis, MO) using the Sequencing primers *E168* and *R90W* (Table 2.1) and Big Dye V3.1 (Advanced Biotechnologies).

Electroretinogram

At least 5 mice of each genotype were tested for ERG at 1mo, 3mo, or 6mo of age. Bilateral flash ERG measurements were performed using a UTAS-E3000 Visual Electrodiagnostic System running EM for Windows (LKC Technologies, Inc., Gaithersburg, MD) and recordings from the higher amplitude eye were used for analysis. Mice were dark-adapted overnight, then anesthetized with 80 mg/kg ketamine and 15 mg/kg xylazine under dim red illumination for electrode placement and testing. Body temperature was maintained at 37± 0.5^{o}C with a heating pad controlled by a rectal temperature probe (FHC Inc., Bowdoin, ME).

Appendix A - Materials and Methods

The mouse's head was positioned just inside the opening of the Ganzfeld dome and pupils were dilated with 1.0% atropine sulfate (Bausch & Lomb, Tampa, FL). The recording electrode was a platinum loop 2.0 mm in diameter, positioned in a drop of 1.25% hydroxypropyl methylcellulose (GONAK; Akorn Inc., Buffalo Grove, IL) on the corneal surface of each eye. The reference needle electrode was inserted under the skin at the vertex of the skull. The ground electrode was inserted under the skin of the mouse's back or tail. The stimulus (trial) consisted of a brief, full-field flash (10 μs) either in darkness, or in the presence of dim (29.2 cd/mm) background illumination after 10 minutes adaptation time to the background light. The initiation of the flash was taken as time zero. The response was recorded over 250 ms plus 25 ms of pre-trial baseline. Responses from several trials were averaged. For complete test parameters see Table S7 (*Tran NM et al. PLOS Genetics 2013*). The log light intensity (log [$^{cd*s}/_{m}{}^{2}$]) was calculated based on the manufacturer's calibrations. The mean amplitudes (in microvolts) of the averaged dark-adapted A and B-waves and light-adapted B-waves were measured and quantified for comparison. The between-group differences in peak amplitude were determined by testing genotype*flash intensity interactions ($p<0.05$, $n\geq5$) at each age were compared using two-way ANOVA for repeated measurement data to account for potential correlations among readings from the same mice. If the overall genotype*flash intensity interaction was significant, post-hoc multiple comparisons for differences between each genotype and the control group at each light intensity level were performed. All the tests were two-tailed, significance: $p<0.05$. The statistical analysis was performed using SAS 9.3 (SAS Institutes, Cary, NC). p-values were adjusted for multiple comparisons by a permutation test using the default parameters provided in the LSMestimate statement in Proc Mixed. Average percent reductions for each wave form were calculated by normalizing the peak amplitude of the mutant to *WT* and results were averaged for the flashes listed in Table 1; ±STDEV.

Appendix A - Materials and Methods

Immunohistochemistry and microscopy

For retinal sections: eyes were enucleated by removing the cornea and lens and fixed in 4% paraformaldehyde for 24hrs at 4˚C. A small corneal tag on the superior portion of the eye was used for orientation. Eyes were embedded in paraffin and 5μM sagittal retinal sections were cut using a Leica RM 2255 microtome as previously described[49]. Hemotoxylin and eosin immunohistochemistry was performed on sections for histology. Fluorescent antibody immunostaining was performed using as previously described using 1% BSA/0.1% Triton X in 1X PBS for blocking and antigen retrieval for all samples[3,49].

For whole flat-mounted retinas: eyes were enucleated by removing the cornea and lens and fixed in 4% paraformaldehyde for 1hr at 4˚C. Retinas were then dissected from the eye cup and 4 evenly spaced relief lines were cut (Fig 2.6A). A scleral tag was left on the superior retina for orientation. Retinas were mounted on poly-D lysine coated slides (Thermo Scientific), blocked with 1% BSA/0.1% Triton X in 1X PBS and immunostained as previous.

Primary antibodies and dilutions used as follows: Mouse monoclonal anti-CRX M02 (1:200, Abova), rabbit anti-CRX 261 (1:200), rabbit anti-cone arrestin (CARR) (1:1000, Millipore), Rabbit anti-Opsin Red/Green (MOP) (1:1000, Millipore), Goat anti-OPN1SW (N-20) (SOP) (1:500, Santa Cruz), Mouse anti-Rhodopsin RET-P1 (RHO)(1:400, Chemicon), Peanut Agglutanin conjugated to Rhodamine (PNA)(1:500, Vector Labs). Secondary Antibodies (1:400): Goat anti-rabbit or mouse IgG antibodies coupled to Alexa Fluor A488, Rhodamine 568 or Cy2 647 (Molecular Probes) and Chicken anti-goat IgG (Molecular Probes). All slides were counterstained with hard set DAPI (Vectashield), except when using Cy2 secondary, which were counterstained with Slow Fade Gold DAPI (Invitrogen). All brightfield and fluorescent imaging was performed using an Olympus BX51 microscope and Spot RT3 Cooled Color Digital camera (Diagnostic instruments inc.).

TUNEL analysis was performed using the Apoptag Fluorescein in situ Apoptosis Detection Kit (Millipore) per kit instructions. TUNEL+ cells were counted in retinal sagittal

sections of P21 and P35 mice. Significant differences from *WT* control ($p<0.05$) were determined by the Kruskal-Wallis rank order test, which was used to protect against departures from the normal distribution assumption.

Morphometric ONL and Cone Analyses

For ONL morphometry, 20x retinal composites of hematoxylin and eosin (H&E) stained sagittal sections were analyzed using Image J software (http://rsb.info.nih.gov/ij/). The distance from the Optic Nerve (ON) was determined by drawing a curved line along the outer limiting membrane. The ONL thickness was measured at 100μM, 500μM, 1000μM, and 1500μM from the ON and 200μM from the peripheral edge on both the superior and inferior retina. Results are presented by 'spider graph'. The between-group differences in ONL thickness were determined by testing overall genotype*distance interactions ($p<0.05$, $n\geq3$) at each age were tested using two-way ANOVA for repeated measurement data, followed by a post-hoc test to adjust p-value for multiple comparisons between each genotype and the *WT* control group at each distance using SAS 9.3 (SAS Institutes, Cary, NC), as above.

Cone nuclear localization was determined by immunostaining retinal sections with CARR. The ONL was divided into 3 equally sized zones (OONL, MONL, IONL; Fig 5A) on 20x retinal composite images using Image J software (http://rsb.info.nih.gov/ij/) and the cone nuclei within in each zone from three sections for each mouse were counted. Significant differences from *WT* for each zone were determined by Kruskal-Wallis rank order test ($p<0.05$, $n\geq3$)

For cone density and opsin expression assessment, 10 images at 40x magnification of whole flat-mounted retinas were taken in the zones specified in Fig 2.6A. All peripheral images were taken ~400μM from the edge of the retina and the central image was taken ~250μM from the ON along the lateral axis. Cones were counted within a 200x200μM square grid for each image using Image J software and the density of cones/(mm^2*1000) was calculated. The between-group differences in cone density were determined by testing overall genotype*retinal

region interactions ($p<0.05$, $n\geq3$) at each age were tested using two-way ANOVA for repeated measurement data, followed by a post-hoc test to adjust p-value for multiple comparisons between each genotype and the *WT* control group in each retinal region using SAS 9.3 (SAS Institutes, Cary, NC), as above. For regional cone opsin expression analysis (Fig 2.8E-P), differences in the fraction of cones expressing SOP, MOP, SOP/MOP or no opsin was tested in each region using a Kruskal-Wallis rank order test ($p<0.05$).

Transmission Electron Microscopy (TEM)

For TEM studies, eyes were enucleated by removing the cornea and lens and fixed in 2% paraformaldehyde/3% gluteraldehyde in 0.1 M phosphate buffer (pH 7.35) for 24 hrs, post-fixed in 1% osmium tetroxide for 1 hr and stained *en bloc* with 1% uranyl acetate in 0.1 M acetate buffer for 1 hr. Blocks were then dehydrated in a graded series of acetones and embedded in Araldite 6005/EMbed 812 resin (Electron Microscopy Sciences). Semi-thin sections (0.5-1μm) were cut through the entire retina at the level of the optic nerve and stained with toluidine blue, post-stained with uranyl acetate and lead citrate, viewed on a Hitachi H7500 electron microscope and documented in digital images. Three retinas for each genotype were sampled at P21 at 800-1200μM from the optic nerve. ≥10 images of four key features were collected by random sampling: OS-RPE (10000x), OS-IS (12000x), ONL (5000x), OPL (10000x). Images were analyzed in a blinded manner using Image J software.

The nuclear percent area of heterochromatin was measured using Image J software in a randomized blinded analysis. For each genotype, 10 5000x images of the ONL were taken for three mouse retinas. For each image, 10 rod nuclei were randomly selected for analysis. The rod nucleus was outlined using the segmented polygon tool, electron dense regions of the nuclei associated with heterochromatin were thresholded and the percentage of the area above the threshold was measured. Thresholding was variably adjusted to accommodate for differences in brightness and contrast. The between-group differences were compared using

one-way ANOVA for repeated measurement data, to account for potential correlations among photos from the same mouse. All the tests were two-tailed, significance: $p<0.05$ (n=3). The statistical analysis was performed using SAS 9.3 (SAS Institutes, Cary, NC). The overall test for genotype difference was statistically significant (p=0.02), therefore *E168d2*/+ and *E168d2neo*/+ were compared to *WT* Fig 2.6).

Transient transfection assays

HEK293 cells (ATCC© CRL-11268) were cultured on 60mm plates in Dulbucco's minimum essential media (DMEM) with 10% fetal bovine serum and Penicillin/Streptomycin. Cells in 60% confluence were transfected with *pCAGIG-NRL* and *pCAGIG-hCRX WT*, *E168d2* and *R90W* either alone or in combination using CaCl (0.25M) and Boric Acid Buffered Saline (1x) pH 6.75 as previously described[3]. Cells were harvested 48 hours post transfection for either RNA (PerfectPure RNA tissue kit, 5Prime), protein (NePER nuclear and cytoplasmic extractions reagents, Thermo Scientific), or Dual-luciferase assays. Dual-luciferase assays were performed as previously described[3]. Significant differences from pcDNA3.1hisc control were determined by Kruskall-Wallis rank order test ($p<0.05$; n=3). Post-hoc comparisons (Fig 2.10 D&E; indicated by brackets) were tested using a less conservative FDR p-value method for multiple comparisons using PROC Multtest of SAS (V9.3). FDR $p<0.09$ was considered marginally significant.

Western Blot assays

Whole retina protein lysates were prepared by homogenization of four genotype-matched isolated whole retinas from P10 mice and lysis in 1x RIPA buffer (Sigma) for 10min with protease inhibitors (Aprotinin, Leupeptin, peptistatin, 0.1mM Phenylmethaneslfonyl fluoride). Nuclear lysates were prepared using NE-PER Nuclear and Cytoplasmic Extraction Reagants (Thermo Scientific) with protease inhibitors. Either 30µg of whole protein lysate or

5µg of nuclear protein lysate was boiled for 10min. Samples were run on a 4-11% SDS-PAGE gel and transferred onto Transblot Turbo nitrocellulose membranes (Bio-Rad) using the Transblot Turbo system (Bio-Rad). Membranes were probed with Rabbit anti-CRX 119b1 (1:750) and Mouse anti-β-Actin (Sigma)(1:1000). Goat anti-Mouse IRDye 680LT and Goat anti-Rabbit IRDye 800CW (LI-COR) were used as secondary antibodies. Signal was detected and quantified using the Odyssey Infrared Imager (LI-COR) and associated manufactory software. Kruskal-Wallis rank order test (Proc Npar1way of SAS, V9.3) was used to test for an overall difference among genotypes ($p=0.0002$), then each genotype was compared to *WT* control ($p<0.05$). Post-hoc analyses were performed using FDR p methods for multiple comparisons using PROC Multtest of SAS (V9.3) (FDR $p<0.09$) ($n\geq3$).

qRT-PCR

RNA was extracted from whole retinas of one male and one female mouse at either P10 or P21 for each biological replicate using the PerfectPure RNA tissue kit (5Prime). RNA was quantified using a NanoDrop ND-1000 spectrophotometer (NanoDrop Technologies, Wilmington, DE). cDNA was synthesized from 1µg of RNA using the Transcriptor First Strand cDNA Synthesis kit (Roche Applied Science). A 10µl QRT-PCR reaction mixture containing 1x EvaGreen with Low Rox reaction mix (BioRad), 1µM primer mix, and diluted cDNA was prepared and run on a two-step 40 cycle amplification protocol with melt curve determination on a BioRad CFX thermocycler in triplicate. The Cq's of technical replicates were averaged and the results were analyzed using the Delta Cq method in QBase software (Biogazelle). Primer sets (*Tran NM et al. PLOS Genetics 2013*, Table S1) were designed using MacVector software and synthesized by IDT DNA technologies. For *mCrx* allele specific amplification the following primers were used: for *E168d2* and *E168d2neo* mice: WT allele specific- Crx E168d2 WT RTF/R, total- Crx R90W WT-RTF/R; for *R90W* and *R90Wneo* mice: WT allele specific- Crx R90W WT-RTF/R, total Crx E168d2 WT RTF/R (Fig 2.2J), Relative gene expression was

normalized to *Ubb* and *Tuba1b*. Kruskal-Wallis rank order test (Proc Npar1way of SAS, V9.3) was used to test for an overall difference among genotypes ($p<0.05$; $n\geq3$). Post hoc analyses were adjusted for multiple comparisons using FDR p methods, as above (FDR $p\leq0.09$).

Electrophoretic mobility shift assays (EMSA)

BAT-1 and *BAT-1* mutated *AB* probes 5' end-labeled with 700 IRDye were synthesized by Integrated DNA Technologies (IDT). Nuclear protein extracts from HEK293 cells (~$1x10^8$ cells) transfected with *pCAGIG-hCRX*, *pCAGIG-hCRX E168d2*, or *pCAGIG-hCRX R90W* were prepared following NE-PER kit instructions (Thermo Scientific). Nuclear extracts were tested for CRX expression by running on a Western Blot as above (Fig 2.8B). CRX levels were quantified by normalizing to β-Actin (Sigma) and a 2-fold dilution series of equivalent amounts of CRX WT, $CRX^{[E168d2]}$ and $CRX^{[R90W]}$ protein were used for binding reactions. Binding reactions were performed using the Odyssey Infrared EMSA kit (LI-COR), per kit instructions using 1µg of nuclear protein extract and 50nM IRDye labeled oligo. Samples were run on a native 5% polyacrylamide; 0.5x Tris/Borate/Ethylenediaminetetraacetic acid (EDTA) buffered gel and imaged on the Odyssey Infrared Imager (LI-COR).

Chromatin immunoprecipitation (ChIP) assays

ChIP was performed as previously described[3,5,50]. Basically, 6 retinas per sample were dissected and chromatin was cross-linked with 1% formaldehyde in PBS for one minute at room temperature. After cell lysis and chromatin fragmentation by sonication, chromatin fragments were immunoprecipitated with the CRX 119b-1 antibody[5] or normal rabbit IgG (Santa Cruz) bound to Protein A beads (GE Healthcare Life Sciences, Piscataway, NJ). After extensive washing, the immunoprecipitated chromatin was eluted with 50mM $NaHCO_3$ 1% SDS, heated to 67°C to reverse the cross-links, the DNA purified by ethanol precipitation and analyzed by PCR

with gene-specific primers (Table 2.1) (n≥3). Fold enrichment was determined by quantitative ChIP PCR. Critical threshold (Ct) values for CRX and IgG immunoprecipitation (IP) were normalized to input and mock subtracted. The fold enrichment of CRX:IgG was calculated based on the formula shown below. Significant enrichment was determined by testing overall promoter*genotype interactions by two-way ANOVA for repeated measures using SAS 9.3 (SAS Institutes, Cary, NC) ($p<0.05$, $n=3$), as above.

ΔCt= (Ct[CRX or IgG]-Ct[Input])

$\Delta\Delta Ct$= ΔCt[CRX or IgG]- ΔCt[mock]

Fold enrichment= $((2^{-\Delta\Delta Ct\ CRX})/(2^{-\Delta\Delta Ct\ IgG})$

Microarray

Triplicate RNA samples were prepared from 4 pooled retinas from 1 male and 1 female mouse at P10 for *WT* and homozygous *E168d2neo, R90Wneo* and -/- mice using the PerfectPure RNA Tissue Kit (5 Prime). The RNA was fluorescent labeled and hybridized to MouseWG-6 v2.0 Expression Beadchips (Illumina) by Washington University Genome Technology Access Center (GTAC). The raw microarray datasets are available at the NCBI GRO website (http://www.ncbi.nlm.nih.gov/gds, access number: GSE51184). Microarray data were analyzed using significance analysis of microarrays (SAM) following background subtraction and quantile normalization in Illumina Genome Studio platform. Control probes and probes with detection p-value <0.05 across all samples were removed prior to any analysis. Candidate probes with 2.0-fold disregulation at false discovery rate ≤0.05 from each comparison were chosen for further analysis. Cellular processes associated with differentially expressed genes were assigned based on gene ontology provided by Mouse Genome Informatics (http://www.informatics.jax.org/).

Appendix A - Materials and Methods

Next-generation RNA-Seq

Triplicate RNA samples were prepared from 4 pooled retinas from 1 male and 1 female mouse at P10 for *WT*, *E168d2/d2, R90W/W, E168d2/+, E168d2neo/+, R90W/+* and P21 *WT, E168d2/+, E168d2neo/+* and *R90W/+* mice using the PerfectPure RNA Tissue Kit (5 Prime). Total RNA was processed by GTAC using standard protocol and sequenced on the Illumina HiSeq. 1x42bp reads were aligned to the mouse genome (version mm9) with the sequence aligner TopHat. The HTSeq package was used to assign aligned reads to the gene annotation reference track (UCSC Genes). This generated a raw read count per gene which was used in EdgeR(v3.2.4) for detecting differentially expressed genes. For each of the genotype comparisons, genes that did not pass the filter criteria of CPM (Counts Per Million) >=5 in all replicates of at least one comparison group were removed prior to the analysis. Filtered count data was normalized by the EdgeR default normalization method, TMM, and differential expression analysis for each of the comparison groups were performed by the exact test. P-values were subjected to Bonferroni and Hochberg multiple testing correction to include false discovery rate (FDR). Downstream analysis was performed using custom perl and R scripts. Heatmaps were generated using the heatmap.2 function of the gplots R package.

Actinomycin D treatment

in vitro: Crx WT and *E168d2* constructs tagged distinct barcodes (Table 4.1) were co-transfected in pairs into HEK 293 cells and cultured, as previously described. Constructs carrying common barcodes were not co-transfected. After 48hrs, transfected cells were treated with 10mg/ml Actinomycin D (Sigma-Aldrich) diluted in DMSO, which blocks mRNA transcription[8–11]. Cell were incubated and then harvested at 4hrs and 8hrs. mRNA was collected, as previously described, and the expression of *Crx* mRNA was determined by qRT-

PCR and normalized to *Ubb* and *Gapdh* expression, results shown are the fold-change relative to expression level at time 0hrs.

ex vivo: Retinas were dissected at the same time and incubated in 6-well cell culture plates for 12hrs in 2ml explant media: 1:1 DMEM (Gibco):Ham's F12 (Gibco), 10%FBS, 100U Penicillin, 100mg/ml Strepomycin, 2mM L-Glutamine and 5µg/ml Insulin. 10mg/ml of Actinomycin D (Sigma) diluted in DMSO was added to the 8hr samples. At 4hrs, 10mg/ml of Actinomycin D was added to the 4hr samples and 8hr retinas were moved to fresh wells containing actinomycin. At 8hrs, retinas were placed in 400µl RNAlater (Qiagen), then prepared and analyzed by qRT-PCR as previously described.

Light damage (LD) and 13-cis RA treatments

For light treatments, mice were dark adapted overnight. Eyes were dilated with 1% Cyclogyl and 2.5% Phenylphrine Hydrochloride and placed in darkness 30min before light damage. LD was performed in a temperature controlled rat cage with the top removed and lined with reflective material to give an even distribution of light treatment. Treatment was performed using white fluorescencent light and the intensity was measured using a photometer. Light intensity was 11-13.5KLUX for all experiments. Mice were placed into 6 separate cages containing moistened food pellets and each receiving light treatments of even intensity for 8hrs. Mouse pupils were re-dilated every 2 hours. For 13-cis RA treatments, 13-cis RA (Sigma-Aldrich) was reconstituted in DMSO to a concentration of 0.013mg/µl. 40mg/kg 13-cis RA was injected into the mouse's interperitoneal cavity 12hrs before LD and mice were dark-adapted overnight. Mice were redosed with 40mg/kg 13-cis RA 30min before LD. Following all LD experiments, mice were returned to a 12hr light-dark cycle under normal ambient light

conditions (~100LUX) for 7 days. After 7 days, retinal function was tested by ERG and eyes were collected for histology, as previously described.

rAAV-mediated gene therapy

3xFLAG-tagged human *CRX* or shRNA targeting mouse *Crx* were subcloned into viral vector plasmids with expression driven from the photoreceptor specific *Rhodopsin Kinase (GRK)*[30] or ubiquitous *CBA (U11)*[31] promoters. Viral vector plasmid constructs were packaged into *rAAV* serotypes *2, 5, 8, 8/9, 2 triple Y-F* and *2 quad Y-F,* which were shown to have different infection characteristics in photoreceptors[30–32]. All viral vectors were packaged, purified, and titered according to previously described methods[31,33,34]. A titer of 1e10[11-12] of virus was injected into the sub-retinal space of P0-P3 mouse eyes in a barrier facility using a 32-guage hamilton syringe. Mice were housed in a barrier-facility for 14days-1mo and then sacked. Eyes were collected, and the sclera was removed for imaging. Eyes were imaged for Gfp using a Leica Macrofluor macroscope and embedded in OCT (BD Sciences). 10μM retinal sagittal sections were cut using a Cryostat and mounted on polysine-coated slides (Fisher) and stained using previously described protocols. 3xFLAG-tagged human CRX expression was detected using a monoclonal FLAG antibody (Sigma-Aldrich).